Experimental Studies and Simulations of Shock-Compressed Silicon

Paul G. Stubley
Worcester College
University of Oxford

A thesis submitted for the degree of
Doctor of Philosophy

Trinity 2016

For my parents

Abstract

The response of silicon to shock-compression has been an area of active research for decades. However, despite considerable improvements in both experimental techniques and computer simulations, the behaviour has not been unanimously constrained. This work introduces a new Lagrangian Elastic code which aims to approach the modelling of solids from a different direction to traditional hydrodynamics codes. We present data from a white-light Laue diffraction experiment, which along with molecular dynamics simulations, suggest that a kinetically inhibited phase-change may be indirectly responsible for the previously reported anomalous elastic response of silicon. We also present data from a monochromatic x-ray diffraction experiment which show the first observed diffraction from a shock-induced high-pressure phase in silicon.

Acknowledgements

I would like to take this opportunity to express my thanks to some of the people who have made this work possible. First and foremost, to my supervisor, Justin Wark, for the crucial insight and advice he has afforded me over the last four years. To Andy Higginbotham, for a great many things, not least for introducing me to Cattlemens. To Matt Suggit, for always offering help with the little things, and for patiently training me on hands-on experiments.

To AWE, for providing the funding for me to carry out this research.

To the scientists and experimental staff of the facilities at which I have been fortunate enough to carry out experiments: The Orion Laser Facility, The Central Laser Facility and The Jupiter Laser Facility.

To Joe and Shαmim, we started together, and we finished...well, we started together. To all the other students and postdocs in the Simon Room, for the predominantly senseless conversations over uncountable cups of coffee. To my housemates and friends over the last four years, for frequent and much needed distraction.

To Sophia, for putting up with me for so long, and for putting up with the barrage of doctor puns that are about to befall her.

And finally, to my family. To Richard, John and Anna, for always setting the bar so high, and expecting nothing less than for it to be cleared with room to spare. And to my parents, for the unwavering love, support and guidance that they have given me throughout my life. I will be forever grateful for everything they do. My mother recently put their role into perspective when, after I exasperatedly explained how to use some unintuitive function of the TV remote, she reminded me:

> *Just remember...I taught you how to use a spoon.*

Contents

List of Figures

List of Symbols

$\mathbf{a}_{1,2,3}$	The three primitive lattice vectors
$a_{1,2,3}$	The magnitudes of the three primitive lattice vectors
α_{ij}	The angle between the i^{th} and j^{th} primitive lattice vectors
h, k, l	The three Miller indices
d_{hkl}	The lattice spacing between planes defined by h, k, l
P	The hydrostatic pressure
$\mathbf{G}_{hkl}$	The reciprocal lattice vector
$\bar{\sigma}, \sigma_{ij}$	The stress tensor
$\bar{\epsilon}, \epsilon_{ij}$	The true strain tensor
$\bar{s}, s_{ijkl}$	The elastic compliance tensor
$\bar{c}, c_{ijkl}$	The elastic stiffness tensor
θ_B	The Bragg angle, the total scattering angle is $2\theta_B$
ρ_0	The ambient density of a material
$\sigma_{n,t}$	The stress in the normal (shock) and transverse directions
$\epsilon_{n,t}$	The true strain in the normal (shock) and transverse directions
Δx	The spatial resolution of a simulation
Δt	The temporal resolution of a simulation
R	The ratio of temporal and spatial resolutions
Σ_σ	The stress integral

$\lambda_{n,t}$	The scaled length, the ratio of current and initial lengths, in the normal and transverse directions
f	The phase fraction, the fraction of β-Sn in a given cell
κ	The phase fraction growth rate coefficient
σ^*	The phase change stress
$\Lambda_{d,ij}$	The weighted sum of the elastic compliance coefficients, s_{ij}, in the d direction
$\chi(f)$	The boundary term for a phase fraction f
μ	The boundary term coefficient
τ_{delay}	The phase change delay time

Chapter 1

Introduction

> *Almost overnight, ordnance laboratories throughout the world were able to convert technology developed for weapons into technology for visionary studies of matter in a new regime. Swords forged for nuclear weapon development were beaten into high pressure science plowshares.*
>
> - R. A. Graham, from Solids Under High-Pressure Shock Compression

1.1 The study of solids by shock compression

Modern day research into shock-compressed solids arguably emerged from the race to create an atomic bomb during the Second World War [1, 2]. The theory and experimental techniques that form the foundation of current investigations have their origins deeply rooted in that endeavour [3]. However, from these sombre beginnings a new field of science emerged, with wide reaching applications. For example, a considerable effort is currently invested in inertial confinement fusion [4], or ICF, in which a spherical capsule filled with deuterium and tritium is compressed to extremely high pressure. This causes the mixture to undergo nuclear fusion, resulting in the release of energy. The aim is to produce more energy from the fusion reaction than it takes to compress the capsule, therefore creating a net energy gain. If achieved, this could be a major source of clean energy for future generations, supplementing sustainable sources [5].

Another area of physics where these extreme pressures exist is in the interior of planets [6, 7, 8]. Understandably, it is very difficult to investigate the structure of planetary cores *in situ* [9, 10], and so high pressure laboratory experiments can provide invaluable insight. While shock compression experiments can complement static investigations of planetary interiors, they may also provide insight to shock processes on a celestial scale [11, 12]. The giant-impact hypothesis, which posits that the moon was formed as a result of a body the size of Mars colliding with Earth 4.5 billion years ago, highlights the possible magnitude of solid shock processes in the universe [13].

With the possible applications of shock compression of solid material being so diverse, there is active research into the underlying processes [14, 15, 16]. At its core, an understanding of the response of a crystal's structure to the passage of a high-pressure shock wave is key. Despite decades of research, and great improvements in both experimental and computational techniques, experiments based on this seemingly simple question continue to produce a wide variety of behaviour, showing that a simple and general response to shock compression is far from the case. As an example, a crystal may behave differently depending on the direction along which it is shocked (*e.g.* [17, 18]), resulting in different responses from that of the same material when hydrostatically compressed.

With the advent of time-resolved x-ray diffraction during the passage of a shock wave [19], and other short-timescale diagnostics, such as The Velocity Interferometer System for Any Reflector (VISAR) [20], knowledge of transient material behaviour is accessible, which adds yet more detail to the description. Elastic precursor decay [21] and kinetically inhibited phase changes [22, 23] are just two examples of time-dependent material responses.

Among these investigations, silicon is a popular test material, due to its ability to be produced in near-perfect, single crystal samples [24]. The appeal of these near-perfect crystals is to study the fundamental behaviour of a material, without the added complications of pre-existing crystallographic defects. Despite the faultless nature of the initial crystal structure, decades of research have not unanimously constrained the behaviour of silicon under uniaxial compression [25, 26]. Whether or not we know yet the full extent of the jigsaw that is silicon's material response, this thesis aims to set firmly, in the correct place, one more piece of the puzzle.

1.2 Accessing high-pressure states

The desire to access high-pressure states of matter has driven the development of numerous experimental techniques. The book by Asay and Shahinpoor [27] provides a good introduction to these, which we will follow here. Introductory references to each technique can be found therein.

One of the original methods was to create pressure waves by detonating high-explosives in direct contact with the sample material [28]. This method can create materials at pressures of several tens of GPa (1 GPa $\approx$ 10,000 atmospheres) [29]. By instead using the explosives to accelerate a flyer plate which in turn impacts the sample, pressures of hundreds of GPa can be reached [30, 31].

To alleviate the issues surrounding the use of explosives, particularly in university environments, and to provide more acute control over the conditions in the sample, gas-guns were developed [32]. Gas-guns use pressurised gas to propel a projectile into the target, creating a pressure wave of up to a few tens of GPa [33]. The development of two-stage gas guns [34] has increased the achievable pressures to several hundreds of GPa [35, 36].

One of the most widely used techniques in high-pressure studies is the diamond anvil cell [37]. A sample is placed between two diamonds, which are subsequently forced together, compressing the sample. A unique characteristic of this technique, compared with those above, is that it compresses materials statically, *i.e.* over indefinitely long timescales. This enables material structures to be investigated with great precision, for example by x-ray diffraction, without the transiency of dynamic compression methods. Traditional diamond anvil cells are limited by the strength of diamonds, and achieving pressures above $\sim 400\,\text{GPa}$ is extremely difficult [38]. Novel improvements to the method have increased this limit over 700 GPa [39, 40].

To access pressures above those achievable by diamond anvil cells, and to investigate time-dependent material responses, lasers can be used. When an intense laser is focussed on the sample, a process known as ablation occurs [41]. The electrons in the sample begin to oscillate in phase with the laser light, and resulting collisions transfer the laser energy to the ions in the crystal. If the laser is powerful enough, the transferred energy will result in the material becoming a plasma, and expanding away from the target. As the plasma travels away from the solid target in one direction, conservation of momentum requires that there is a transfer of momentum in the opposite direction, that is into the sample, resulting in a pressure wave being launched into the target. By tailoring the laser pulse, attributes of the pressure wave, such as amplitude, duration and temporal shape, can be adjusted. This technique has the ability to considerably increase the pressures available to experiments, whilst keeping the sample solid. As an example, in 2015, solid diffraction was observed from tin that had been laser compressed to 1.2 TPa [42]. If keeping the sample solid is not a requirement, laser shock-compression can create pressures at least up to 100 TPa [43].

For the work in this thesis, the desired pressures are accessible by several methods, and it is principally the time-dependence of the material response which is of interest. Specifically, the short timescales of the kinematic behaviour that forms one of the major focusses of this work makes it particularly suited to investigation by laser compression. Although we use laser compression for all data presented here, comparisons with gas-gun and diamond anvil cell work are made. At each stage, we must take into account the inherent differences in these methods, so that we are able to separate properties of the sample from features of the experimental method.

1.3 Thesis layout and role of the author

Chapter 2 gives a brief introduction to some of the underlying theory used in this thesis. The concepts and derivations are taken from a variety of sources, and more detailed discussions of any of the areas can be found in the given references.

Chapter 3 gives details of the Lagrangian elastic code which forms one of the two main simulation tools for the remainder of this thesis. The code was originally written to simulate plastic yielding by J. S. Wark and A. Higginbotham [44], but has been significantly developed by the author. The inclusion of the phase change model was the work of the author, with detailed guidance from A. Higginbotham. The molecular dynamics simulations, with which the Lagrangian elastic code is compared, were carried out by the author, using the LAMMPS code detailed in subsequent chapters. During the analysis of the molecular dynamics, the author used some tools written by other members of the Wark group, notably the Son-of-Howard code and the Per-atom-deformation-gradient code, which were both either written or collated by A. Higginbotham. A paper covering the work detailed in this chapter, written by the author, has been submitted to Computational Material Science.

Chapter 4 describes an experiment performed on the Orion laser at AWE, Aldermaston. Its success was the result of a large collaboration between members of the group here in Oxford, and researchers and experimental scientists from AWE. The principal results from this experiment have been published in Nature Scientific Reports [23], and details of the collaboration can be found in the author list of that paper. The author of this work was part of the experimental team, second author of the paper due to the significant contribution made to the work, and performed the analysis shown here. Initial fitting of the diffraction data was completed using the DIFFRACT code, written by A. Higginbotham, but subsequent analysis was carried out using codes written by the author, as detailed in the text. An understanding of the time-dependent behaviour of the phase-change described here came about through continued discussion with A. Higginbotham. The author is also grateful for the input of L. J. Peacock and J. M. Foster who provided information regarding the pressure-intensity scaling of the drive pulse, and who are acknowledged as their contributions are introduced.

Chapter 5 describes an experiment performed on the Linac Coherent Light Source in Stanford, CA. The author was not present on the experiment, becoming part of the collaboration after the experiment had been carried out. Details of the experimental team can be found in the author list of [45]. The analysis described here is the work of the author. Again the DIFFRACT code was used for initial fitting of the diffraction data, and all further analysis tools were written by the author. The author is grateful for the continued input of A. E. Gleason, of the original experimental team. A manuscript covering the work detailed in this chapter is being prepared for submission.

Chapter 6 summarises the work presented in this thesis, and discusses possibilities for future work.

1.4 List of publications

S. Patel *et al.* - Single Hit Energy-resolved Laue Diffraction. Rev. Sci. Instrum. 86, 053908 (2015).

A. Higginbotham *et al.* - Inelastic response of silicon to shock compression. Sci. Rep. 6, 24211 (2016).

P. G. Stubley *et al.* - Simulations of the Inelastic Response of Silicon to Shock Compression. Submitted to Computational Material Science (June 2016).

Chapter 2

Theoretical Background

This chapter outlines the theoretical background that forms the foundation for much of the work in this thesis. The chapter is divided into four main sections: crystal structure, x-ray diffraction, shock waves, and simulating solids with computational codes. Much of this chapter follows closely the derivations set out in the textbooks by Warren [46], Nye [47], Simon [48], and Meyers [49], and a fuller description of the concepts introduced here can by found by referring to the relevant textbook.

2.1 Crystal Structure

2.1.1 Lattices

A crystal is a three-dimensional repetition of a unit of atoms or molecules, which builds up a periodic structure. In three dimensions, a *lattice* is made up of points defined by the vectors

$$\mathbf{R} = m_1\mathbf{a}_1 + m_2\mathbf{a}_2 + m_3\mathbf{a}_3, \tag{2.1}$$

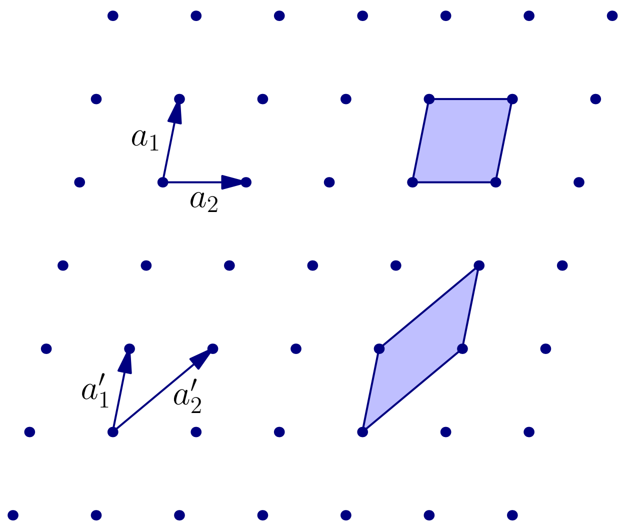

Figure 2.1: A two-dimensional lattice showing two choices of primitive lattice vectors, and two choices of primitive unit cell.

where m_1, m_2, m_3 are integers and $\mathbf{a}_1, \mathbf{a}_2, \mathbf{a}_3$ are non-coplanar vectors, known as the primitive lattice vectors. For a given lattice, the choice of primitive lattice vectors is not unique, as shown in figure 2.1. Each point in the lattice is equivalent, and the lattice appears the same irrespective of which lattice point is chosen as the origin. The three primitive vectors define the edges of a parallelepiped which, when repeated at each lattice point, fills the entire space without overlapping. This parallelepiped is known as a primitive unit cell, and is the smallest volume which, when repeated, will fill the space. Primitive unit cells contain exactly one lattice point. The volume of the primitive unit cell is given by $v = \mathbf{a}_1 \cdot \mathbf{a}_2 \times \mathbf{a}_3$. Although the primitive unit cell defined with its edges lying along the three primitive lattice vectors is perhaps the most obvious, there are many choices of primitive unit cells that fulfil the above criteria. To illustrate this concept, an alternative choice, for the two dimensional case, is shown in figure 2.1.

In general, the length and direction of the vectors $\mathbf{a}_1, \mathbf{a}_2, \mathbf{a}_3$, and therefore the positions of the points on the lattice, can be arbitrary. In three dimensions, there are seven distinct lattice systems, characterised by their inherent symmetries. As well as these, additional lattices can be formed by adding lattice points to the unit cell, either to some or all of the faces, or at the unit cell centre. There are six possible lattice centerings:

Simple / Primitive: lattice points on the corners of the unit cell only.

Body-centred: lattice points on the corners, and one additional point in the centre of the unit cell.

Face-centred: lattice points on the corners, and one additional point in the centre of each face of the unit cell.

Base-centred: lattice points on the corners, and one additional point in the centre of each face of one pair of parallel faces of the unit cell. There are three base-centred variants.

Combining each of these centerings with each of the lattice systems gives $7 \times 6 = 42$ lattices. As some of these lattices have identical symmetries, by careful choice of the primitive lattice vectors, the list can be reduced to 14 distinct lattices. These were identified by Auguste Bravais in 1850 [50], and are known as the Bravais lattices. Those whose lattice vectors are of unequal length ($a_1 \neq a_2 \neq a_3$) and are non-orthogonal ($\alpha_{12} \neq \alpha_{23} \neq \alpha_{31}$)[1] have the lowest symmetry and are known as triclinic. Those with $a_1 = a_2 = a_3$ and $\alpha_{12}, \alpha_{23}, \alpha_{31} = 90°$ have the highest symmetry and are known as cubic lattices. The three cubic Bravais lattices are primitive (or simple) cubic (sc), body-centered cubic (bcc), and face-centered cubic (fcc).[2] The primitive unit cell for simple cubic is shown in figure 2.2a.

While the primitive cell mentioned above is the smallest unit cell, and contains by construction only one lattice point, it is often more convenient to consider the *conventional* unit cell, which contains more than one lattice point. The conventional

---

[1] $|\mathbf{a}_i| = a_i$ and α_{ij} is the angle between lattice vectors $\mathbf{a}_i$ and $\mathbf{a}_j$.

[2] Strictly speaking, for symmetric primitive basis vectors, fcc has $a_1 = a_2 = a_3$ and $\alpha_{12}, \alpha_{23}, \alpha_{31} = 60°$, while bcc has $a_1 = a_2 = a_3$ and $\alpha_{12}, \alpha_{23}, \alpha_{31} = 109°28'$. The choice of conventional unit cells shown in figure 2.2 removes the need to think in terms of the non-orthogonal primitive lattice vectors, and instead uses orthogonal conventional lattice vectors that are given by the edges of the cubic cell.

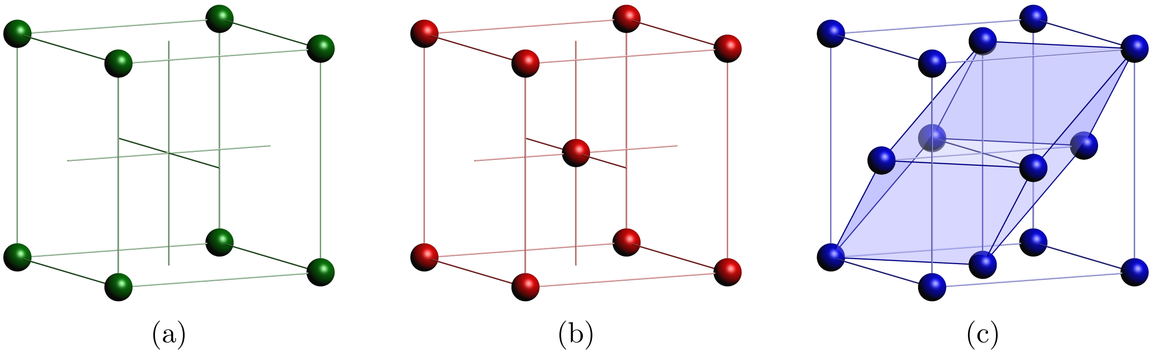
(a) (b) (c)

Figure 2.2: The three cubic Bravais lattices: (a) simple cubic, (b) body-centred cubic (bcc) and (c) face-centred cubic (fcc). We also illustrate the primitive unit cell for the fcc lattice.

unit cells for bcc and fcc are shown in figure 2.2b and 2.2c, and contain 2 and 4 lattice points respectively. Also shown is the primitive unit cell of fcc, for comparison.

2.1.2 Bases

For a given material, the positions of the atoms (or molecules) within the unit cell are given by the basis. If the atoms in the unit cell are labelled $1, 2, ..., n$, and have positions $\mathbf{r}_1, \mathbf{r}_2, ..., \mathbf{r}_n$ in the unit cell, then the position of every atom of type-n in the crystal is given by

$$\mathbf{R} = m_1\mathbf{a}_1 + m_2\mathbf{a}_2 + m_3\mathbf{a}_3 + \mathbf{r}_n. \tag{2.2}$$

Though they are lattices in their own right, the bcc and fcc lattices can be described as a simple cubic lattice with a basis, as shown below.

$$\text{bcc}: \qquad \mathbf{r}_1 = \mathbf{0}, \qquad \mathbf{r}_2 = \tfrac{1}{2}(\mathbf{a}_1 + \mathbf{a}_2 + \mathbf{a}_3), \tag{2.3}$$

$$\text{fcc}: \qquad \mathbf{r}_1 = \mathbf{0}, \qquad \mathbf{r}_2 = \tfrac{1}{2}(\mathbf{a}_1 + \mathbf{a}_2), \qquad \mathbf{r}_3 = \tfrac{1}{2}(\mathbf{a}_2 + \mathbf{a}_3), \qquad \mathbf{r}_4 = \tfrac{1}{2}(\mathbf{a}_1 + \mathbf{a}_3). \tag{2.4}$$

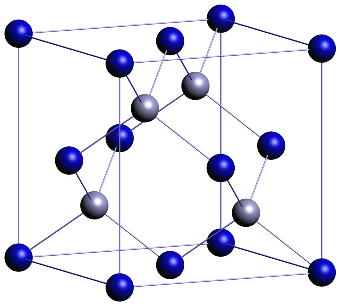

Figure 2.3: The conventional unit cell for cubic diamond, which contains four lattice points, and eight atoms. The $\mathbf{r}_1$ atoms are shown in dark blue, while the $\mathbf{r}_2$ atoms are shown in pale blue.

The majority of the work in this thesis will concentrate on silicon crystals, which, at ambient pressure, have a structure composed of an fcc lattice with a 2-atom basis, known as cubic diamond (cd). The basis is given by

$$\text{cd}: \qquad \mathbf{r}_1 = \mathbf{0}, \qquad \mathbf{r}_2 = \tfrac{1}{4}(\mathbf{A}_1 + \mathbf{A}_2 + \mathbf{A}_3), \tag{2.5}$$

where we have here made explicit that the basis positions are being measured relative to the *conventional* fcc unit cell by using $\mathbf{A}_{1,2,3}$, the conventional lattice vectors. The cubic diamond structure is shown in figure 2.3, where for clarity the type-2 atoms are shown in pale blue. Like the fcc lattice, the cubic diamond lattice has four lattice points per conventional unit cell, however, due to its basis, each conventional unit cell contains eight atoms.

For crystals with a one-atom basis, *i.e.* a single atom on every lattice point, it is usually sufficient to state the lattice type without the basis.

2.1.3 Lattice planes

Now that we have an understanding of lattices, it will be necessary in much of what follows to refer to planes of atoms within the structure. In order to do this, the usual convention is to label the planes by three integers, h, k and l, known as Miller indices. A given choice of three Miller indices describes a set of parallel, infinite and equally spaced planes, the first of which passes through the origin, and the next closest of which intersects the three lattice vectors at $\mathbf{a}_1/h$, $\mathbf{a}_2/k$ and $\mathbf{a}_3/l$ respectively, as shown in figure 2.4. For a given set of planes in an orthorhombic lattice (one with $\alpha_{12}, \alpha_{23}, \alpha_{31} = 90°$), the perpendicular distance between neighbouring planes, d_{hkl}, is given by

$$\frac{1}{d_{hkl}^2} = \frac{h^2}{a_1^2} + \frac{k^2}{a_2^2} + \frac{l^2}{a_3^2}. \tag{2.6}$$

Due to the symmetry of the lattice, there will be equivalent sets of planes, which can be grouped into families. For example, for a cubic lattice the planes defined by (100) are equivalent to the planes defined by (010), through simple rotation of the lattice. As such they can be considered collectively in the family $\{100\}$, where the curly brackets donate a family of planes. Also included in this family is any set of planes where one Miller index is 1 or -1, while the other two are zero.[3] For a given family, the number of distinct sets of planes is called the *multiplicity*, *e.g.* for the $\{100\}$ family of a cubic lattice, the multiplicity is 6.

Each set of planes is defined by two properties: their orientation and their interplanar distance. We can create a single vector, $\mathbf{G}_{hkl}$, whose direction is normal to the planes and whose magnitude is related to the interplanar distance, which would thus encompass both of these properties. In order to do this we first define a set of *reciprocal* lattice vectors, $\mathbf{b}_1, \mathbf{b}_2, \mathbf{b}_3$, and from these construct the vector $\mathbf{G}_{hkl}$. We will see that this reciprocal lattice is of great importance in the study of x-ray diffraction.

---

[3] A negative Miller index m is either written $-m$, or more frequently $\bar{m}$, for example $(1\bar{1}1)$ denotes h=1, k=-1 and l=1.

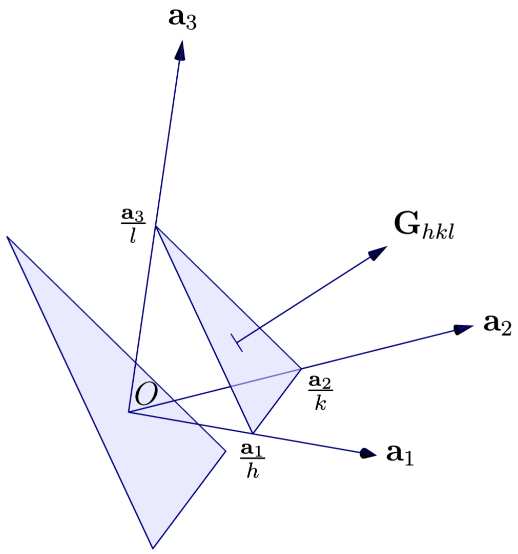

Figure 2.4: Illustrating how Miller indices (hkl) can be used to define a set of parallel planes of atoms.

2.1.4 The reciprocal lattice

We begin by defining the reciprocal lattice vectors and investigating their basic properties. We define the vectors as

$$\mathbf{b}_1 = 2\pi\frac{\mathbf{a}_2 \times \mathbf{a}_3}{\mathbf{a}_1 \cdot \mathbf{a}_2 \times \mathbf{a}_3}, \qquad \mathbf{b}_2 = 2\pi\frac{\mathbf{a}_3 \times \mathbf{a}_1}{\mathbf{a}_1 \cdot \mathbf{a}_2 \times \mathbf{a}_3}, \qquad \mathbf{b}_3 = 2\pi\frac{\mathbf{a}_1 \times \mathbf{a}_2}{\mathbf{a}_1 \cdot \mathbf{a}_2 \times \mathbf{a}_3}. \tag{2.7}$$

We can see that, by construction, the vectors have the following properties

$$\mathbf{a}_i \cdot \mathbf{b}_j = \begin{cases} 2\pi, & i = j, \\ 0, & i \neq j. \end{cases} \tag{2.8}$$

We will see that for a given set of planes (hkl), defined as above, the vector $\mathbf{G}_{hkl}$ defined by

$$\mathbf{G}_{hkl} = h\mathbf{b}_1 + k\mathbf{b}_2 + l\mathbf{b}_3, \tag{2.9}$$

is both orthogonal to the planes (hkl) and has a magnitude related to the interplanar distance, as desired. We first note that the two vectors $(\mathbf{a}_1/h$-$\mathbf{a}_2/k)$ and $(\mathbf{a}_2/k$-$\mathbf{a}_3/l)$ are both parallel to the (hkl) planes. We also see from equation 2.8 that

$$\begin{aligned}(\mathbf{a}_1/h - \mathbf{a}_2/k) \cdot \mathbf{G}_{hkl} &= (\mathbf{a}_1/h - \mathbf{a}_2/k) \cdot (h\mathbf{b}_1 + k\mathbf{b}_2 + l\mathbf{b}_3) \\ &= 2\pi - 2\pi = 0, \end{aligned} \tag{2.10}$$

and similarly for $(\mathbf{a}_2/k$-$\mathbf{a}_3/l)$. Therefore, $\mathbf{G}_{hkl}$ is perpendicular to two non-parallel vectors that lie in the plane (hkl), and so it is normal to the plane, as desired. The vector $\mathbf{G}_{hkl}$ is also shown in figure 2.4.

The perpendicular distance, d_{hkl}, between the plane that passes through the origin, and the next closest plane can be expressed as $(a_1/h)\cos\phi$, where ϕ is the angle between $\mathbf{a}_1$ and the unit normal to the plane, $\hat{\mathbf{n}}$. We can create a unit normal to the plane from $\mathbf{G}_{hkl}/|\mathbf{G}_{hkl}|$. This gives

$$\begin{aligned} d_{hkl} &= \frac{a_1}{h}\cos\phi = \frac{\mathbf{a}_1}{h} \cdot \hat{\mathbf{n}} = \frac{\mathbf{a}_1}{h} \cdot \frac{\mathbf{G}_{hkl}}{|\mathbf{G}_{hkl}|} \\ &= \frac{2\pi}{|\mathbf{G}_{hkl}|}. \end{aligned} \tag{2.11}$$

Therefore, the vector $\mathbf{G}_{hkl}$ has the two desired properties mentioned above. The interplanar spacing, d_{hkl}, is of critical importance in the theory of x-ray diffraction from crystals, as we will see later in the chapter.

2.1.5 Stress

Stress is defined as the force acting on a body, per unit area. For the simple case of a bar with cross-sectional area A, on which acts an axial force F, the axial stress is given by $\sigma = F/A$. In three dimensions, the stress depends on the direction of both the force and the area upon which it acts. The stress in three dimensions therefore

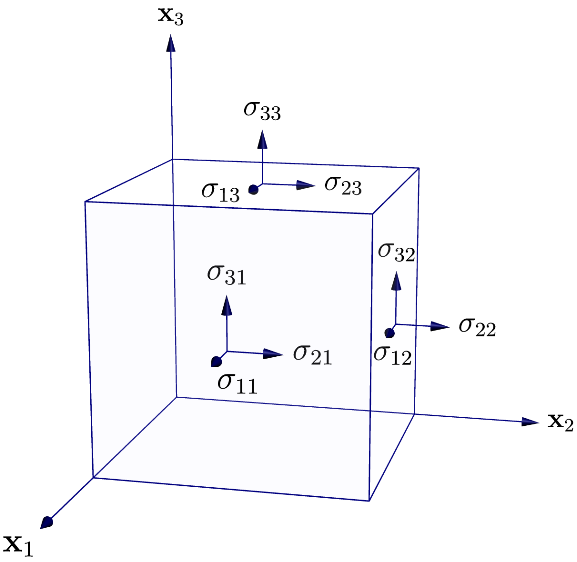

Figure 2.5: Illustrating the three dimensional stress tensor components.

has nine components and forms a second-rank tensor

$$\bar{\sigma} = \begin{pmatrix} \sigma_{11} & \sigma_{12} & \sigma_{13} \\ \sigma_{21} & \sigma_{22} & \sigma_{23} \\ \sigma_{31} & \sigma_{32} & \sigma_{33} \end{pmatrix}, \tag{2.12}$$

where σ_{ij} is the stress corresponding to a force acting along the $\mathbf{x}_i$ direction, on a surface which is normal to the $\mathbf{x}_j$ axis, as illustrated in figure 2.5.

In order that angular momentum is conserved in equilibrium, the stress tensor must be symmetric, $\sigma_{ij} = \sigma_{ji}$, leading to six independent stresses. Stresses for which $i = j$, the diagonal elements of the stress tensor, correspond to normal stresses, where the direction of the force is normal to the surface on which it acts. Stresses for which $i \neq j$, the off-diagonal elements, correspond to shear stresses, where the force acts along the surface.

This leaves us with a choice of sign convention, *i.e.* whether stresses should be measured positive in compression or tension. As the majority of this work will consider solids under compression we choose the (less popular) convention that positive stresses cause compression. The total pressure, P, is thus related to the positive trace of the stress tensor

$$P = \tfrac{1}{3}(\sigma_{11} + \sigma_{22} + \sigma_{33}). \tag{2.13}$$

2.1.6 Strain

Strain is a measure of the deformation a material exhibits when it is put under stress. As a one dimensional case, we consider an extendible fibre. If two points on the fibre, separated by a small distance l before a certain infinitesimal deformation, are separated by a distance $l + dl$ after that deformation, the change in strain is measured as[4]

$$\text{change in strain} = d\epsilon = -\frac{\text{change in length}}{\text{original length}} = -\frac{dl}{l}, \tag{2.14}$$

which we can integrate to give the *true* strain, ϵ,

$$\epsilon = -\ln\left(\frac{l}{l_0}\right), \tag{2.15}$$

where l_0 is the initial separation of the two points under no stress.

A common simplification is to use the *engineering* strain, e, which is just a ratio of the change in separation to the initial separation of the two points

$$e = -\frac{\Delta l}{l_0} = -\frac{l - l_0}{l_0} = 1 - \frac{l}{l_0} \qquad \Rightarrow \qquad l = l_0(1 - e). \tag{2.16}$$

We can show that for small enough strains, where $l - l_0 \ll l_0$, these two measures

---

[4] In a similar way to defining positive stresses causing compression, we here choose a convention to define positive strains in compression, as much of our work focusses on solids above normal density. A more frequently used definition would yield $\epsilon = \ln(l/l_0)$. This choice will result in some sign discrepancies between our derivations and the references from which they evolve.

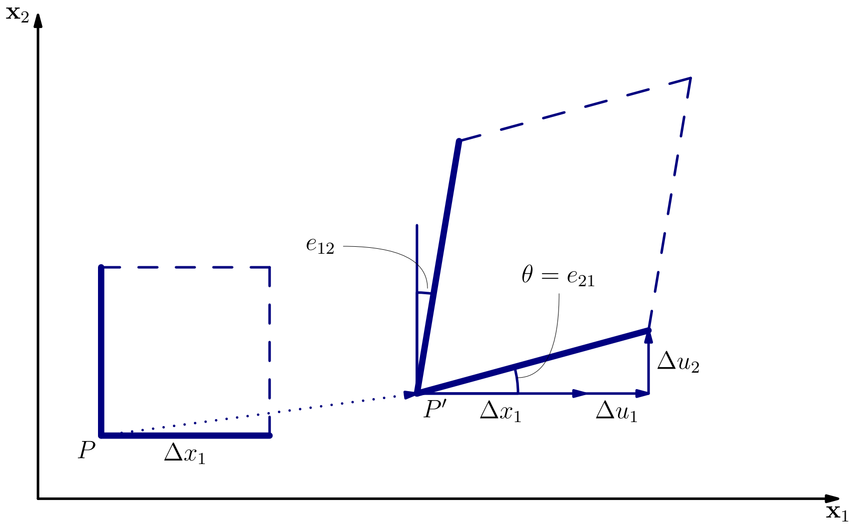

Figure 2.6: Illustration of two-dimensional strain. Line segments initially parallel to the $\mathbf{x}_1$ and $\mathbf{x}_2$ axes respectively are deformed in two dimensions.

of strain are equivalent. Taking the true strain and expanding the logarithm gives

$$\epsilon = -\ln\left(1+\frac{\Delta l}{l_0}\right) = -\left(\frac{\Delta l}{l_0} - \frac{1}{2}\left(\frac{\Delta l}{l_0}\right)^2 + ...\right) \simeq -\frac{\Delta l}{l_0} = e. \tag{2.17}$$

In two dimensions, for a given line segment on a plane, we must consider both deformations parallel to and perpendicular to the segment, as shown in figure 2.6. A point P in the unstrained material is moved to a point P' in the strained material. Small line segments extruding from P, parallel to the two axes, are strained under the deformation. For infinitesimal deformations, such that $\Delta u_{1,2} \ll \Delta x_{1,2}$, we define a second-rank *relative displacement* tensor with elements

$$e_{11} = -\frac{\Delta u_1}{\Delta x_1}, \qquad e_{12} = \frac{\Delta u_1}{\Delta x_2}, \qquad e_{21} = \frac{\Delta u_2}{\Delta x_1}, \qquad e_{22} = -\frac{\Delta u_2}{\Delta x_2}, \tag{2.18}$$

As figure 2.6 suggests, elements e_{ij} with $i = j$ correspond to extensions or compressions along a certain direction, whereas elements with $i \neq j$ correspond to rotations. Indeed, the tensor can be written as the sum of a symmetric and an antisymmetric

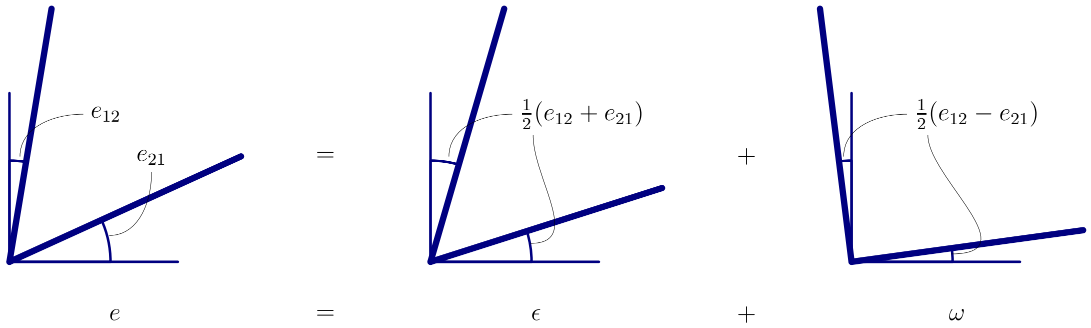

Figure 2.7: The relative displacement tensor, e_{ij}, can be written as the sum of a symmetric tensor, ϵ_{ij}, and an antisymmetric tensor, ω_{ij}. The symmetric tensor is defined to be the strain.

tensor

$$e_{ij} = \epsilon_{ij} + \omega_{ij}, \tag{2.19}$$

where

$$\epsilon_{ij} = \frac{1}{2}(e_{ij} + e_{ji}) \qquad \text{and} \qquad \omega_{ij} = \frac{1}{2}(e_{ij} - e_{ji}). \tag{2.20}$$

We illustrate this in figure 2.7, and see that the antisymmetric tensor ω_{ij} is a pure rotation tensor. We therefore define the symmetric part of e_{ij} as the strain using the expression given above.

These ideas are easily extended to three dimensions, resulting in a three dimensional strain tensor given by

$$\bar{\epsilon} = \begin{pmatrix} e_{11} & \frac{1}{2}(e_{12}+e_{21}) & \frac{1}{2}(e_{13}+e_{31}) \\ \frac{1}{2}(e_{21}+e_{12}) & e_{22} & \frac{1}{2}(e_{23}+e_{32}) \\ \frac{1}{2}(e_{31}+e_{13}) & \frac{1}{2}(e_{32}+e_{23}) & e_{33} \end{pmatrix}. \tag{2.21}$$

The elements on the diagonal are referred to as the *normal* strains, whereas the off-diagonal elements are referred to as the *shear* strains. Like the stress tensor described earlier, the symmetric nature of the strain tensor results in six independent strains: three normal and three shear elements.

2.1.7 Elastic and plastic behaviour

Imposing a stress on a crystal changes its shape. Provided the stress is below a certain limit the material will return to its original shape once the stress is removed. This behaviour is known as *elastic* behavior, and the limit below which it occurs is known as the elastic limit. When the material is behaving elastically, for small stresses the relationship between stress and strain is given by Hooke's law [51]

$$\epsilon_{ij} = s_{ijkl}\sigma_{kl}, \tag{2.22}$$

where s_{ijkl} is a fourth-rank tensor called the elastic *compliance* tensor. Alternatively we can write

$$\sigma_{ij} = c_{ijkl}\epsilon_{kl}, \tag{2.23}$$

where c_{ijkl} is a also fourth-rank tensor, called the elastic *stiffness* tensor.[5] Each of s and c have $3^4 = 81$ elements, however as there are symmetries in each of the stress and strain tensors, these symmetries are reflected in the stiffness and compliance tensors. For example, $\epsilon_{12} = \epsilon_{21}$, meaning that to avoid the introduction of arbitrary constants, we can set s_{12kl} and s_{21kl} to be equal. Therefore all $s_{ijkl} = s_{jikl}$ and $s_{ijkl} = s_{ijlk}$, and similarly for c_{ijkl}. Along with symmetries regarding the energy of a strained crystal [47], this reduces the number of independent elements in each tensor to 36.

As symmetries in each of σ, ϵ, s and c reduce the number of independent elements considerably, an alternative notation known as *Voigt* notation, can be used. Each

---

[5] We note that, counterintuitively, stiffness and compliance are labelled c and s respectively.

second-rank tensor is reduced to a 6-dimensional vector in the following way.

$$\bar{\sigma} = \begin{pmatrix} \sigma_{11} & \sigma_{12} & \sigma_{31} \\ \sigma_{12} & \sigma_{22} & \sigma_{23} \\ \sigma_{31} & \sigma_{23} & \sigma_{33} \end{pmatrix} = \begin{pmatrix} \sigma_1 & \sigma_6 & \sigma_5 \\ \sigma_6 & \sigma_2 & \sigma_4 \\ \sigma_5 & \sigma_4 & \sigma_3 \end{pmatrix} \rightarrow (\sigma_1, \sigma_2, \sigma_3, \sigma_4, \sigma_5, \sigma_6), \tag{2.24}$$

and

$$\bar{\epsilon} = \begin{pmatrix} \epsilon_{11} & \epsilon_{12} & \epsilon_{31} \\ \epsilon_{12} & \epsilon_{22} & \epsilon_{23} \\ \epsilon_{31} & \epsilon_{23} & \epsilon_{33} \end{pmatrix} = \begin{pmatrix} \epsilon_1 & \frac{1}{2}\epsilon_6 & \frac{1}{2}\epsilon_5 \\ \frac{1}{2}\epsilon_6 & \epsilon_2 & \frac{1}{2}\epsilon_4 \\ \frac{1}{2}\epsilon_5 & \frac{1}{2}\epsilon_4 & \epsilon_3 \end{pmatrix} \rightarrow (\epsilon_1, \epsilon_2, \epsilon_3, \epsilon_4, \epsilon_5, \epsilon_6). \tag{2.25}$$

This enables the stiffness and compliance tensors to be written with two indices, instead of four, using the same substitution. For each pair of indices ij, kl substitute

$$ij \rightarrow \begin{cases} 1, & i = j = 1, \\ 2, & i = j = 2, \\ 3, & i = j = 3, \\ 4, & ij = 23, 32, \\ 5, & ij = 31, 13, \\ 6, & ij = 12, 21. \end{cases} \tag{2.26}$$

At the same time, extra factors are introduced as such

$$\begin{aligned} s_{ijkl} &= s_{mn} \text{ when } m \text{ and } n \text{ are } 1, 2 \text{ or } 3, \\ 2s_{ijkl} &= s_{mn} \text{ when either } m \text{ or } n \text{ are } 4, 5 \text{ or } 6, \\ 4s_{ijkl} &= s_{mn} \text{ when both } m \text{ and } n \text{ are } 4, 5 \text{ or } 6. \end{aligned} \tag{2.27}$$

With these substitutions, the fourth-rank tensors c and s can be displayed as 6×6

matrices, containing 36 independent elements each. Additional symmetries of the lattice will reduce these further, and can result in only a few tensor elements being independent.

As an example we show explicitly the stiffness tensor for a cubic structure, which contains only three independent elastic compliance constants, s_{11}, s_{12} and s_{44}.

$$\bar{s}_{\text{cubic}} = \begin{pmatrix} s_{11} & s_{12} & s_{12} & 0 & 0 & 0 \\ s_{12} & s_{11} & s_{12} & 0 & 0 & 0 \\ s_{12} & s_{12} & s_{11} & 0 & 0 & 0 \\ 0 & 0 & 0 & s_{44} & 0 & 0 \\ 0 & 0 & 0 & 0 & s_{44} & 0 \\ 0 & 0 & 0 & 0 & 0 & s_{44} \end{pmatrix} . \tag{2.28}$$

For large elastic deformations, Hooke's law must be written in an incremental form

$$\Delta\epsilon_i = s_{ij}(\bar{\epsilon})\Delta\sigma_j, \qquad \Delta\sigma_i = c_{ij}(\bar{\epsilon})\Delta\epsilon_j, \tag{2.29}$$

where we make explicit that the elastic tensors depend on the current strain in the system. Macroscopic changes in stress and strain can be accounted for by integrating equation 2.29. In effect, this allows us to take into account behaviour such as a real material becoming less compressible the more we compress it.

Once the stress on a material exceeds the elastic limit, the material begins to behave plastically. Once plastic deformation has taken place, the material will no longer fully return to the pre-stressed state once the stresses have been removed. There are many forms of plastic behaviour: for example defects in the original crystal may enable some regions of the crystal to 'slip' [52] relative to other regions; or an entire region may change its lattice orientation relative to a neighbouring region, which is known as twinning [53, 54].

Alternatively, or additionally, some materials accommodate large external stresses by undergoing one or more phase changes [55], *i.e.* macroscopic rearrangements of the atoms to another lattice type. The archetypal example of this is the $\alpha \rightarrow \epsilon$ transition in iron, under which bcc (α) iron at ambient conditions changes to an hexagonal-close-packed (ϵ) structure as pressure is increased to above ~13 GPa [56, 57]. Under compression, the more closely packed arrangement of atoms in the ϵ-phase has a lower energy, enabling the crystal to accommodate the increased pressure.

2.2 X-ray diffraction

X-rays populate the region of the electromagnetic spectrum with wavelengths between approximately 100 eV and 100 keV, and corresponding wavelengths of 0.01 - 10 nm. As such, they have wavelengths on the same length scale as the interatomic distances in solid lattices, which are usually several to tens of Angstroms ($1\,\text{Å} = 10^{-10}\,\text{m}$).

2.2.1 Bragg's Law

One of the main equations of x-ray diffraction is known as Bragg's law [58]. The equation describes two photons reflecting specularly (in a mirror-like way) off two neighbouring planes of atoms, as shown in figure 2.8. We can see that the additional distance travelled by the lower photon is $2d\sin\theta$. In order that there is constructive interference between the two photons, this additional path length must be equal to an integer number of wavelengths of the photon. We therefore arrive at Bragg's law

$$n\lambda = 2d\sin\theta, \qquad \text{where} \qquad n = 1, 2, 3, ... \tag{2.30}$$

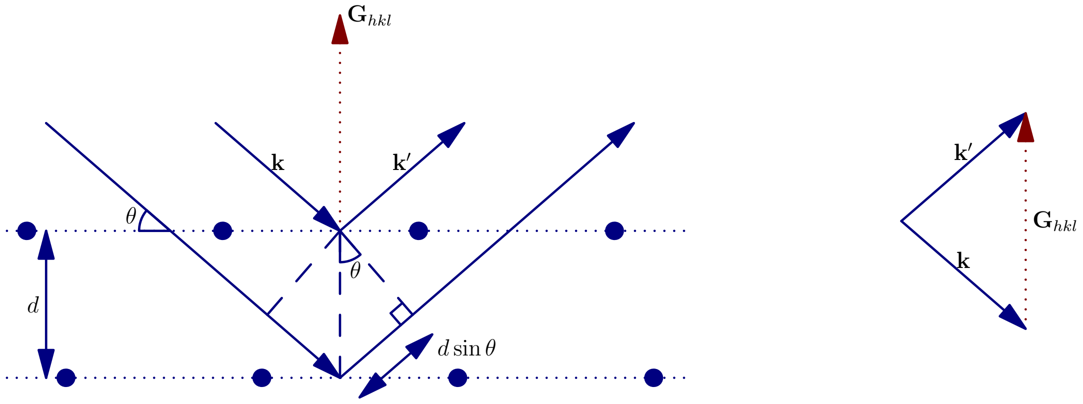

Figure 2.8: Illustration of Bragg's law of diffraction, and its equivalence to the Laue condition.

In this context the angle θ is known as the Bragg angle, often written θ_B. It should be noted that the total scattering angle, the change in direction between incoming and outgoing photons, is $2\theta_B$.

2.2.2 The Laue condition

A more general condition, known as the Laue condition, can be derived using Fermi's Golden Rule, as shown in the book by Simon [48]. This is given by

$$\mathbf{k}' - \mathbf{k} = \mathbf{G}_{hkl}, \qquad |\mathbf{k}'| = |\mathbf{k}| = \frac{2\pi}{\lambda}, \tag{2.31}$$

where the second expression necessitates that the scattering is elastic. To see that this is equivalent to Bragg's law, we note that from the geometry of figure 2.8

$$\hat{\mathbf{k}}' \cdot \hat{\mathbf{G}}_{hkl} = \cos(\tfrac{\pi}{2} - \theta) = \sin\theta = -\hat{\mathbf{k}} \cdot \hat{\mathbf{G}}_{hkl}, \tag{2.32}$$

where the circumflexes ($\hat{}$) denote unit vectors. Now assuming that the Laue condition is satisfied we can take the dot-product of each side of equation 2.31 with $\hat{\mathbf{G}}_{hkl}$, and using equation 2.11 we have

$$\frac{2\pi}{\lambda}(\hat{\mathbf{k}}' - \hat{\mathbf{k}}) \cdot \hat{\mathbf{G}}_{hkl} = \mathbf{G}_{hkl} \cdot \hat{\mathbf{G}}_{hkl}, \tag{2.33}$$

$$\frac{2\pi}{\lambda}(2\sin\theta) = |\mathbf{G}_{hkl}|, \tag{2.34}$$

$$2\, d_{hkl} \sin\theta = \lambda \tag{2.35}$$

which is Bragg's law for $n = 1$. For $n \neq 1$ we note that for every reciprocal lattice vector $\mathbf{G}_{hkl}$ describing planes with spacing d, there is another reciprocal lattice vector $n\mathbf{G}_{hkl}$ describing planes with spacing d/n. For a given incoming photon, described by the wavevector $\mathbf{k}$, diffraction will only produce outgoing wavevectors, $\mathbf{k}'$, which satisfy the Laue condition (eqn. 2.31).

2.2.3 Amplitude of scattering

X-rays being diffracted from atoms in a solid are scattered from the electrons. The amplitude of the scattering is related to the potential from the charge distribution of the electrons [48], and the potential is given by

$$V(\mathbf{x}) \sim \sum_{\text{atom } j \text{ in unit cell}} Z_j g_j(\mathbf{x} - \mathbf{x}_j), \tag{2.36}$$

where Z_j is the atomic number of the j^{th} atom and g_j is a short-range function that describes the electron charge distribution. Taking the Fourier transform of this potential we obtain

$$S(\mathbf{G}) \sim \sum_{\text{atom } j \text{ in unit cell}} f_j(\mathbf{G}) e^{i\mathbf{G}\cdot\mathbf{x}_j}, \tag{2.37}$$

where f_j is the Fourier transform of the potential and is known as the *atomic form factor*. $S(\mathbf{G})$ is the *structure factor* of the unit cell and is related to the diffracted intensity by

$$I(\mathbf{G}_{hkl}) \propto |S(\mathbf{G}_{hkl})|^2, \tag{2.38}$$

where we have included (hkl) to emphasise that if $\mathbf{G}$ is not a reciprocal lattice vector, the structure factor, and therefore the diffracted intensity, is zero. Calculating the diffracted intensity for the entire crystal involves convolving the unit-cell structure factor with delta functions at all the lattice points, and results in a finite constant that is normalisable in the full derivation given in the book by Simon [48].

We now calculate the structure factor for the three cubic lattice types. Using the relations between the conventional lattice vectors and the reciprocal lattice vectors, equation 2.8, we can write

$$\begin{align} S_{hkl} &= \sum_j f_j e^{i(h\mathbf{b}_1 + k\mathbf{b}_2 + l\mathbf{b_3})\cdot(x_j\mathbf{a}_1 + y_j\mathbf{a}_2 + z_j\mathbf{a_3})} \tag{2.39} \\ &= \sum_j f_j e^{2\pi i(hx_j + ky_j + lz_j)}, \tag{2.40} \end{align}$$

where $[x_j, y_j, z_j]$ are the coordinates of atom j, in terms of the three lattice vectors.

For simple cubic, with a single atom on each lattice point this just gives $S(\mathbf{G}) = f$. For bcc, with atoms at coordinates relative to the simple cubic lattice of [0,0,0] and $[\frac{1}{2}, \frac{1}{2}, \frac{1}{2}]$, we have

$$S_{hkl} = f(1 + e^{i\pi(h+k+l)}) = f(1 + (-1)^{h+k+l}). \tag{2.41}$$

It is evident that the structure factor, and therefore the diffracted intensity, reduces to zero if $h + k + l$ is an odd number. These "forbidden" reflections are known as

Structure	Allowed reflections	Forbidden reflections
simple cubic	any h, k, l	none
bcc	$(h+k+l)$ even	$(h+k+l)$ odd
fcc	h, k, l all even, or all odd	h, k, l mixed even/odd
cd	h, k, l all odd, or all even with $(h+k+l)=4n$	h, k, l mixed even/odd, or h, k, l all even with $(h+k+l)\neq 4n$

Table 2.1: Selection rules for calculating whether a given reflection is forbidden or allowed.

systematic absences, and the rule that governs them a *selection rule.* For fcc lattices, with an atoms at [0,0,0], $[\frac{1}{2}, \frac{1}{2}, 0]$,$[\frac{1}{2}, 0, \frac{1}{2}]$ and $[0, \frac{1}{2}, \frac{1}{2}]$, the structure factor is

$$S_{hkl} = f(1 + e^{i\pi(h+k)} + e^{i\pi(h+l)} + e^{i\pi(k+l)}), \tag{2.42}$$

which vanishes unless h, k, l are all even or all odd. These results are summarised in table 2.1, along with the selection rules for cubic diamond.

The fact that certain planes do not diffract is not intuitive, but can easily be explained by returning to the *primitive* lattice vectors. By choosing to think of the bcc and fcc lattices in terms of conventional unit cells, we introduced “extra” atoms to the unit cells, which are included in the sum to calculate the structure factor. However, it is still physically the same lattice, and so our choice of unit cell should not create any additional planes. To illustrate this we show several conventional planes in table 2.2, and calculate whether they produce allowed or forbidden reflections. Also included in the table are the Miller indices of the planes in units of the primitive lattice vectors.

We can see a clear pattern in table 2.2: any reflection that is forbidden by a selection rule corresponds to non-integer Miller indices, when measured relative to the primitive lattice vectors. The selection rules work to remove the additional planes

Conventional lattice vectors	bcc		fcc	
(hkl)	allowed	$(hkl)^{\text{bcc}}$	allowed	$(hkl)^{\text{fcc}}$
(100)		$(\frac{1}{2}\frac{\bar{1}}{2}\frac{1}{2})^{\text{bcc}}$		$(\frac{1}{2}0\frac{1}{2})^{\text{fcc}}$
(110)	✓	$(100)^{\text{bcc}}$		$(1\frac{1}{2}\frac{1}{2})^{\text{fcc}}$
(111)		$(\frac{1}{2}\frac{1}{2}\frac{1}{2})^{\text{bcc}}$	✓	$(111)^{\text{fcc}}$
(200)	✓	$(1\bar{1}1)^{\text{bcc}}$	✓	$(101)^{\text{fcc}}$
(210)		$(\frac{3}{2}\frac{\bar{1}}{2}\frac{1}{2})^{\text{bcc}}$		$(\frac{3}{2}\frac{1}{2}1)^{\text{fcc}}$
(211)	✓	$(101)^{\text{bcc}}$		$(\frac{3}{2}1\frac{3}{2})^{\text{fcc}}$
(220)	✓	$(200)^{\text{bcc}}$	✓	$(211)^{\text{fcc}}$
(221)		$(\frac{3}{2}\frac{1}{2}\frac{1}{2})^{\text{bcc}}$		$(2\frac{3}{2}\frac{3}{2})^{\text{fcc}}$
(222)	✓	$(111)^{\text{bcc}}$	✓	$(222)^{\text{fcc}}$
(300)		$(\frac{3}{2}\frac{\bar{3}}{2}\frac{3}{2})^{\text{bcc}}$		$(\frac{3}{2}0\frac{3}{2})^{\text{fcc}}$

Table 2.2: “Forbidden” reflections are just conventional lattice planes that correspond to non-integer Miller indices when expressed in terms of the primitive lattice vectors.

we introduced when moving from the primitive to the conventional unit cell.

Unlike solid structure factors, liquid structure factors do not exhibit sharp peaks. This is due to the absence of long-range order in liquids. However, some short range order is present in liquids, meaning that diffraction from liquids is still possible. In general, the diffraction patterns obtained from liquids contain much broader diffraction peaks than those obtained from solids.

2.2.4 Diffraction in experiments

Bragg’s law dictates that for a given wavelength of x-rays, only certain angles of incidence will result in diffraction from a single crystal sample. This suggests two clear options for measuring diffraction experimentally: use polychromatic x-rays and fix the angle of incidence; or use monochromatic x-rays but vary the angle of incidence. Perhaps the simplest method for varying the angle of incidence on the sample, at least in laser shock experiments, is the so-called *diverging beam* geometry [59, 60], where x-rays from a monochromatic point-source diverge and so hit the sample at a range of angles. Two further methods that are used later in this work are Laue diffraction, and powder diffraction, which we will describe here in turn.

2.2.4.1 Laue diffraction

The Laue diffraction method [58, 61, 62] uses a broadband x-ray source incident on a fixed single crystal target. The source is collimated, allowing a single angle of incidence on the sample. For a given plane (hkl), the interplanar spacing and Bragg angle are known, so the wavelength allowed by Bragg's law to diffract is known. If this wavelength is contained in the broadband incident spectrum, diffraction will be seen from that plane. This diffraction is then recorded on a detector, typically either photographic film, image plate, or a CCD. If the spectrum of the source is known, the relative spacings and orientations of the planes can be calculated from the diffraction pattern, enabling a determination of unknown lattice types.

2.2.4.2 Powder diffraction

Alternatively, one can use a monochromatic x-ray source, and vary the angle of incidence with the crystal. This is often achieved by using a different type of sample, which is no longer a single crystal. If a powder target is used [63, 64, 65], that is, one with many small, randomly-oriented, single crystals, then many (ideally every) orientation is present for each plane. This allows many more families of planes to diffract from a collimated monochromatic source, and indeed the multiplicity of the family can be implied from the relative intensity of the recorded diffraction. Polycrystalline samples diffract similarly to powder targets, however their crystalline grains ofter have a preferred orientation, and so the assumption that every orientation is present is sometimes not accurate.

2.2.5 The Ewald sphere

Returning to the Laue condition, we have two criteria for x-ray diffraction: that the incoming and outgoing photons must have the same energy, and that the difference in their k-vectors must be a reciprocal lattice vector. The first can be displayed graphically using a construction known as the Ewald sphere [66]. This is a sphere, of radius $|\mathbf{k}|$, centred on the start of the incoming $\mathbf{k}$ vector: it is the locus of all outgoing $\mathbf{k}'$ vectors that fulfil the requirement for elastic scattering. If we locate this Ewald sphere so that the end of the incoming $\mathbf{k}$ vector is at the origin of the reciprocal lattice, then any reciprocal lattice vector, $\mathbf{G}_{hkl}$, that intersects the sphere fulfils the full Laue condition. This is shown in two dimensions in figure 2.9a.

For a broadband x-ray source with photon energies between $E(\mathbf{k}_{\mathrm{min}})$ and $E(\mathbf{k}_{\mathrm{max}})$, two Ewald spheres are constructed with radii $|\mathbf{k}_{\mathrm{min}}|$ and $|\mathbf{k}_{\mathrm{max}}|$, centred on the start of their k-vectors respectively, as shown in figure 2.9b. Any reciprocal lattice point outwith the smaller sphere, but within the larger, produces diffraction.

Finally, for a powder target, as the crystallites are oriented randomly, each reciprocal lattice point is rotated 4π about the origin, producing a sphere for each $\mathbf{G}_{hkl}$. This is shown in figure 2.9c. The geometric intersection between two spheres is a circle, and so the diffraction pattern produced by monochromatic x-rays incident on a powder sample is a series of rings known as Debye-Scherrer rings: one for each intersection between a $\mathbf{G}_{hkl}$ sphere and the Ewald sphere.

Geometric constructions of this type can be extremely useful in determining whether or not diffraction is allowed for certain geometries, and if so, predicting the diffraction patterns expected in experiment. They will be used extensively in the rest of this work.

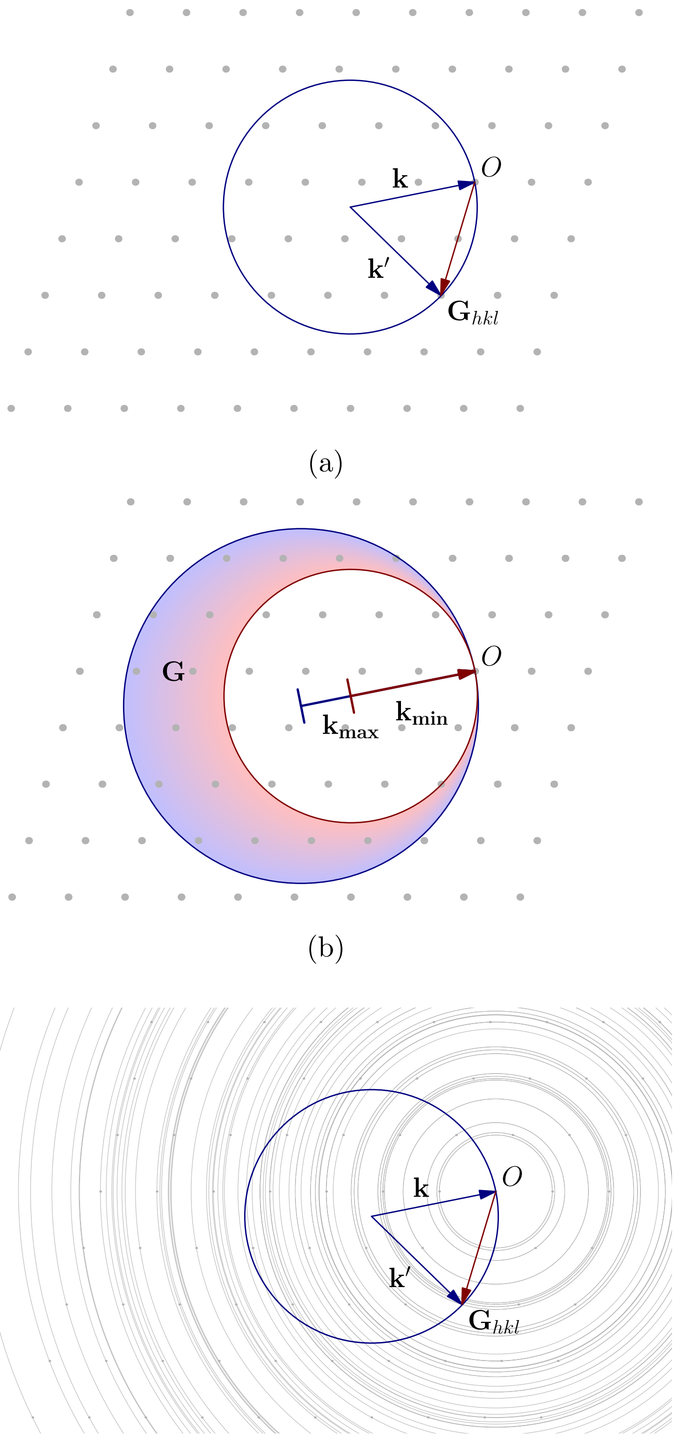

(a)

(b)

(c)

Figure 2.9: Ewald sphere construction (shown in 2D) for three different experimental setups: (a) monochromatic x-rays, single crystal; (b) Laue diffraction - broadband x-rays, single crystal; and (c) Powder diffraction - monochromatic x-rays, powder target. For (c) the original reciprocal lattice points associated with each $\mathbf{G}_{hkl}$ sphere are still shown.

2.3 Shock waves

A shock wave is defined mathematically as a disturbance propagating through a material that causes a discontinuity in some physical property, such as pressure, density, or internal energy [49]. The discontinuity is called the shock front. In solids, due to the discrete nature of the lattice, the shock front is not a true discontinuity, but a *steady-state* wave with a length scale of some number of lattice spacings. In fluids, the shock thickness is limited by the ion-ion collisional mean free path.

2.3.1 The Rankine-Hugoniot equations

The equations that govern the shock are known as the Rankine-Hugoniot equations [67, 68]. To derive them we consider a piston pushing on a cylinder of material, with cross-sectional area A, as shown in figure 2.10. At time $t \leq 0$ the cylinder is at ambient conditions with pressure, density and internal energy of P_0, ρ_0 and E_0 respectively. At time $t = 0$ the piston begins to push on the cylinder at constant velocity U_p, usually termed the particle velocity. At a later time dt, material in front of the piston has been compressed and has pressure, density and internal energy of P, ρ and E respectively.

Across the shock front, which travels forward into the material at speed U_s, mass, momentum and internal energy must be conserved, and we consider each of these in turn. The volume of material behind the shock front at $t = dt$ is $(U_s - U_p)\, A\, dt$, as shown in the figure, and so the corresponding conservation of mass equation, once we have eliminated the common factor $A\, dt$, is

$$\rho_0 U_s = \rho(U_s - U_p). \tag{2.43}$$

Conservation of momentum requires that the difference in momentum is equal to the

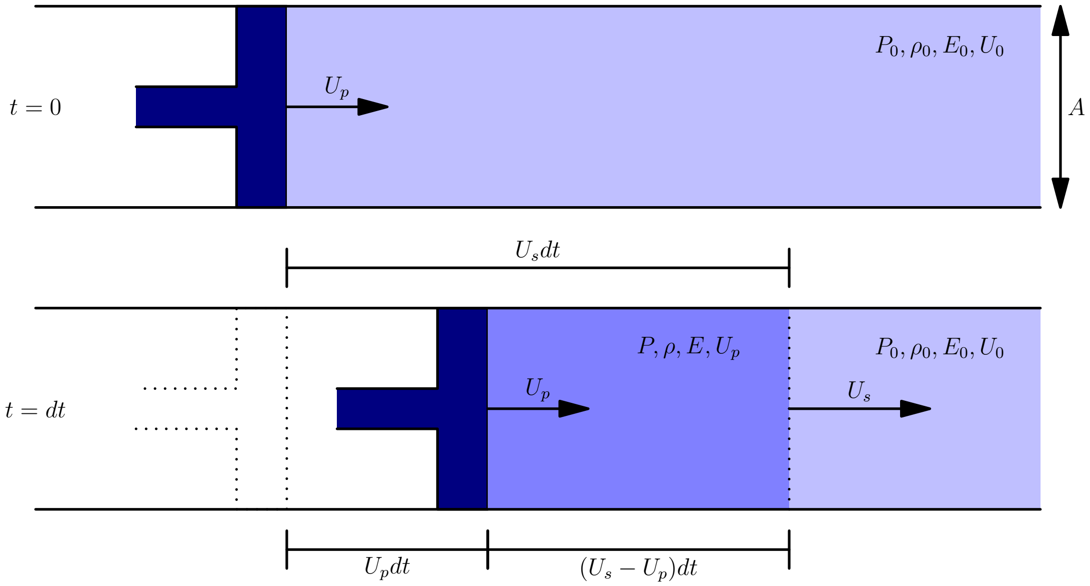

Figure 2.10: A cylinder, of cross-sectional area A, onto which a piston acts. The properties of the material are shown: pressure, P, density, ρ and internal energy, E; in the undisturbed material (subscript 0) and behind the shock front (no subscript). Also labelled are the piston (or particle) velocity, U_p, and the shock velocity, U_s.

impulse provided by the piston

$$\text{Impulse:} \qquad F dt = (P - P_0) A dt, \tag{2.44}$$

$$\text{Difference in momentum:} \qquad \underbrace{\rho(U_s - U_p)Adt}_{\text{mass}} \; \underbrace{U_p}_{\text{velocity}} - \underbrace{\rho_0(U_s - U_0)Adt}_{\text{mass}} \; \underbrace{U_0}_{\text{velocity}=0}. \tag{2.45}$$

Equating these we arrive at

$$(P - P_0) = \rho(U_s - U_p)U_p, \tag{2.46}$$

and by using equation 2.43

$$(P - P_0) = \rho_0 U_s U_p. \tag{2.47}$$

Finally, the conservation of energy equates the difference in the work done by P and

P_0 to the change in total energy (kinetic plus internal)

$$\text{Difference in work:} \qquad \underbrace{(PA)}_{\text{force}}\ \underbrace{U_p dt}_{\text{distance}}\ -\underbrace{(P_0A)}_{\text{force}}\ \underbrace{U_0 dt,}_{\text{distance}=0} \tag{2.48}$$

$$\text{Difference in energy:} \qquad \underbrace{\tfrac{1}{2}\{\rho A(U_s-U_p)dt\}U_p^2}_{\text{kinetic}}+\underbrace{EA\rho(U_s-U_p)dt-E_0A\rho_0U_sdt.}_{\text{internal}} \tag{2.49}$$

Equating these yields

$$PU_p=\tfrac{1}{2}\rho(U_s-U_p)U_p^2-E_o\rho_0U_s+E\rho(U_s-U_p), \tag{2.50}$$

again by using equation 2.43 we have

$$PU_p=\tfrac{1}{2}\rho_0U_sU_p^2+\rho_0U_s(E-E_0), \tag{2.51}$$

which can be rearranged into the form

$$E-E_0=\tfrac{1}{2}(P+P_0)(V_0-V), \tag{2.52}$$

where $V=1/\rho$ is the specific volume. So the three Rankine-Hugoniot equations that describe the conditions before and after the shock wave are

$$\text{Mass:} \qquad \rho_0U_s=\rho(U_s-U_p), \tag{2.53}$$

$$\text{Momentum:} \qquad (P-P_0)=\rho_0U_sU_p, \tag{2.54}$$

$$\text{Energy:} \qquad E-E_0=\tfrac{1}{2}(P+P_0)(V_0-V). \tag{2.55}$$

These three equations contain five independent variables, and so to calculate all parameters as a function of one of them, an additional equation is needed. This additional equation is known as the *equation of state* (EOS) and is often considered as a relationship between U_s and U_p

$$\text{EOS:} \qquad U_s=C_0+S_1U_p+S_2U_p^2+... \tag{2.56}$$

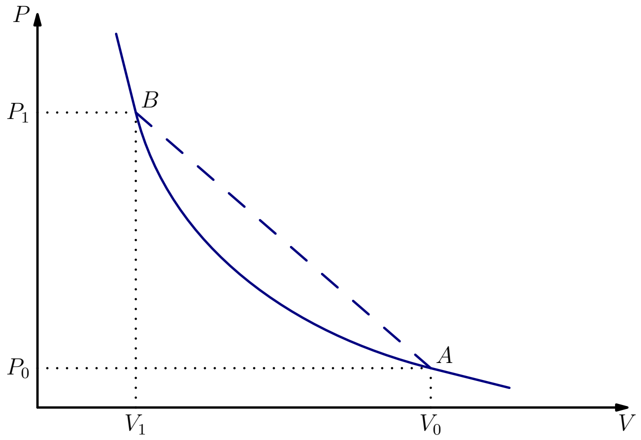

Figure 2.11: Illustration showing a schematic of the ideal gas Hugoniot (solid blue), and the Rayleigh line (dashed blue).

where C_0 is the sound velocity in the material at zero pressure, and S_i are empirical parameters.

2.3.2 The Hugoniot

Once both the equation of state and initial conditions are known, one can calculate the final conditions after a shock. The locus of all possible final conditions is known as the Hugoniot. For the simple case of an ideal gas, the EOS is given by

$$E = \frac{PV}{\gamma - 1}, \tag{2.57}$$

where the adiabatic index, γ, is the ratio of specific heats at constant pressure and constant volume. Substituting this into the Rankine-Hugoniot equation for energy (eqn. 2.55) and rearranging gives

$$P = \frac{(\gamma+1)V_0 - (\gamma-1)V_1}{(\gamma+1)V_1 - (\gamma-1)V_0} P_0, \tag{2.58}$$

$$P = H(P_0, V_0, V_1). \tag{2.59}$$

The curve defined by H is precisely the Hugoniot curve described above, and is sketched in figure 2.11. It should be stressed that the Hugoniot is not the path that the material takes through P-V space, but the locus of all possible points that are accessible by a single shock from the start conditions $(A : P_0, V_0)$. For an infinitely thin shock, the material jumps discontinuously from the initial conditions to the final conditions $(B : P_1, V_1)$. The straight line that connects A and B is called the Rayleigh line and is related to the shock velocity, U_s. From the equations above we find

$$\frac{P_1 - P_0}{V_1 - V_0} = -\rho_0^2 U_s^2. \tag{2.60}$$

If (P_0, V_0) are ambient conditions, the Hugoniot is known as the principal Hugoniot. If the material experiences a second shock after reaching point B, a second Hugoniot, different from the first, passes through B and defines all points accessible by the second shock.

2.3.3 Shock waves in solid materials

The Hugoniot described above is for a fluid, that is, a material that does not allow any shear stresses or strains, and relaxes completely when any external stresses are imposed upon it. In solids, as discussed previously, small stresses may be accommodated elastically, while larger stresses cause plastic deformation or phase changes to occur. The boundary between these two responses is the Hugoniot elastic limit (HEL), which was previous introduced as simply the elastic limit. Below this boundary, a single shock creates an elastic wave moving through the material. Just above this limit, a two-wave profile occurs, where an initial elastic precursor wave takes the material to P_{HEL} and a second, slower plastic wave takes the material to its final conditions. If the pressure of the shock is increased further, a wave structure emerges with a single, plastic shock. The two latter phenomena are often referred to as weak and strong shocks respectively. The pressure that separates these two cases is labelled P_{OD} in figure 2.12, signifying the boundary of *over-driven*, strong shocks.

To see why these three different forms of wave profile can occur, we consider the respective shock velocities. As described previously the shock velocity is related to the negative gradient of the Rayleigh line. For any wave with $P<P_{HEL}$, the Rayleigh line has the same gradient, as shown in figure 2.12, and so an elastic wave always travels at the same velocity, the sound velocity, C_0. Once the HEL is exceeded, the initial wave still travels at C_0, but a second wave follows it more slowly, at a wave velocity determined by the Rayleigh line *from* the HEL *to* the final conditions (the green dashed line in fig. 2.12). The velocity of a strong shock depends only on the slope of its single Rayleigh line (the red dashed line) and is independent of the sound velocity.

If we acknowledge that in real materials the elastic constants are strain dependent (eq. 2.29), the portion of the hugoniot up to the HEL also becomes slightly concave. This means that higher amplitude elastic waves travel marginally faster than C_0 (now defined as the negative gradient of the hugoniot at $P = 0$), and so even elastic waves steepen into a shock as they pass through the material.

In experiments, the HEL is often much lower than the pressure range being investigated, meaning they are carried out in a strong shock regime, and so purely plastic (or phase change) responses are seen. However, with the work in this thesis, the pressures explored are in the weak regime for silicon, and so elastic precursor waves will be present. In addition for single crystals, the value of the HEL is dependent on the direction of the pressure wave relative to the orientation of the crystal [17, 18]. Finally, preexisting defects in the crystal structure can act to lower the HEL [69, 70] and expedite plastic relaxation [71, 72].

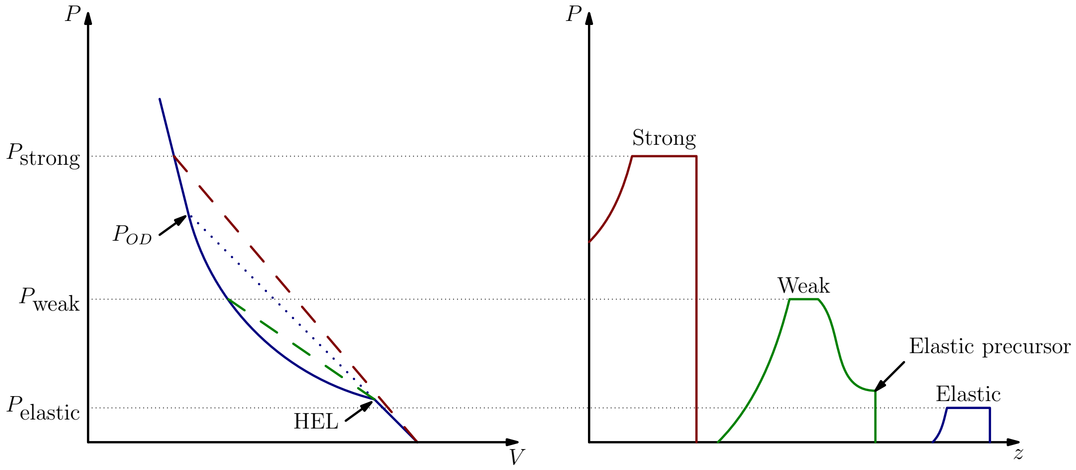

Figure 2.12: Illustration showing (right) the wave profile of elastic (blue), weak- (green) and strong-shocks (red). Also shown (left) is a schematic Hugoniot for a solid (solid blue), showing the HEL after which plastic deformation occurs, and the Rayleigh lines for weak- (dashed green) and strong-shocks (dashed red). The pressure, P_{OD}, which separates the weak and strong regimes is highlighted on the left plot.

2.3.4 Wave interactions at material boundaries

When a pressure wave travelling through a material encounters a boundary with a different material, some of the wave can be reflected. The property that affects the magnitude of this interaction is the *impedance*, given by $\rho_0 U_s$ for each material. If two materials have the same impedance, the pressure wave is not affected by the boundary, but if there is an impedance mismatch, the wave profile will be altered. For example, if a wave travels from a material with low impedance to a material with high impedance, the resulting pressure in the second material is higher than in the first. The size of this increase can be calculated using by plotting the P-U_p curves of the two materials, as shown in figure 2.13. Conversely, if a wave travels from a material of high impedance to a material of low impedance, the pressure in the second material will be lower than in the first. These considerations are important for calculating the pressure profiles in multi-layered samples, such as those used in chapter 4.

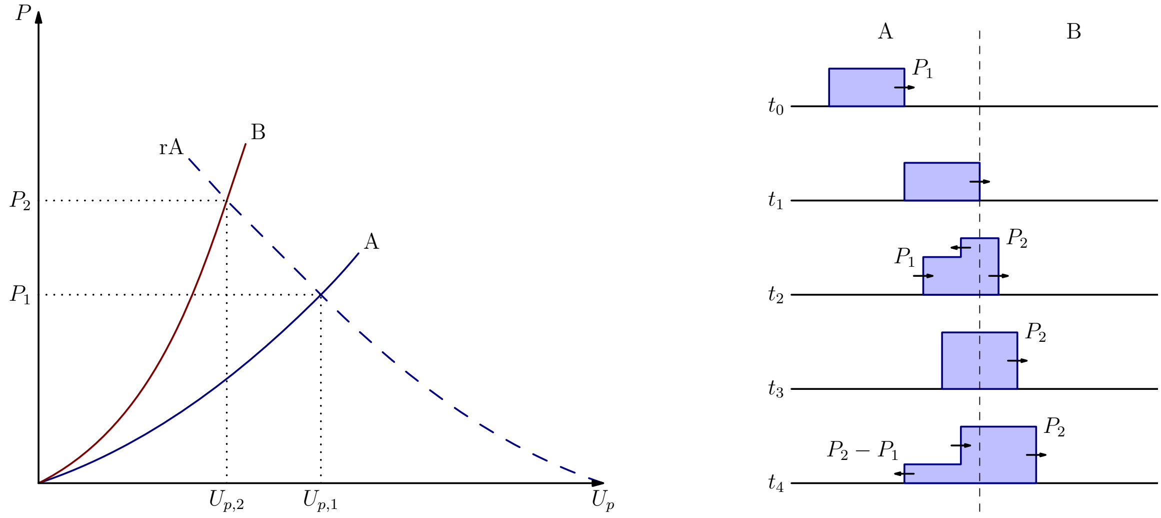

Figure 2.13: Illustration of the increase in pressure when a wave of pressure P_1 travels from a material of lower impedance (A) to a material of a higher impedance (B). The left-hand subfigure shows the P - U_p curves for the two materials (A and B), and the reflected curve (rA), which is curve A reflected horizontally about the point $(P_1, U_{p,1})$. The final pressure, P_2, of the wave in material B is given by the intersection of the curves rA and B. The right-hand subfigure shows the pressure wave travelling from left to right across the boundary as time increases from t_0 to t_5. Figure adapted from reference [49].

2.4 Simulating solids computationally

Among the various schemes for simulating the behaviour of solids, two methods that are used extensively are hydrodynamic modelling and molecular dynamics modelling. As the two methods approach the problems of modelling solids from very different standpoints, each have their own benefits. We give a brief introduction to each method here.

2.4.1 Hydrodynamic codes

Hydrodynamic codes (hydrocodes) [73], in the first instance, model the behaviour of fluids by solving conservation equations for mass, momentum and energy

$$\frac{\partial \rho}{\partial t} + \rho \nabla \cdot \mathbf{u} = 0, \tag{2.61}$$

$$\rho \frac{\partial \mathbf{u}}{\partial t} = -\nabla P + \mathbf{f}, \tag{2.62}$$

$$\rho \frac{\partial \epsilon}{\partial t} + P(\nabla \cdot \mathbf{u}) = 0, \tag{2.63}$$

where ρ is the mass density, $\mathbf{u}$ is the local fluid velocity, P is the hydrostatic pressure of the fluid, $\mathbf{f}$ is an external force acting on the fluid (often assumed to be zero) and ϵ is the internal energy. These equations describe the changes in motion and energy of an inviscid, nonconducting fluid [74]. In order to simulate more complicated materials, such as solids, additional equations are necessary, which will be discussed in due course.

2.4.1.1 Eulerian and Lagrangian formulations

As the computers that are being used to run the simulations have a finite memory, but the fluid is a continuous material, moving through continuous time, a discretisation of both time and space are necessary to make the problem tractable. As such, the simulation is divided into small spatial *cells* that make up a grid, each of which has a single defined value of each material parameter, P, ρ, etc. In general, the higher the resolution of these cells, the better the simulation will match the physical behaviour. Similarly, time must be discretised, and the simulation will jump from one time-step to the next. Again, the shorter the time-step of the simulation, the better the simulation will handle short timescale phenomena.

There are two main schemes for discretising the space, known as the Eulerian and Lagrangian formulations [73]. In essence, they differentiate between choosing a grid that stays fixed in space as the material moves through it (Eulerian) or choosing a grid that stays fixed to the material and deforms with it during the simulation (Lagrangian). In general, this means Eulerian hydrocodes must have a larger number of cells to accommodate movement of the material throughout the simulation. In addition, accurate modelling of free surfaces relies heavily on the spatial resolution of the simulation, as a free surface will jump from one cell boundary to the next as the material moves. In contrast, as the free surfaces will lie along fixed cell boundaries in Lagrangian codes this issue is not as great. However, as the cell boundaries move with the material in the Lagrangian formalism, if there is severe deformation of the material, the cells too will be deformed, causing problems with some of the assumptions of cell shape in the underlying equations. Furthermore, if turbulence in the fluid is anticipated, the grid can become extremely contorted, leading to similar issues. To illustrate these points, schematic Eulerian and Lagrangian grids overlaid on an initially-straight material boundary are shown in figure 2.14.

For simulating solids, as these extreme deformations are less likely to occur, and simulations with fewer cells are more efficient, the Lagrangian formalism is often preferred, and the code introduced in chapter 3 uses this method.

While uniform Eulerian or Lagrangian meshes are two of the simplest techniques

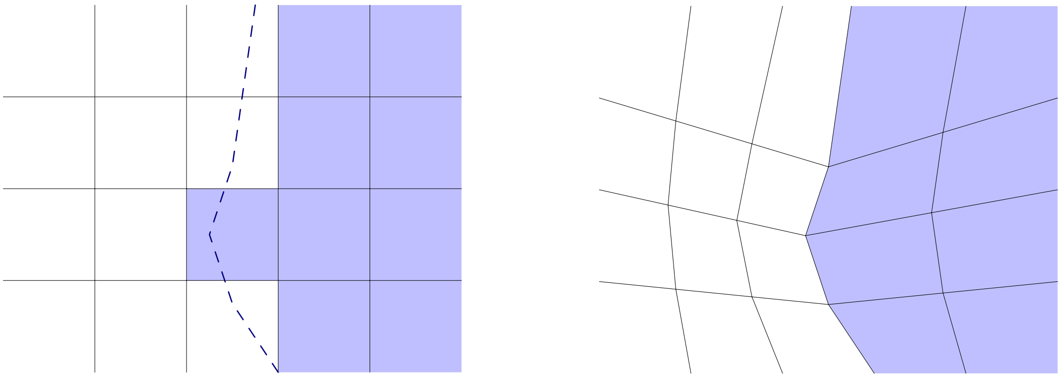

(a) Eulerian (b) Lagrangian

Figure 2.14: Schematic of (a) Eulerian and (b) Lagrangian grids in a 2d hydrocode, overlaid on an initially-straight material boundary being simulated. The Eulerian grid in this case cannot accurately capture the shape of the boundary, whereas the Lagrangian grid is fixed to the original boundary, and so moves with it.

used in hydrodynamic codes, it is possible to improve the efficiency, and scaling capabilities, by using a method known as Adaptive Mesh Refinement (AMR) [75]. In this case a non-uniform grid is created, whereby regions of the simulation which require the highest resolution (for example turbulent regions or boundaries between materials) are modelled by a grid with a higher spatial resolution. In contrast, regions of the sample with simpler behaviour are modelled with a courser grid. By dynamically adapting the grid as the simulation progresses, one can ensure regions of complicated behaviour are modelled accurately, while regions of simple behaviour still run efficiently.

2.4.1.2 Resolution and the Courant and Cauchy conditions

Once the choice of Eulerian vs Lagrangian frame has been made, successful hydrocodes must be temporal and spatial resolution independent. That is, the simulated behaviour of the material must not change considerably as the resolution is increased or decreased. This imposes requirements on the underlying equations to be unit-less in terms of time and space. In addition to this, the choice of temporal and spatial resolutions are not completely independent, as can be seen by the often used Courant [76, 77] and Cauchy conditions

$$\Delta t_{Courant} < \min\left(\frac{\Delta x}{C}\right), \tag{2.64}$$

$$\Delta t_{Cauchy} < \min\left(\frac{\Delta x}{|u|}\right). \tag{2.65}$$

where Δt is the time-step, Δx is the spatial resolution, C is the speed of sound and $|u|$ is the particle speed. Taking the minima over all cells ensures that the most demanding conditions are met. The condition given in equation 2.64 dictates that the choice of time-step must be small enough that a sound wave cannot travel the full width of a spatial cell in one time-step. The condition given in equation 2.65 requires that fluid can not be moved more than the width of a spatial cell within a single time-step.

2.4.1.3 Artificial viscosity

One problem that is particularly prevalent in simulations that may include shock waves, is that by our previous mathematical description a shock wave is a discontinuous change in material parameters. Even when we acknowledge that the shock front has a finite width, this rapid change in pressure and density can cause fast-growing numerical oscillations in hydrocodes, specifically when the shock front width is on the order of the computational cell width. As increasing the spatial-resolution of the simulation indefinitely is impossible, a method for minimising this effect was developed, firstly by Von Neumann and Richtmyer [78], and is known as *artificial viscosity*. Essentially, the artificial viscosity introduces additional damping and increases the width of the shock front to several cell widths, while damping the resonant oscillations. An illustration of this artificial viscosity and the reduction in shock front instability is shown in figure 2.15.

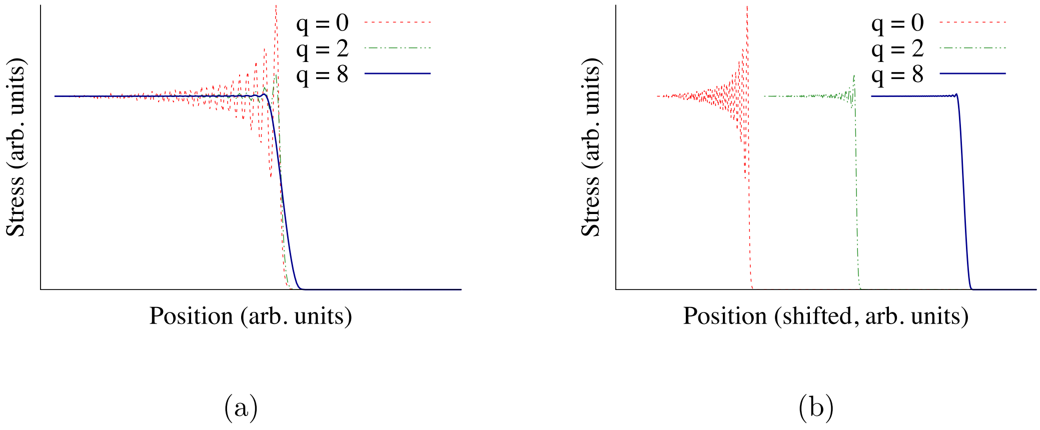

(a) (b)

Figure 2.15: Illustration of how the numerical instabilities at the shock front are affected by increasing the artificial viscosity coefficient, q. (a) Three elastic wave fronts with varying values of q and (b) the same three waves shifted in position for clarity. Note the increasing width, and decreasing slope, of the shock front in subfigure (a).

2.4.1.4 Material strength models

As the underlying equations of hydrocodes discussed so far are all fluid equations, additional models are required to simulation solid behaviour [79, 80, 81], for example elastic behaviour followed by plastic yielding [82]. For this, the hydrostatic pressure in equation 2.62 must be replaced with a full stress tensor

$$\rho \frac{\partial \mathbf{u}}{\partial t} = -\nabla \cdot \bar{\sigma} + f. \tag{2.66}$$

In addition to this change, four further relationships are necessary: 1) a stress-strain relationship connecting changes in stress with changes in elastic strain; 2) a flow equation that dictates the rate of change of plastic strain; 3) a criterion that defines the boundary between elastic and plastic flow; and possibly 4) a hardening rule that relates the current stress to the plastic deformation history [83]. Clearly any attempt to improve the physical processes modelled by the code has a stark effect on the complexity of the underlying equations.

2.4.2 Molecular dynamics codes

An alternative simulation technique is Molecular dynamics (MD), whereby individual atoms are simulated, rather than assuming a continuous material as in hydrocodes. Before a given time-step, the position, $\mathbf{r}_i$, and velocity, $\mathbf{v}_i$, of all N atoms is known, and the force on each atom is calculated using Newton's second law:

$$\mathbf{F}_i(\mathbf{r}_1, \mathbf{r}_2, ..., \mathbf{r}_N) = m_i \frac{d^2\mathbf{r}_i}{dt^2}. \tag{2.67}$$

This force acts on the i^{th} atom for a time-step Δt, after which the position and velocity of the atom are updated. The process is repeated for every atom and the next time-step begins. The main difficulty with MD lies in creating accurate interatomic potentials, which define the force each atom imposes on its neighbours, and indeed, creating and improving these potentials is still an area of active research [84, 85]. For a given set of initial and boundary conditions, the final state of the atoms is found by simply by integrating the equations of motion forward in time until the desired amount of time has passed.

One intrinsic feature of MD that is extremely useful to the work presented here the ability to simulate diffraction patterns. As the position of every atom is known at each time-step, a diffraction pattern can be calculated using the principles given in previous sections.

2.4.2.1 The LAMMPS code

The molecular dynamics code that we use in this work is the "Large-scale atomic/ molecular massively parallel simulator" (LAMMPS), which was developed at Sandia National Laboratories [86]. This code can simulate up to billions of interacting atoms [87], and by using processors in parallel reduces computational time drastically. The code integrates the motion of the atoms forward in time using the Verlet velocity algorithm [88, 89]. For a given time-step the position and velocity of each atom are updated as follows.

$$\mathbf{r}(t+\Delta t) = \mathbf{r}(t) + \mathbf{v}(t)\Delta t + \frac{1}{2}\mathbf{a}(t)\Delta t^2, \tag{2.68}$$

$$\mathbf{a}(t+\Delta t) = \frac{-\nabla V\big(\mathbf{r}(t+\Delta t)\big)}{m}, \tag{2.69}$$

$$\mathbf{v}(t+\Delta t) = \mathbf{v}(t) + \frac{1}{2}\mathbf{a}(t)\Delta t + \frac{1}{2}\mathbf{a}(t+\Delta t)\Delta t, \tag{2.70}$$

Our simulations generally consist of a long, square-ended cuboid which is shocked uniaxially along the extended direction. We use periodic boundary conditions in the two short directions, meaning atoms on one boundary of the simulation box interact with atoms on the opposite boundary, eliminating edge effects[6]. The boundaries of the long dimension are free boundaries, upon one of which a force is applied to simulate a piston.

2.4.2.2 Simulating diffraction from MD

As mentioned previously, a major benefit of MD is the ability to simulate diffraction patterns directly from the atom positions. In order to do this a Fourier transform of the positions must be taken, effectively converting the real lattice into a reciprocal lattice. In the work presented here a discrete Fourier transform is used. The intensity at $\mathbf{k}$ is given by

$$|F(\mathbf{k})|^2 \propto \left| \sum_{j}^{N} e^{i\mathbf{k}\cdot\mathbf{r}_j} \right|^2, \tag{2.71}$$

$$\tag{2.72}$$

---

[6] Despite the use of periodic boundaries, the transverse dimension of the simulation will have an effect [90].

where $\mathbf{r}_j$ is the position of the j^{th} atom, and the sum is over all atoms. This assumes that the atoms are delta functions centred on their position $\mathbf{r}_j$. An alternative technique would be to use the fast Fourier transform method developed for increased efficiency by Kimminau *et al.* [91].

Chapter 3

The Lagrangian Elastic Code

Many of the current methods for simulating solid materials rely on hydrodynamics codes, or hydrocodes. The underlying equations in hydrocodes are valid for inviscid, nonconducting fluids. In order to simulate solid materials, additional models are required which hinder the fluid flow in some way, as introduced in chapter 2.

To approach the problem from an alternate angle, we here introduce a code which assumes an elastic, solid response from the outset, and uses additional models to allow later yielding. This ensures that the primary behaviour of the material is that of a simple solid, before other material responses, such as plasticity or phase changes, are allowed to occur.

As the majority of work in this thesis concerns experiments on single crystal silicon, the code introduced here is focussed on the phase change between ambient cubic diamond silicon and the high pressure β-tin (β-Sn) phase. It was developed, in part, to aid in the analysis of the data introduced in chapter 4. In principle, the code could be adjusted to not only model other phase changes, but also to accept mixed-phase regions of more than two phases.

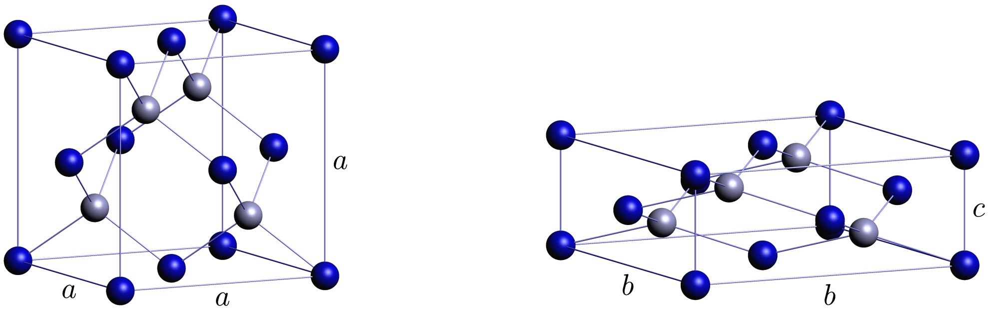

(a) Cubic diamond (cd) (b) Beta (β)

Figure 3.1: The two Si phases of interest. (a) The cubic diamond phase: a face-centered cubic structure with a basis of [(0,0,0),($\frac{1}{4}$,$\frac{1}{4}$,$\frac{1}{4}$)]. (b) The β phase: a highly strained tetragonal structure, with the same relative atom positions as cd, but different lattice dimensions. We use values of $a = 5.431\,\text{Å}$, $b = 6.897\,\text{Å}$ and $c = 2.548\,\text{Å}$, found by minimising the energy of the unit cell in MD, while holding the cell at zero external pressure.

3.1 Introducing the two phases of interest

The two phases that we concentrate on in this chapter are the cubic diamond (cd) and β-Sn phases of silicon, shown in figure 3.1. In static work, the β-Sn phase is observed when silicon is hydrostatically compressed beyond 11.7 GPa [92]. In previous studies using molecular dynamics, uniaxial shock-compression of cd silicon creates a mixed-phase region consisting of cd permeated with thin bands of Imma, a phase closely related to β-Sn [93].

Traditionally, static work on cubic diamond structures usually considers them as fcc-with-a-basis. However, for work on the higher pressure phases of silicon it is useful to consider the cd structure as a body-centred tetragonal structure, by choosing a conventional unit cell rotated by 45° about one of the conventional lattice vectors, as shown in figure 3.2. This results in a 4-atom body-centred conventional unit cell. With this choice of unit cell, it is possible to express the first four phases of silicon (with increasing pressure: cd, β-Sn, Imma and simple hexagonal) by only changing the cell dimensions, a, b, c, and the parameter Δ, which adjusts the relative height of the basis atoms in the unit cell. Therein lies the benefit of this initially counterintuitive

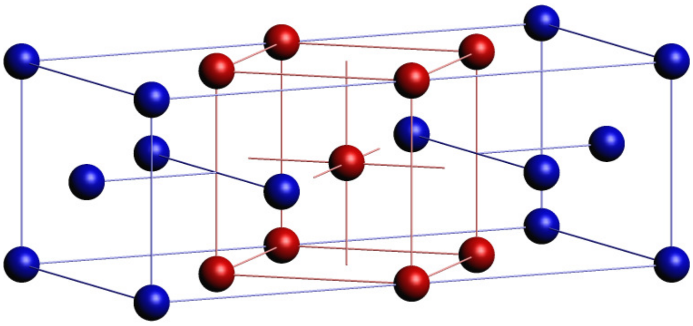

Figure 3.2: Two neighbouring face-centred conventional unit cells, showing the alternative body-centred conventional unit cell coloured red.

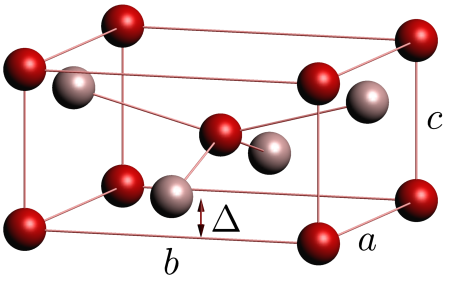

Figure 3.3: The body-centred conventional unit cell for β-Sn. The additional atoms in the 2-atom basis are shown in pale red. For β-Sn $a = b$ and $\Delta = 0.25$, for Imma $a \neq b$ and $\Delta =$ free, and for simple hexagonal $b/c = \sqrt{3}$ and $\Delta = 0.5$.

choice of body-centred unit cell for ambient silicon. We use this choice of conventional unit cell for all further work in this thesis. The body-centred unit cell for β-Sn is shown in figure 3.3.

Now that we are considering both the cd and β-Sn phases as tetragonal structures, they will have the same symmetries when considering their respective stress-strain relationships. The compliance tensor, introduced generally in chapter 2, is given below for tetragonal structures.

$$\bar{s}_{\text{tetragonal}} = \begin{pmatrix} s_{11} & s_{12} & s_{13} & 0 & 0 & 0 \\ s_{12} & s_{11} & s_{13} & 0 & 0 & 0 \\ s_{13} & s_{13} & s_{33} & 0 & 0 & 0 \\ 0 & 0 & 0 & s_{44} & 0 & 0 \\ 0 & 0 & 0 & 0 & s_{44} & 0 \\ 0 & 0 & 0 & 0 & 0 & s_{66} \end{pmatrix}. \tag{3.1}$$

We can see that it contains 6 independent elastic coefficients. However, as the code that we are introducing here is a 1-dimensional code, all shear stresses and strains, *e.g.* σ_{xy}, are assumed to be zero. These elements correspond to Voigt indices of 4-6. Therefore the only pertinent compliance coefficients are those with indices 1-3. We can also relabel $\sigma_{zz} = \sigma_n$ and $\sigma_{xx} = \sigma_{yy} = \sigma_t$, where n and t denote stresses normal to and transverse to the shock direction respectively. We relabel the strains in a similar manner. With these factors in mind, we can reduce the stress-strain relationships considerably:

$$\Delta\epsilon_n = s_{33}\Delta\sigma_n + 2s_{13}\Delta\sigma_t, \tag{3.2}$$

$$\Delta\epsilon_t = s_{13}\Delta\sigma_n + s_{1112}\Delta\sigma_t, \tag{3.3}$$

where we have relabeled $(s_{11} + s_{12}) = s_{1112}$ to make clear that the relations require only three independent quantities. The compliance coefficients are related to the stiffnesses, c_{ij}, by

$$s_{33} = \frac{c_{1112}}{\bar{c}}, \qquad s_{13} = -\frac{c_{13}}{\bar{c}}, \qquad s_{1112} = \frac{c_{33}}{\bar{c}}, \tag{3.4}$$

where $\bar{c} = c_{1112}c_{33} - 2c_{13}^2$.

3.2 The elastic code

The code we have developed is based on the method used by Horie [82]. We begin with the one dimensional Lagrangian wave equations

$$\rho_0 \left(\frac{\partial u}{\partial t}\right) + \left(\frac{\partial \sigma_n}{\partial z}\right) = 0, \tag{3.5}$$

$$\left(\frac{\partial u}{\partial z}\right) + e^{-\epsilon_n} \left(\frac{\partial \epsilon_n}{\partial t}\right) = 0, \tag{3.6}$$

where we use the following

ρ_0	initial density
u	particle velocity
σ_n	stress in the normal direction
z	Lagrangian coordinates in the normal direction
ϵ_n	true strain in the normal direction

We note that we have had to include the additional term $e^{-\epsilon_n}$ in equation 3.6 compared with the original reference as we use true, rather than engineering, strain.

In addition to these equations we require an equation that relates stress to strain. For simplicity with begin with a completely uniaxial, elastic response. The stress-strain relationship in this case is simply

$$\Delta\sigma_n = c_{33}\Delta\epsilon_n, \tag{3.7}$$

as given by equation 2.23. In the full simulations, once the phase change is introduced, we instead use equations 3.2 and 3.3.

Following the method introduced by Horie, in order to integrate these equations in time two sets of meshes are introduced. The two sets are separated by $(\Delta z/2, \Delta t/2)$, where Δz and Δt are the spatial and temporal resolution of the simulation, respectively. In the following superscripts denote the time-step, while subscripts denote the spatial cell, and we omit the previous subscript, n, denoting the normal direction for clarity.

(I)

$$\epsilon_j^{n+1} = \epsilon_j^n - e^{\epsilon}\left(\frac{\Delta t}{\Delta z}\right)\left(u_{j+1/2} - u_{j-1/2}\right)^{n+1/2}, \tag{3.8}$$

$$u_j^{n+1} = u_j^n - \frac{1}{\rho_0}\left(\frac{\Delta t}{\Delta z}\right)\left(\sigma_{j+1/2} - \sigma_{j-1/2}\right)^{n+1/2}, \tag{3.9}$$

$$\sigma_j^{n+1} = \sigma_j^n + \rho_0\langle C_L^2\rangle\left(\epsilon_j^{n+1} - \epsilon_j^n\right). \tag{3.10}$$

(II)

$$\epsilon_{j-1/2}^{n+1/2} = \epsilon_{j-1/2}^{n-1/2} - e^{\epsilon}\left(\frac{\Delta t}{\Delta z}\right)\left(u_j - u_{j-1}\right)^n, \tag{3.11}$$

$$u_{j-1/2}^{n+1/2} = u_{j-1/2}^{n-1/2} - \frac{1}{\rho_0}\left(\frac{\Delta t}{\Delta z}\right)\left(\sigma_j - \sigma_{j-1}\right)^n, \tag{3.12}$$

$$\sigma_{j-1/2}^{n+1/2} = \sigma_{j-1/2}^{n-1/2} + \rho_0\langle C_L^2\rangle\left(\epsilon_{j-1/2}^{n+1/2} - \epsilon_{j-1/2}^{n-1/2}\right). \tag{3.13}$$

Here the angled brackets indicate the average of a variable between time-steps $n+1$ and n, and $\rho_0\langle C_L^2\rangle = c_{33}$. From the second set of equations we find

$$\left(u_{j+1/2} - u_{j-1/2}\right)^{n+1/2} = \left(u_{j+1/2} - u_{j-1/2}\right)^{n-1/2} - \frac{R}{\rho_0}\left(\sigma_{j+1} - 2\sigma_j + \sigma_{j-1}\right)^n, \tag{3.14}$$

where $R = \Delta t/\Delta x$. This equation can then be used recursively to produce

$$\left(u_{j+1/2} - u_{j-1/2}\right)^{n+1/2} = \left(u_{j+1/2} - u_{j-1/2}\right)^{-1/2} - \frac{R}{\rho_0}\sum_{m=0}^{n}\left(\sigma_{j+1} - 2\sigma_j + \sigma_{j-1}\right)^m. \tag{3.15}$$

For a simulation which initiates with a sample at rest, the first term on the right-hand side is zero. The sum in the second term is known as the *stress integral*, which we write as Σ_σ. From this equation, along with equations 3.8 and 3.10, we find

$$\epsilon_j^{n+1} = \epsilon_j^n + \left(\frac{R^2}{\rho_0}\right)\Sigma_\sigma, \tag{3.16}$$

$$\begin{aligned}\sigma_j^{n+1} &= \sigma_j^n + \langle C_L^2\rangle R^2\ \Sigma_\sigma \\ &= \sigma_j^n + \rho_0\langle C_L^2\rangle\left(\epsilon_j^{n+1} - \epsilon_j^n\right),\end{aligned} \tag{3.17}$$

which no longer contain any terms with half-integer indices, and so can be described by the time-steps and spatial cells in the simulation. Using these equations, given a set of initial conditions and boundary conditions, the stress and strain can be integrated forward in time for all cells in the simulation.

In addition to these equations, we introduce an artificial viscosity term, as described in chapter 2. The form of this term is derived from equation 2.8.1.4 in reference [73], which introduces a pressure-like term, q, that is added consistently to the normal stress in all governing equations. The form of q is given by

$$q = -q_c^2\frac{R^2}{\rho_0}e^{-\epsilon_n}\Sigma_\sigma|\Sigma_\sigma|, \tag{3.18}$$

where q_c is a constant that determines the magnitude of the artificial damping.

The resulting simulations from these equations are both temporally and spatially resolution independent, which is of upmost importance when attempting to bridge the gap between the accessible time and length scales of MD and those of experiments.

An early version of this code was used with a plastic yielding term added to equation 3.7 to excellently reproduce experimental shock data on the plastic yielding of copper [94, 44]. In this thesis, instead of plastic yielding, we introduce the option for the material to undergo a phase change, and the ability for the code to calculate and store the stresses and strains in each phase of the resulting mixed-phase region.

3.2.1 Phase change

We now introduce the concept of a mixed-phase region in the code. Rather than having cells which are entirely one phase, we allow individual cells to have a mixture of the two phases. The fraction of β-Sn in the j^{th} cell is given by the phase fraction $f(j)$, which must be between 0 and 1. As we are here only considering a mixed-phase region consisting of two phases, the fraction of cubic diamond in each cell is therefore given by (1-f). Each phase will have its associated strain and, given f, the total strain of the cell can be calculated. To reduce the number of symbols in the equations, we use the scaled length

$$\lambda_d^p = \frac{l}{l_0} = e^{-\epsilon_d^p}, \tag{3.19}$$

where d denotes the normal (n) or transverse (t) direction, and p denotes the phase, cd or β. We can then write the mixed-phase normal strain as

$$e^{-\epsilon_n^m} \equiv \lambda_n^m = f\lambda_n^\beta + (1-f)\lambda_n^{\mathrm{cd}}. \tag{3.20}$$

This will be the strain used in equation 3.6. This is illustrated in figure 3.4. Similarly the mixed-phase transverse strain in the cell can be given as a weighted sum of the individual phases' transverse strains.

$$\lambda_t^m = 1 = f\lambda_t^\beta + (1-f)\lambda_t^{\mathrm{cd}}, \tag{3.21}$$

where we have included explicitly that the total transverse strain in the cell must be zero, as required by a 1D code, and indeed assumed in the uniaxial experiments which this code was developed to simulate.

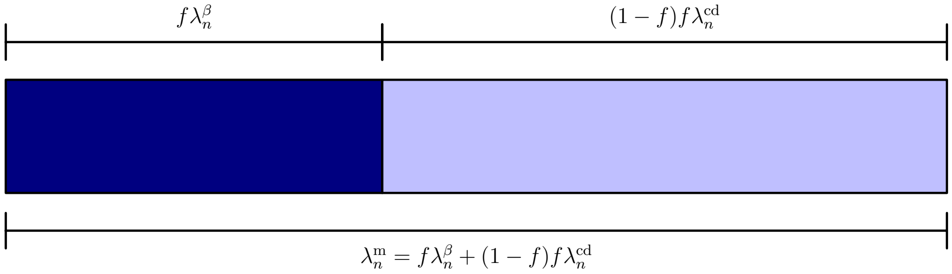

Figure 3.4: The strain in the mixed-phase cells is a weighted sum of the strains of the individual phases.

Taking derivatives of equations 3.20 and 3.21, remembering that

$$\Delta(\lambda) = \Delta(e^{-\epsilon}) = -e^{-\epsilon}\Delta\epsilon = -\lambda\Delta\epsilon, \tag{3.22}$$

yields

$$\lambda_n^m \Delta\epsilon_n^m = f\lambda_n^\beta \Delta\epsilon_n^\beta + (1-f)\lambda_n^{\mathrm{cd}}\Delta\epsilon_n^{\mathrm{cd}} + (\lambda_n^{\mathrm{cd}} - \lambda_n^\beta)\Delta f, \tag{3.23}$$

$$0 = f\lambda_t^\beta \Delta\epsilon_t^\beta + (1-f)\lambda_t^{\mathrm{cd}}\Delta\epsilon_t^{\mathrm{cd}} + (\lambda_t^{\mathrm{cd}} - \lambda_t^\beta)\Delta f. \tag{3.24}$$

The right-hand side of each of these equations is made up of three terms, each with clear meanings. The first term is the fraction of β phase with a given scaled length λ^β (due to existing strain) multiplied by a change in strain $\Delta\epsilon^\beta$. The second term is the analogous term for the cd phase. Finally the third term describes the collapse (or expansion) due to a small fraction, Δf, of the material changing from cd to β, with an associated dimension change $(\lambda^{\mathrm{cd}} - \lambda^\beta)$.

With these equations, along with equations 3.5 and 3.6, and the stress-strain relations for each individual phase, equations 3.2 and 3.3, we need only an equation describing the change in phase fraction, Δf, to form a closed system of equations.

Our assumption is that, once the stress has passed a certain threshold, σ^*, the increasing phase fraction is driven by non-zero shear stress, $(\sigma_n - \sigma_t)$, which gives

$$\Delta f = \begin{cases} \kappa \Delta t(\sigma_n - \sigma_t), & \text{if } \sigma_n > \sigma^* \\ 0, & \text{otherwise} \end{cases} \tag{3.25}$$

where κ is a constant which governs the rate of growth of the phase, and Δt is time-resolution of the simulation. The final assumption concerns the stresses in each phase, which we assume to be in the Reuss limit [95], that is the limit of iso-stress between phases.

Substituting $\Delta\epsilon_n^{\beta,\mathrm{cd}}$ with $\Delta\sigma_{n,t}$ using equations 3.2 and 3.3 gives

$$\begin{aligned} \lambda_n^m \Delta\epsilon_n^m =& f\lambda_n^\beta(s_{33}^\beta \Delta\sigma_n + 2s_{13}^\beta \Delta\sigma_t) + (1-f)\lambda_n^{\mathrm{cd}}(s_{33}^{\mathrm{cd}}\Delta\sigma_n + 2s_{13}^{\mathrm{cd}}\Delta\sigma_t) \\ &+ (\lambda_n^{\mathrm{cd}} - \lambda_n^\beta)\Delta f, \end{aligned} \tag{3.26}$$

$$\begin{aligned} 0 =& f\lambda_t^\beta(s_{13}^\beta \Delta\sigma_n + s_{1112}^\beta \Delta\sigma_t) + (1-f)\lambda_t^{\mathrm{cd}}(s_{13}^{\mathrm{cd}}\Delta\sigma_n + s_{1112}^{\mathrm{cd}}\Delta\sigma_t) \\ &+ (\lambda_t^{\mathrm{cd}} - \lambda_t^\beta)\Delta f. \end{aligned} \tag{3.27}$$

Rearranging equation 3.27 for $\Delta\sigma_t$ gives

$$\Delta\sigma_t = -\frac{\Lambda_{t,13}\Delta\sigma_n + (\lambda_t^{\mathrm{cd}} - \lambda_t^\beta)\Delta f}{\Lambda_{t,1112}}, \tag{3.28}$$

where we introduce the notation

$$\Lambda_{d,ij} = f\lambda_d^\beta s_{ij}^\beta + (1-f)\lambda_d^{\mathrm{cd}} s_{ij}^{\mathrm{cd}},$$

with $d = n, t$ and $ij = 13, 33, 1112$. This allows equation 3.26 to be rearranged to

$$\lambda_n^m \Delta\epsilon_n^m = A + B\Delta\sigma_n + (\lambda_n^{\mathrm{cd}} - \lambda_n^\beta)\Delta f, \tag{3.29}$$

with

$$A = -\frac{2\Lambda_{n,13}(\lambda_t^{\mathrm{cd}} - \lambda_t^{\beta})\Delta f}{\Lambda_{t,1112}},$$

$$B = \Lambda_{n,33} - \frac{2\Lambda_{t,13}\Lambda_{n,13}}{\Lambda_{t,1112}}.$$

This gives

$$\Delta\sigma_n = \frac{\lambda_n^m \Delta\epsilon_n^m - (\lambda_n^{\mathrm{cd}} - \lambda_n^{\beta})\Delta f - A}{B}. \tag{3.30}$$

When there is no phase fraction, equations 3.28 and 3.30 should reduce to equations 3.2 and 3.3. In this special case, $f = 0, \Delta f = 0, \epsilon_t^{\mathrm{cd}} = 0$, and $m \to \mathrm{cd}$ and is omitted for clarity

$$\begin{aligned}
\Lambda_{n,ij} &\to \lambda_n s_{ij}, \\
\Lambda_{t,ij} &\to \lambda_t s_{ij} = s_{ij}, \\
A &\to 0, \\
B &\to \lambda_n s_{33} - 2\frac{\lambda_n s_{13}^2}{s_{1112}} = \lambda_n \left(s_{33} - 2\frac{s_{13}^2}{s_{1112}} \right),
\end{aligned}$$

giving

$$\Delta\epsilon_n \to \left(s_{33} - 2\frac{s_{13}^2}{s_{1112}} \right) \Delta\sigma_n = s_{33}\Delta\sigma_n + 2s_{13}\Delta\sigma_t,$$

as expected from equation 3.2.

This gives us a self consistent set of equations that, given initial and boundary conditions, define the stress and strain in each individual phase, and the total strain in the sample, for all later times. We note that with the phase change mediated as above, the simulations are intrinsically temporally and spatially resolution independent.

3.2.2 The integration routine

Given the imposed boundary condition $\sigma_n(z = 0, t)$, an integration step at timestep $t = l$ proceeds as follows for each cell: if there is any shear stress in the cell, the phase fraction is adjusted to relieve this stress using equation 3.25; the change in longitudinal strain is then calculated following the arguments laid out above; the changes in normal and transverse stress are calculated using equations 3.30 and 3.28; and finally the changes to the individual phases' strains are adjusted using equations 3.2 and 3.3. We show here an algorithmic representation of one simulation timestep:

for $j \leftarrow 1$ to N-1:

$$
\begin{aligned}
\Delta f &\leftarrow \kappa \Delta t (\sigma_n - \sigma_t), \\
\Delta \epsilon^m_{n,j}(t = l) &\leftarrow \frac{R^2}{\rho_0} \sum_{k=0}^{l} (\sigma^k_{n,j+1} - 2\sigma^k_{n,j} + \sigma^k_{n,j-1}), \\
\Delta \sigma_n &\leftarrow \frac{\lambda^m_n \Delta \epsilon^m_n - (\lambda^{\mathrm{cd}}_n - \lambda^\beta_n)\Delta f - A}{B}, \\
\Delta \sigma_t &\leftarrow -\frac{\Lambda_{t,13}\Delta\sigma_n + (\lambda^{\mathrm{cd}}_t - \lambda^\beta_t)\Delta f}{\Lambda_{t,1112}}, \\
\Delta \epsilon^{\mathrm{cd},\beta}_n &\leftarrow S^{\mathrm{cd},\beta}_{33} \Delta\sigma_n + 2S^{\mathrm{cd},\beta}_{13} \Delta\sigma_t, \\
\Delta \epsilon^{\mathrm{cd},\beta}_t &\leftarrow S^{\mathrm{cd},\beta}_{13} \Delta\sigma_n + S^{\mathrm{cd},\beta}_{1112} \Delta\sigma_t,
\end{aligned}
$$

where cell number j is an implicit subscript, and timestep l an implicit superscript, of all variables except where shown explicitly in the second equation. The coefficients $\Lambda_{d,ij}, A, B$ and κ are as before, and $R = \Delta t/\Delta x$ is again the ratio of the temporal and spatial resolutions of the simulation. All parameters are then incremented, *e.g.* $\sigma_n \leftarrow \sigma_n + \Delta\sigma_n$, and the routine repeats for timestep $t = l + 1$.[1]

---

[1] Runtime efficiency is increased by only carrying out the final four steps for cells which undergo a change in that timestep, *i.e.* those that have non zero Δf or Σ_σ.

3.3 Calculating the elastic coefficients from MD

For the stress-strain relationships given by equations 3.2 and 3.3, we must know the elastic constants s_{ij}, which depend on strain. Though these could be extrapolated from the literature, we here choose to calculate them using molecular dynamics. Our choice is determined by the initial desire to compare the new Lagrangian elastic code with molecular dynamics simulations, before extending to experimental time and length scales. We therefore run MD simulations in which we strain small cubic diamond samples and measure the resulting stress tensor. From relating the imposed strain with the resultant stress we can calculate the stiffness tensor, c_{ij}, and therefore the required compliance elements, s_{ij}, using equation 3.4. These same simulations can calculate the strain states of any (meta-)stable phases, which are points in (ϵ_n, ϵ_t)-space where $\sigma_n = \sigma_t = P = 0$. As an illustration, the stiffness coefficient c_{33} is shown in figure 3.5. Also shown are the $\sigma_n = 0$ (green), $\sigma_t = 0$ (red) and $P = 0$ (blue) contours, as well as the hydrostats (white-black dashed) ($\sigma_n = \sigma_t$) passing through the two points that define stable phases. The third intersection of the stress contours in the figure can be shown to be a saddle point [96], and therefore would not give a stable phase.

It is clear from figure 3.5 that there are some discontinuities in the c_{33} landscape, most noticeably in the upper-right of the figure. These are probably due to the inter-atomic potential being parametrised best around the zero strain state. As the portion of the c_{33} surface around the β-Sn phase at zero pressure is smooth, one can extrapolate the surface into the regions where the discontinuities lie, as shown in figure 3.6. In this way it is possible to create a smooth function for the coefficients, if it is believed that the potential is the cause of the discontinuities, and not some underlying physical behaviour. However, as our initial aim here is to compare our new code to MD with identical input data and boundary conditions, we choose to use the original calculated coefficients (fig. 3.5), so a direct comparison can be made.

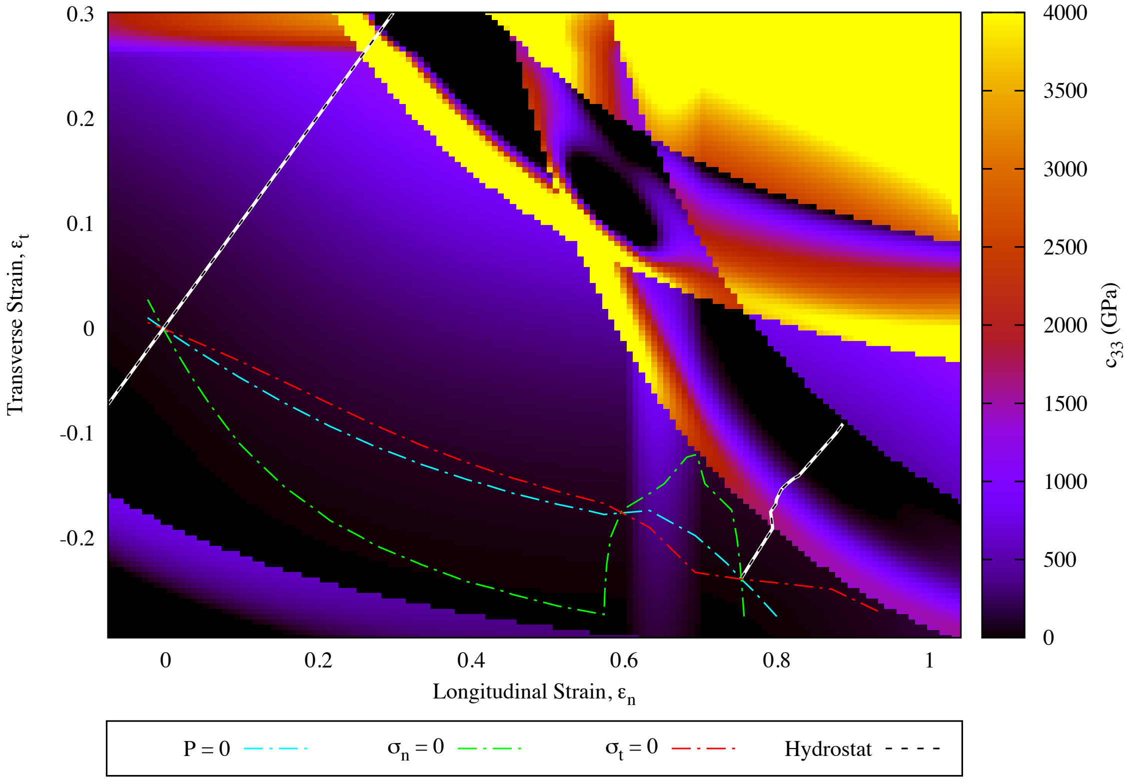

Figure 3.5: The strain dependence of the elastic stiffness constant c_{33}. Also shown are the $\sigma_n = 0$ (green), $\sigma_t = 0$ (red) and $P = 0$ (blue) contours, whose intersections define (meta-)stable points in strain space. The hydrostats ($\sigma_n = \sigma_t$) that pass through the two points that define stable phases are shown (white-black dashed).

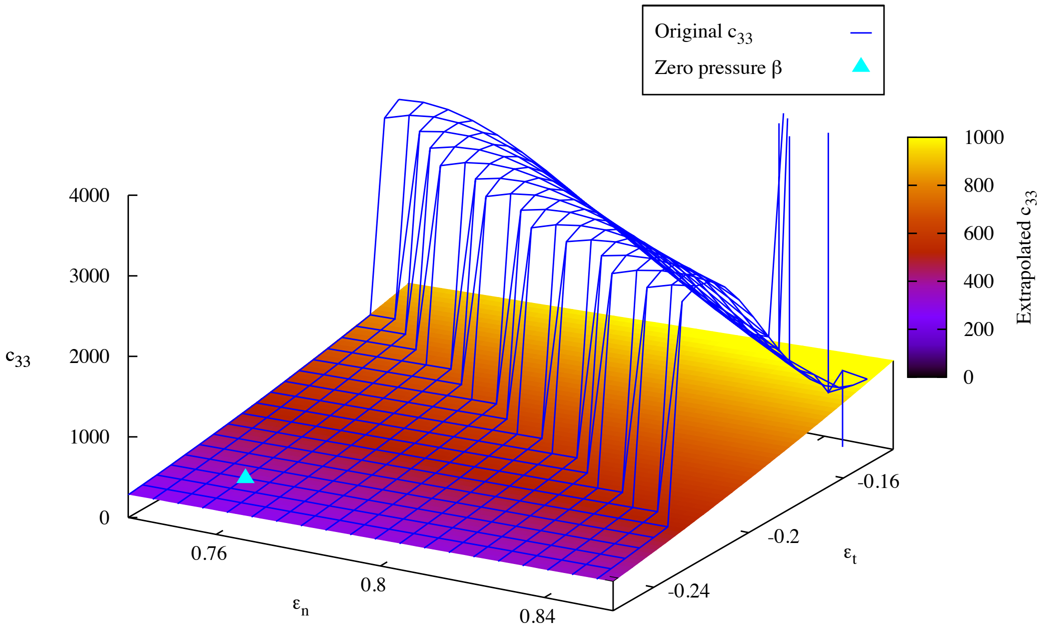

Figure 3.6: Extrapolating c_{33} from the smooth region near zero-pressure β-Sn phase (cyan triangle) to higher strain. The surface is the extrapolated stiffness coefficient. Overlaid (blue) is the original c_{33} coefficient to show exact agreement where the original coefficient was smooth.

3.4 Creation of the new phase

As one of the principal assumptions we hold is that the material is behaving in the Reuss limit, when $f \neq 0$ both phases must experience the same stress. As such, if, upon changing phase, material in a given cell were to follow a path from strain coordinates corresponding to cubic diamond to those corresponding to β-Sn it would have to do so along a strain path that kept both σ_n and σ_t constant. In figure 3.7, we plot for a given timestep, but for all cells, the strain states in the cd and β-Sn phases (magenta and cyan solid lines respectively). We can see that the cubic diamond phase is strained uniaxially (horizontally to the right in the figure) from zero strain before it yields and returns to the hydrostat (black and white dashed line). We can also see from the contours of constant normal and transverse stress that, from the strain state at which the cubic diamond yields (labelled A in the figure), there is no one path to

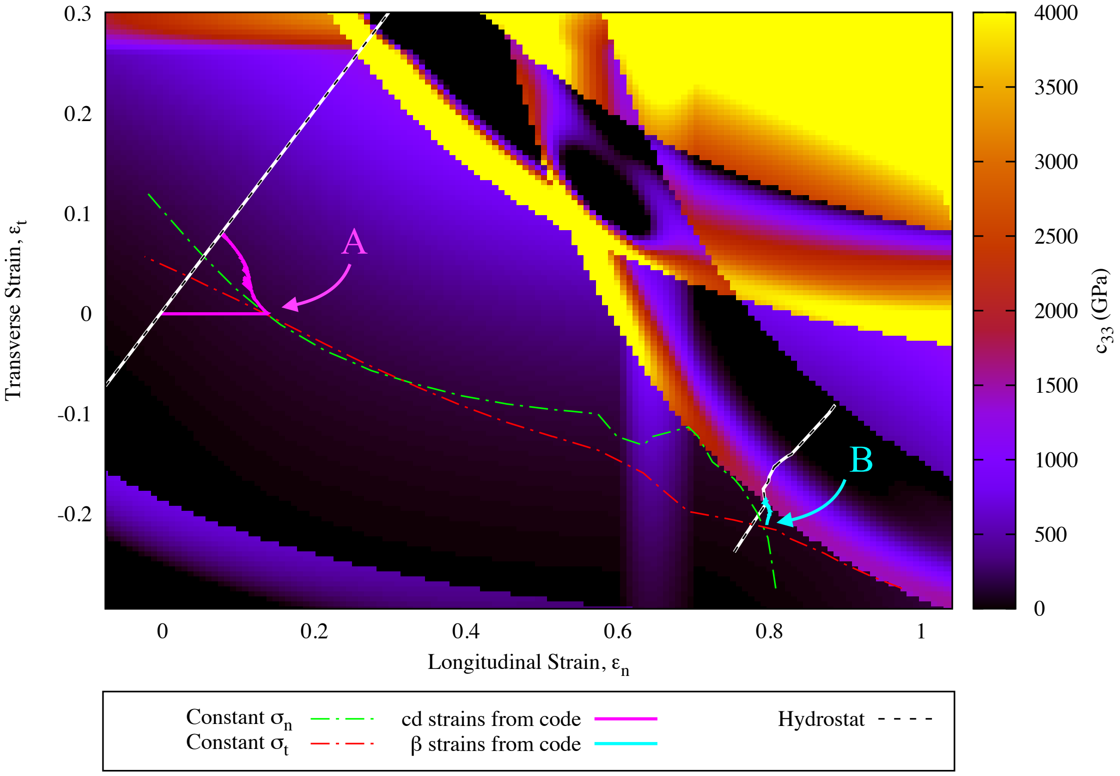

Figure 3.7: This figure shows that there is no path of simultaneously constant σ_n (green) and constant σ_t (red) from the cubic diamond strain (magenta) to the β-Sn strain (cyan).

β-Sn (labelled B) that keeps both stresses constant. Therefore, we are not able to simply permit the phase change and wait for the new β-Sn material to move towards the β-Sn region of strain space (from A to B) of its own accord.

Our solution to this is as follows. As alluded to in section 3.2.2, the strains in the β-Sn phase are updated irrespective whether there is a non-zero phase fraction. In this manner, once the phase fraction is increased (including from 0), the simulation has already calculated the point in strain space that will satisfy the conditions of iso-stress, and creates the new phase at that point. As such, in any one time-step, the material that is undergoing the phase change moves discontinuously between the two points in strain space (from A to B). This is accommodated automatically in the governing equations.

3.5 Initial comparison with MD

A series of molecular dynamics simulations were run using the LAMMPS MD code [86]. The sample consisted of 30x30x400 silicon unit cells (2,881,800 atoms). The interatomic interactions were modelled using a Tersoff-like potential [97], as parameterised by Erhart and Albe [98]. The sample was thermalised at 300 K, before a fixed pressure (as opposed to the frequently used fixed velocity) piston was applied at position $z = 0$.

Given the work by Mogni *et al.* [93], we were expecting the wave profile to consist of a fast-moving elastic precursor followed a slow-moving phase-change wave to take the system to a mixed-phase region containing both the cubic diamond and β-Sn phases.

A plot of potential energy is shown in figure 3.8. As expected, we see a fast-moving elastic precursor followed by a slow-moving phase change wave. Behind this phase change wave a banded, mixed-phase region is seen, as observed by Mogni *et al.* The bands of high (less negative) potential energy atoms are the β-Sn phase.[2] Also visible (yellow) are the atoms that lie along the boundaries between the two phases and are therefore in the most highly strained environments. Finally, the region directly ahead of the piston has lost the banding structure due to the onset of melting in the material.

The aim of our LE code is to be able to accurately recreate the macroscopic properties of the material (pressure, strain *etc.*) as the shock wave travels through it. However, it is troublesome to calculate the strain in the individual phases from the MD, and so we satisfy ourselves with comparing the overall longitudinal strain, as well as longitudinal and transverse stress. We compare the two simulation techniques

---

[2] The specific potential used in the MD does not predict β-Sn to be the stable phase at these pressures, but rather the closely related orthorhombic *Imma* phase. As the difference between these two phases is, for our purposes, small, we continue to use the term β-Sn for the new phase in the MD simulations.

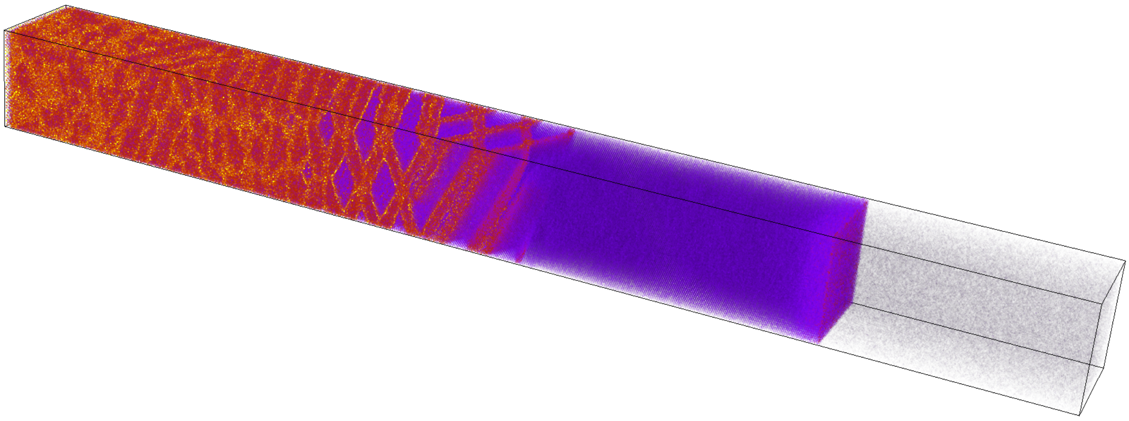

Figure 3.8: Plot of potential energy from MD simulation, shocked from the left by a fixed pressure piston. Clearly visible is the initial elastic shock, following which is the elastically compressed material (purple). The phase change to a mixed-phase region follows this, showing bands of a new phase with higher potential energy (red). The thin boundaries of the bands have the highest potential energy (yellow). Immediately ahead of the piston the material has melted, which removes the clear banding.

for a given timestep in figure 3.9.

Although the elastic precursor velocity in the LE code matches the MD well, the phase change which follows the elastic precursor wave is clearly travelling considerably too quickly. This in turn is allowing the mixed-phase region to accommodate the stress with a smaller longitudinal strain.

There are several possible causes for this behaviour. One possibility is that the new phases are rotated with respect to the original single crystal. It is suggested by Mogni [93] that rotations of $\sim 10^\circ$ in the cd and $\sim 18^\circ$ in the β-Sn are present in the mixed-phase region. Brief analysis of rotating the elastic stiffness and compliance tensors accordingly does not improve agreement with the MD. A full analysis would require a fully 3D LE code, which is beyond the scope of this thesis, but which is currently under construction.

An alternative cause of this behaviour is that we are not acknowledging the boundary layers between the phases in the mixed-phase region. It is quite possible that these behave very differently from the bulk phases, and indeed figure 3.8 shows that they

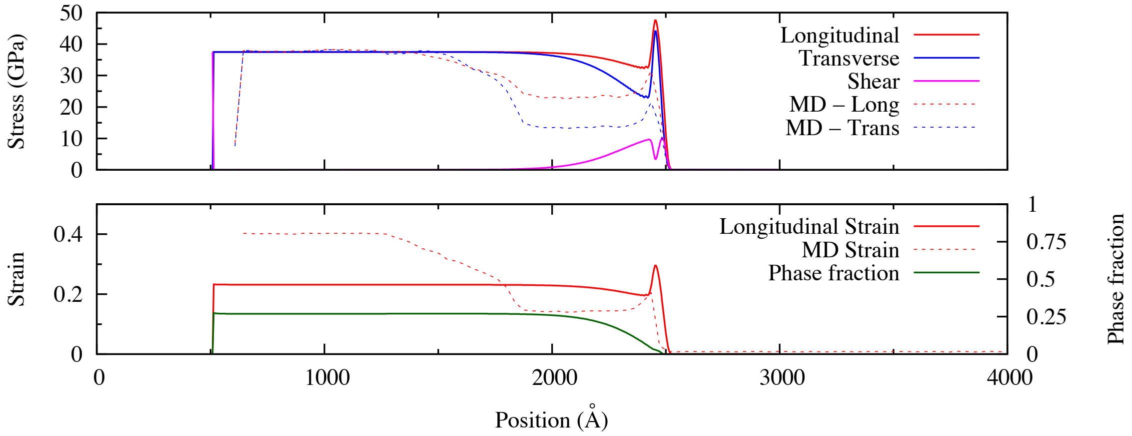

Figure 3.9: Initial comparison of Lagrangian elastic code with MD. The elastic wave speed is well matched but the phase change wave speed is overestimated considerably.

have a higher potential energy than either of the individual phases. This suggests that the boundaries are under significantly different strain conditions to the bulk phases. To investigate this further, we return to our governing equations and introduce a boundary term.

3.6 The boundary softening term

The boundary term should account for softening (or hardening) at the boundaries between the two phases. As such, it appears in the equation governing the total strain of the mixed-phase region, equation 3.20. We introduce a term that is proportional to the current phase fraction, and largest at $f = 0.5$, as that is where we expect there to be the most boundaries between the two phases. A suitable function, which possesses these qualities, is $\chi(f) = \mu \sin^2(\pi f)$, where μ is a constant that defines the magnitude and sense of the boundary term. We include this term in the original equations,

$$e^{-\epsilon_n^m} \equiv \lambda_n^m = f\lambda_n^\beta + (1-f)\lambda_n^{\mathrm{cd}} + \chi(f), \tag{3.31}$$

$$\lambda_t^m = 1 = f\lambda_t^\beta + (1-f)\lambda_t^{\mathrm{cd}} + \chi(f). \tag{3.32}$$

Following the same derivation as before, we arrive at the adjusted stress-strain relationships

$$\Delta\sigma_n = \frac{\lambda_n^m \Delta\epsilon_n^m - (\lambda_n^{\mathrm{cd}} - \lambda_n^\beta - \chi'(f))\Delta f - A}{B}, \tag{3.33}$$

$$\Delta\sigma_t = -\frac{\Lambda_{t,13}\Delta\sigma_n + (\lambda_t^{\mathrm{cd}} - \lambda_t^\beta - \chi'(f))\Delta f}{\Lambda_{t,1112}}, \tag{3.34}$$

where the prime ($'$) signifies the derivative with respect to f, the term B is as before, and A is adjusted to

$$A = -\frac{2\Lambda_{n,13}(\lambda_t^{\mathrm{cd}} - \lambda_t^\beta - \chi'(f))\Delta f}{\Lambda_{t,1112}}.$$

With this small adjustment we can explore the behaviour of boundaries that are harder or softer than the bulk phase. We illustrate this in figure 3.10. The principle is that for a given computational cell, each phase has a single value for each compressibility coefficient, and the additional boundary term must artificially accommodate a different value of these coefficients for the boundaries. If we want to model a boundary that is harder than the bulk phase, *i.e.* less compressible, we require the additional boundary term to artificially occupy volume ($\chi(f) > 0$). This means that in reality the actual phase boundaries would occupy this volume, being less compressible than the bulk.

Conversely, if we believe the boundaries to be more compressible than the bulk, we require the additional term to allow an overlap of the two phases ($\chi(f) < 0$), to emulate the phase boundaries compressing against each other.

We explored both these options, aware that the high potential energy of the atoms in the boundary layers in figure 3.8 suggests that they are more tightly packed than the bulk phases, implying the latter case. Indeed, for positive boundary terms $\chi(f) > 0$, the LE behaviour diverges further from the MD, while for $\chi(f) < 0$ the behaviour

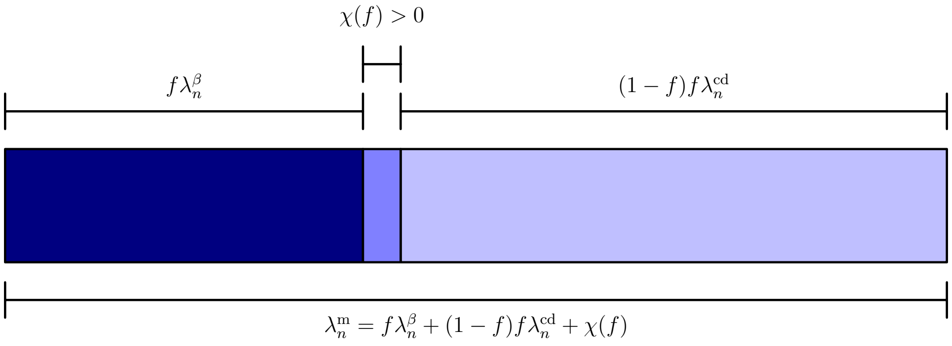

(a) Boundaries harder than the bulk phases: $\chi(f) > 0$

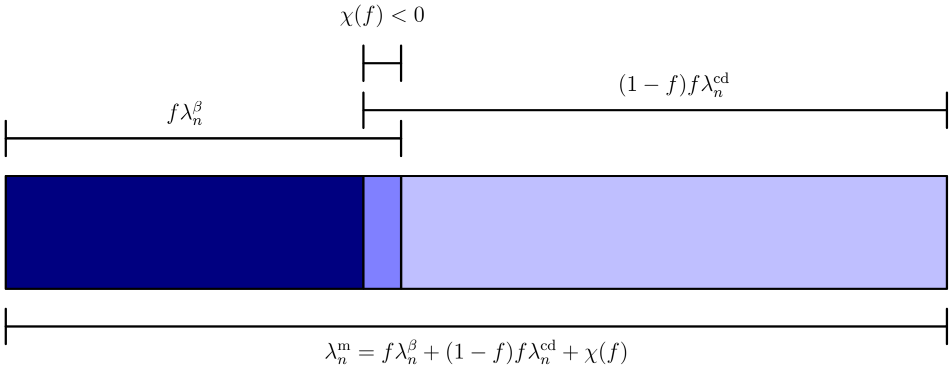

(b) Boundaries softer than the bulk phases: $\chi(f) < 0$

Figure 3.10: Using the boundary term, $\chi(f)$, to allow softer or harder boundaries between the two phases.

converges with the MD, as expected.

With this extra term, we are able to match the stresses and strains from MD for multiple timesteps, and multiple drive pressures, by fitting just three parameters: μ, the magnitude of the boundary softening term; σ^*, the onset pressure for the phase change; and κ, the rate of phase growth (eqn. 3.25). The optimal values for these are found to be $\mu = -0.044$, $\sigma^* = 23.5\,\mathrm{GPa}$ and $\kappa = 8 \times 10^{-3}\,\mathrm{ps}^{-1}\,\mathrm{GPa}^{-1}$.

The effect of each of these parameters on the resulting wave profiles is distinct, and therefore there is a unique solution of the fit. The most obvious effect is that of the phase-change onset pressure, σ^*, which determines the height of the elastic plateau

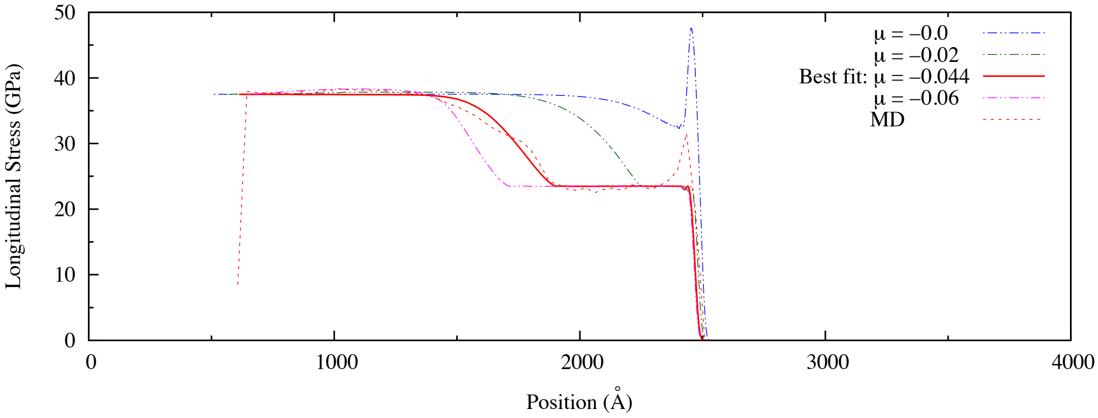

Figure 3.11: The boundary term coefficient, μ, is fitted to match the speed of the phase change wave.

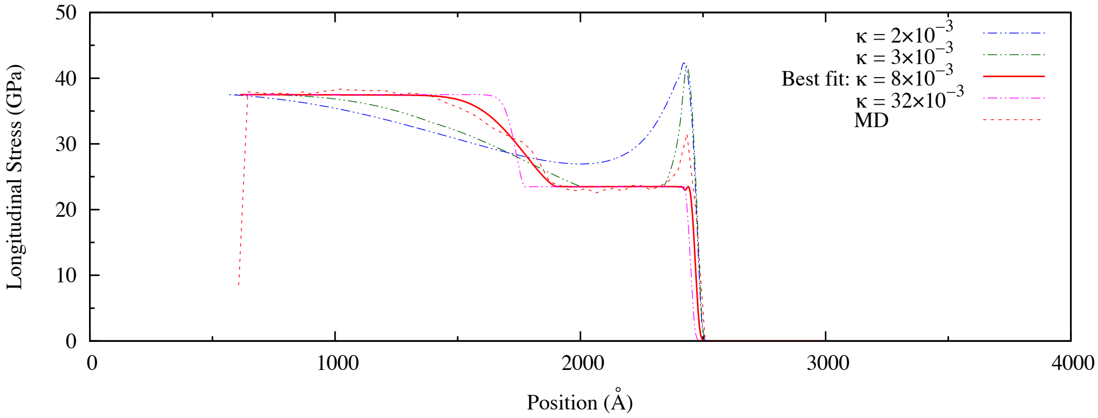

Figure 3.12: The phase fraction growth rate coefficient, κ, is fitted to match the gradient of the phase change wave.

behind the shock front. To demonstrate how the two remaining fitting parameters are independent, we plot parameter sweeps of μ and κ in figures 3.11 and 3.12. In essence, μ controls the velocity of the phase change wave (fig. 3.11), and the resulting total strain of the mixed-phase region. This is in contrast to κ, which controls the slope of the phase change wave, roughly keeping the centre point fixed (fig. 3.12) and has little effect on the resulting total strain.

With this new term, we show the normal and transverse stresses and the normal strain in figure 3.13. We can see that, once the boundaries are accurately accommodated by the model, the agreement with the MD is considerably better.

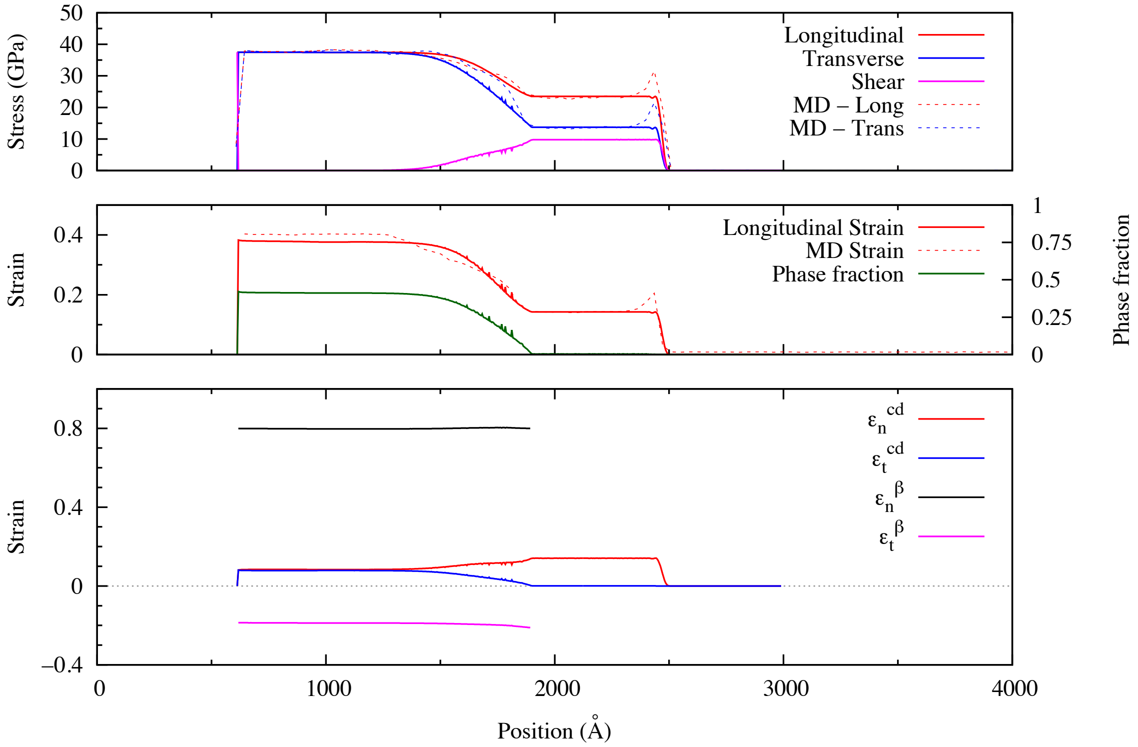

Figure 3.13: Final comparison between LE code and MD. The addition of the boundary term increases the agreement considerably. A slight discrepancy between the final strains is attributed to the melt region in the MD, which is not accounted for with a two-phase version of the LE code. We also show, in the lower plot, the strains in the individual phases, with respect to the ambient cubic diamond lattice parameters.

3.7 Comparing the LE phase fraction with MD

It is possible to compare the phase fraction predicted by the LE code with that measured from the molecular dynamics simulations. Two methods were used to measure the phase fraction from the MD code. The first is the method that was used by Mogni *et al.* [93], where all atoms are binned according to potential energy. This results in a double peaked distribution with a tail at high potential energy. The two peaks correspond to atoms in each of the two bulk phases, while the tail is attributed to atoms in the boundary layer which have the highest potential energy, due to their highly strained environments. A superposition of three separate gaussian peaks is fitted to the profile (one for each of the two main peaks and the boundary tail), and the phase fraction is defined as the number of atoms under the β peak divided by the total number of atoms. The upper limit of the phase fraction assumes all boundary atoms are counted within the β-Sn phase, while the lower limit assumes all boundary atoms are counted within the cubic diamond phase. The phase fraction calculated by this method is shown as the points in figure 3.14. As this method counts the individual atoms, this fraction calculated is a number fraction, signified by f^N.

As an alternative, a less labour-intensive method has been developed. Here, the potential energy values from the MD are first spatially binned into 3-dimensional cells, before being averaged. These averaged values are histogrammed, resulting in a distribution that again has two clear peaks (with a local minimum between them), but a much smaller tail. A simpler assumption is then used to classify the phases of the atoms, that is, all cells above the local minimum are assumed to contain β-phase, whereas all those below are assumed to contain cubic diamond. The phase fraction calculated by this method is shown as the dashed line in figure 3.14. As this method spatially averages the potential energy within each cell before summing, this measures a volume fraction, signified by f^V.

Neither of these measures, number or volume fraction, relate directly to the phase fraction we have defined in the code, f, which is a measure of the phase fraction in each dimension. However, this phase fraction from the code can be related to the measurable quantities from the MD by the following method. First we note that the average unit cell volume, V, is related to the unit cell volumes of the two phases, V^{cd} and V^{β}, the number fraction, f^N, and the ambient unit cell volume, V_0, by the following expression:

$$\frac{V}{V_0} = f^N \frac{V^{\beta}}{V_0} + (1 - f^N) \frac{V^{\mathrm{cd}}}{V_0}. \tag{3.35}$$

By definition of the scaled lengths introduce earlier (eqn. 3.19), we have

$$\frac{V^p}{V_0} = \frac{l_n^p}{l_0} \cdot \frac{l_t^p}{l_0} \cdot \frac{l_t^p}{l_0} = \lambda_n^p (\lambda_t^p)^2, \tag{3.36}$$

for each phase, $p = \beta, \mathrm{cd}, m$. As there is zero total transverse strain (*i.e.* $\lambda_t^m = 1$), the expression on the left-hand-side of equation 3.35 is equal to the normal scaled length, λ_n^m. Replacing the other terms in equation 3.35 with equation 3.36, we find

$$f^N = \frac{\lambda_n^m - \lambda_n^{\mathrm{cd}} (\lambda_t^{\mathrm{cd}})^2}{\lambda_n^\beta (\lambda_t^\beta)^2 - \lambda_n^{\mathrm{cd}} (\lambda_t^{\mathrm{cd}})^2}. \tag{3.37}$$

As noted in the work of Mogni *et al.* [93], the volume fraction, f^V, is related to the number fraction, f^N, by the following expression.

$$f^V = \frac{f^N V^\beta}{f^N V^\beta + (1 - f^N) V^{\mathrm{cd}}}. \tag{3.38}$$

This shows that if the densities of the two phases, and therefore their unit cell volumes, are equal, then the volume fraction and the number fraction are equivalent.

Using the conversion given in equations 3.37 and 3.38, we plot the volume fraction from the LE code, alongside the number and volume fractions calculated from the MD, in figure 3.14. There is good agreement between the LE and MD volume fractions. In the inset of figure 3.14, we show that the number and volume fractions for this LE simulation are very similar, justifying our choice to show both the MD number fraction and MD volume fraction on the same plot.

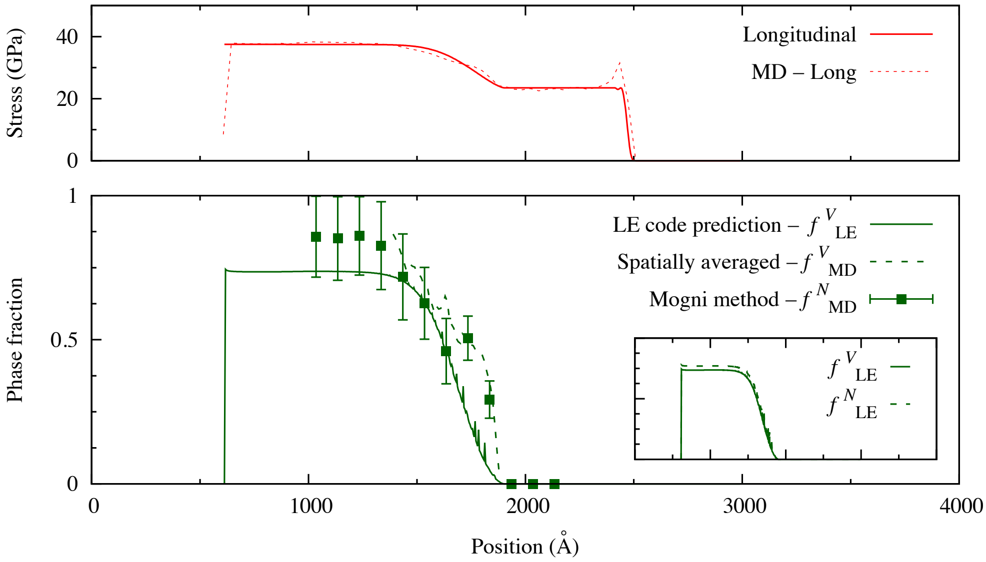

Figure 3.14: Comparing the phase fraction (green) predicted by the LE code to that calculated from MD, for the simulation in figure 3.13. Inset: Comparing the volume fraction and number fraction calculated from the LE code, plotted on the same scales as the full plot. The longitudinal stress profiles are shown again above for context (red).

3.8 Possible additions to the code

There are several additions to the code which would be useful in its current form. Firstly, it is seen in MD that the height of the elastic precursor, here determined by the constant σ^*, decays from the peak piston pressure to its final value over a range of $\lesssim 500\,\text{Å}$. Though this is a small discrepancy here, especially at length scales $\gg 500\,\text{Å}$, a model could be added to take this decay into account when defining σ^*. In experiments on other materials [71, 99], this elastic precursor decay can occur over much longer length scales ($\sim$mm). If the LE code was used to simulate materials with such slow precursor decays, this would clearly become an important addition.

As mentioned previously, the formulation of the code would, in principle, enable an arbitrary number of phases to be simulated. The underlying equations could be rewritten to include a general number phases, rather than specifying exactly two, with a phase fraction, f_p, for each phase. This would allow more complicated material behaviour to be taken into account, including, for example, fully accommodating the melt region shown in figure 3.8.

As the code has been benchmarked against MD simulations, it has been sufficient that the drive is imposed on the sample by a simple stress profile applied to the first computational cell, *i.e.* $\sigma_n(z = 0, t)$. For the drive to be provided by an incident laser beam, for comparison with experiment, would require a laser-material interaction model which is beyond the scope of this work. As an alternative, it is possible to determine the pressure drive created by a given laser pulse using a full radiation-hydrodynamics code, for example HYADES [100]. This pressure drive could then be applied as the boundary conditions to the Lagrangian Elastic code described here.

The code in its current form is used, and further adapted, in the context of a single crystal silicon experiment in the next chapter.

3.9 Summary

We have introduced the formalism behind a new Lagrangian elastic code. The code simulates an elastic material which, when driven by a non-zero shear stress, can undergo a phase-change to create a mixed-phase region. The code calculates and stores the strains in each of the phases therein. The model could in principle be extended to accommodate an arbitrary number of phases. Initially benchmarked against molecular dynamics simulations of shock-compressed single crystal silicon, the code shows good agreement with the stress and strain profiles of the MD. We highlight the necessity for the code to contain a boundary term to accommodate increased density between the crystallites of cubic diamond and β-Sn in the mixed-phase region.

Chapter 4

White-Light X-Ray Laue Diffraction Experiment on the Orion Laser

4.1 Introduction

In this chapter we discuss an experiment carried out using the Orion laser at the Atomic Weapons Establishment (AWE), Aldermaston. The experiment was designed to measure diffraction from the elastic regions of dynamically compressed [001] silicon, on nanosecond timescales. The structure of the chapter is as follows: we describe the previous work in the literature, followed by introducing the Orion system, and the experimental setup. We go on to introduce the data, including an unexpected diffraction feature, and the molecular dynamics simulations we ran to gain insight into this feature. With confidence of the underlying physics, we move on to analysing the data fully before suggesting improvements for future experiments and giving our conclusions.

4.2 Previous work in the literature

4.2.1 Previous experiments on [001] Silicon

Dynamic compression of silicon samples began in the 1960s [101, 102] to further the investigations of the phase changes exhibited under static compression [103, 104]. In the subsequent decades, there has been much debate about the response of silicon to dynamic compression, debate that still continues. When classifying a given technique as either dynamic or static, it is the timescales of the material behaviour that are the deciding factor: if the timescale of the experiment is comparable to the timescale of the material response, it is considered a dynamic compression experiment; whereas experiments with timescales much greater than material timescales are classified as static experiments.

Whereas early work by Pavlovskii [102] suggested that “shock compression does not have any practical effect on the critical phase-transition pressures”, it is now understood that under high-strain-rate compression the material does behave differently to under static compression.

In 1971, Gust and Royce recorded a two wave structure for [001] silicon, consisting of an elastic wave at a stress of 9.2 GPa, followed by a presumed phase-change wave at 14.0 GPa [17].

In 1982, Goto *et al.* found reasonable agreement with this, measuring the HEL at 8.4 GPa, followed by a presumed phase transition at 13.4 GPa [105]. No further transitions were observed up to 60 GPa. The phase change was accompanied by a considerable (22 %) volume collapse.

In 2001, Loveridge-Smith *et al.* showed that for nanosecond scale hohlraum-drive experiments using 40 μm thick targets (as opposed to the ∼mm scale targets used in the previous studies), purely elastic behaviour is possible at least up to 11 % uniaxial compression [25]. It was also noted that for several of the shots, two distinct elastic compressions were observed, though this was attributed to both the sensitive dependence on the temporal profile of the laser beams that irradiated the hohlraum, as well as the slow rise of the radiation temperature in the hohlraum, which created the drive pressure. The work stated that there was no evidence of plasticity or phase-change, and so dubbed this purely elastic response to high peak drive stress as *anomalous.* It should be noted, however, that our elastic code calculates the longitudinal stress of an elastic wave with 11 % strain as 19.2 GPa, much less than the stated maximum drive stress of 60 GPa in Loveridge-Smith's work. This suggests there were processes at work, such as plastic yielding or phase-change, that were not described in the original paper. This will be discussed in more detail later in the chapter.

In 2007, Turneaure and Gupta explored peak stresses between 16.0 GPa and 21.7 GPa and recorded a three-wave profile for long lengthscales (1-3 mm) [106]. The work details a leading elastic wave, followed by a so-called *inelastic* (as opposed to specifically plastic) wave, and finally a phase change wave.

The collaboration returned in 2012, when they showed that peak stresses as low as 12 GPa can result in inelastic behaviour [26], in direct contradiction to Loveridge-Smith's assertion that silicon responded purely elastically up to 60 GPa, and which they did not attribute to the timescales being an order of magnitude larger than in the Loveridge-Smith work. Their explanation for the discrepancy will be discussed in due course.

A detailed paper by Smith *et al.*, from 2012, consolidated results from all the previous works to calculate an elastic precursor stress of 8.7 GPa [18]. However, they also highlighted that at sample thicknesses $< 100\,\mu$m the elastic precursor stress increases with decreasing thickness, up to a factor of 2-3 higher. In addition to this, they found that the precursor initially rose to a peak, before relaxing to a lower stress plateau. Following this plateau the inelastic and phase change waves once more increased the stress up to peak drive stress. Moreover, Smith *et al.* do state that the inelastic wave is consistent with one caused by “the onset of significant plastic flow”.

It is clear, that despite decades of experiments, there is still investigation to be done into the response of even this supposedly simple material to dynamic compression. With a greater number and variety of future experiments, we will be able to more tightly constrain the true behaviour. It is in this context that we planned and carried out our Orion experiment.

4.2.2 Previous white-light Laue diffraction studies

In this experiment, during the compression of the sample, white-light (as opposed to monochromatic) x-rays were used as the “backlighter” to diagnose the crystal structure. Here, this spectrum of x-rays was produced by irradiating a backlighter foil that is a cocktail of several mid-Z elements. This method was first developed by members of the same collaboration as this experiment, and described by Suggit *et al.* in 2010 [107]. The original foils consisted of 300 nm thick layers of Pd, Ag, Sn, Sm, CsI, Ti, and V, coated onto a 10 μm thick layer of plastic film, and, although the foils have undergone several minor adjustments to improve the x-ray yield, have remained largely unchanged. A complete description of the foils, and the x-ray spectra they produce, can be found in reference [107].

Further white-light Laue diffraction studies were completed by the collaboration and reported by Comley *et al.* [108]. The experiment introduced the broadband x-ray diffraction (BBXRD) diagnostic. This diagnostic is a hollow, truncated square-based pyramid, which is lined inside on the four non-square sides with image plate (as seen in figure 4.1). On one square side, there is an opening into which the sample is attached, with the drive surface facing out of the diagnostic. The other square side contains a circular hole to allow a VISAR laser [20] to reflect from the rear surface of the target. However, the experiment used a different method to produce the x-rays, by imploding a spherical plastic capsule, and was carried out on the 60-beam Omega

Laser at the Laboratory for Laser Energetics (LLE), Rochester, NY.

4.3 The Orion laser system

The Orion Laser, at AWE, Aldermaston, consists of ten long-pulse (LP) beams which are synchronised with two petawatt shot-pulse (SP) beams [109].

Each of the LP beams can deliver 500 J of 351 nm (ultraviolet) light in a nanosecond scale pulse. Pulse lengths of 100 ps to 5 ns duration are possible, in 100 ps increments. The long-pulse profiles can be temporally shaped to a high degree and up to 10 ns delay is available between individual LP beams.

The ten LP beams are arranged in two cones of five beams, with a cone half-angle of 50°. The nominal spot size is 100 μm, although use of phase plates and defocussing can increase this to millimetre scales.

The two SP beams deliver 500 J of 1053 nm (infrared) light in 0.5 ps pulses. The relative timing between the LP and SP beamlines can be adjusted to arbitrarily large values.

4.4 Experimental setup

Our experiment investigated the response of single crystal, [001] oriented, silicon to shock compression. A schematic of the setup for the experiment is shown in figure 4.1. For this experiment, the drive was provided by one of the two long-pulse cones. On request, each of the five beams in the drive cone delivered between 50 - 150 J of 351 nm light, resulting in a total drive energy of between 250 - 750 J. The requested pulse shape was a flat-top, 5 ns square pulse. The beams were defocussed to 5 mm, leading to a laser intensity on target of between $\sim 2.5 - 7.5 \times 10^{11}\,\mathrm{Wcm^{-2}}$. This significant defocussing, coupled with overlapping five separate beams, resulted in a smooth drive intensity across a 3 mm portion of the crystal.

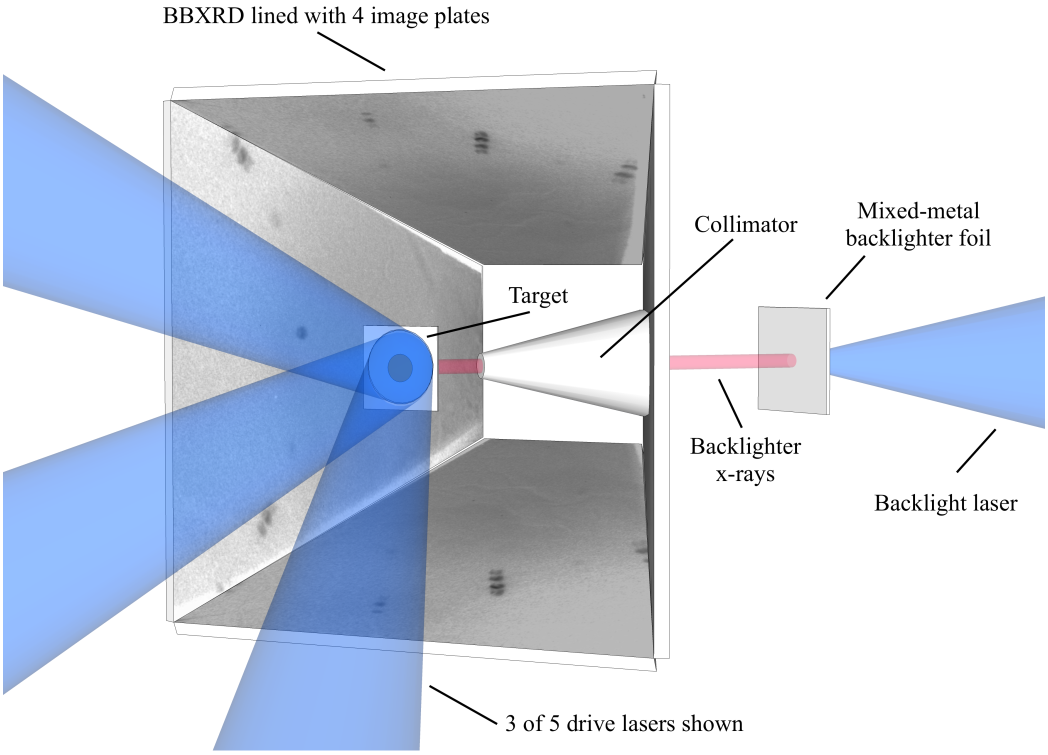

Figure 4.1: Orion experimental setup. Figure is adapted with permission from original publication by Higginbotham *et al.* [23], under license [110].

The targets were made up of 30 μm of single crystal silicon, a 15 μm layer of parylene-N ablator and a flash coating of aluminium. The Si was cut so that the [001] crystallographic direction was aligned with the drive direction.

Our x-rays were produced by using one beam of the opposing LP cone to irradiate a cocktail backlighter foil, of the same type as those introduced in section 4.2 [107, 111]. A 1 ns square pulse delivered $\sim$400 J of 351 nm light, resulting in an intensity of $\sim 10^{14}$ Wcm^{-2} on the backlighter foil. This generated a quasi-continuous x-ray spectrum from 3 - 10 keV. The x-ray spectrum will be discussed in more detail in section 4.9.

Our main diagnostic was an adaptation of the broadband x-ray diffraction (BBXRD) diagnostic introduced in section 4.2 [108]. There are two main differences between our use of this diagnostic and that in the previous reference. Firstly, our target was attached to the larger square side (as seen in figure 4.1), whereas the previous experiments attached the target the smaller square side. Attaching the target to the larger square side allows for a less oblique angle of incidence between the outgoing x-rays and the image plate (IP), resulting in a single diffraction spot being spread over a smaller area of the detector. This allows for a more accurate measurement of the position of the Laue spots on the image plate. Secondly, our setup made use of x-rays that diffracted from the rear surface of the target, as opposed to the drive surface. This meant that the diffraction from this experiment was recorded in reflection, as opposed to the original work which recorded diffraction after transmission through the sample. This enabled us to use lower energy x-rays than in the previous study, which would otherwise have been absorbed on their transit through the sample. Removing the necessity for high energy x-rays ($> 10\,\text{keV}$) avoided having to produce x-rays by imploding a spherical CH capsule [112], as in the previous study. Spherical implosions require high spherical symmetry of the beam positions, and a large number of beams (typically > 30 [112, 108]), and would therefore have been impossible on the Orion system. Another, slightly more subtle, reason for choosing to record diffraction in reflection can be understood by referring to figure 2.9b. It is clear that outgoing k-vectors in the reverse direction sample a much greater volume of reciprocal space than do the forward propagating k-vectors, allowing for more information to be gained from the diffraction pattern.

To reach the rear surface of the target, the x-rays passed through a collimator attached to one non-square side of the BBXRD resulting in a 0.8 mm spot on the rear surface of the sample, which is aligned with the centre of the driven region. As the x-ray spot was substantially smaller than the drive spot, we could be confident that only material subject to the drive pulse was being probed by the x-rays. Moreover, this meant that effects coming from the spatial edge of the drive spot could be ignored, resulting in a uniaxial pressure profile for the entirety of the diffracting material.

4.5 Experimental Results: An introduction to the data

As described in section 4.4, the x-ray diffraction patterns were collected on four trapezium-shaped image plates (IPs). Data from a representative undriven shot is shown in figure 4.2. Although rough positions for each of the IPs were known from the experimental setup, the exact position of each plate was fitted by matching the undriven spots to simulated diffraction spots. Once the position of the four plates was known accurately, additional diffraction spots, which appeared on driven shots, could be investigated.

In figure 4.3 we show data from a driven shot. The same hydrostatic spots are seen as in the undriven case, but during the drive, each diffraction spot splits into four. It should be noted at this stage that, for white light Laue experiments, the position of the spot is only sensitive to the aspect ratio of the unit cell, c/a, and its orientation. Without further information, such as a measurement of the x-ray energy of each diffraction spot, absolute values of strain are not accessible. However, as none of the four diffraction spots show signs of broadening there is strong evidence that the microstructure of the material doesn't change significantly under compression, which would suggest a purely elastic material response, at least in the region of the sample from which these diffraction spots originate. For this reason, we assume that movement of the spot position along the axis of the four spot centres can be measured as uniaxial strain, and that transverse strain in the cell is kept constant, at zero. This assumption is strengthened by the work of Loveridge-Smith *et al.* [25], which observed purely uniaxial compression.

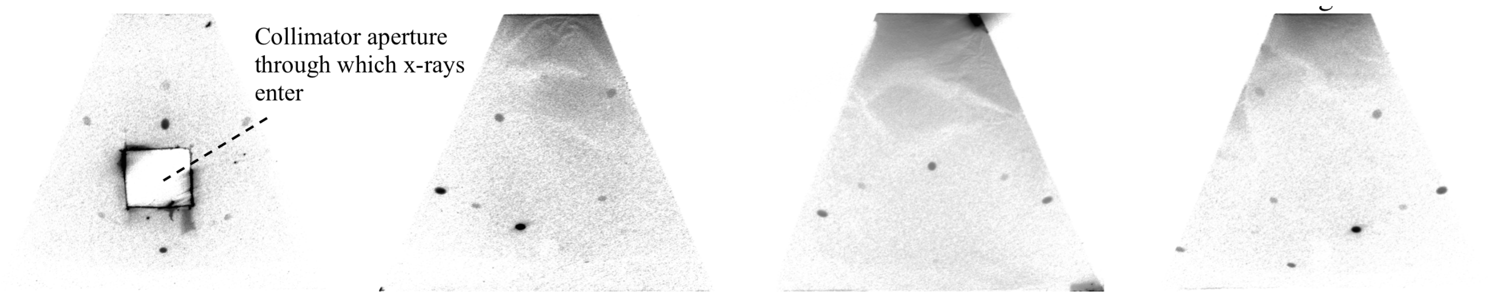

Figure 4.2: Image plate data for a representative undriven (x-ray backlight only) shot. We can see the many Laue spots from ambient cubic diamond.

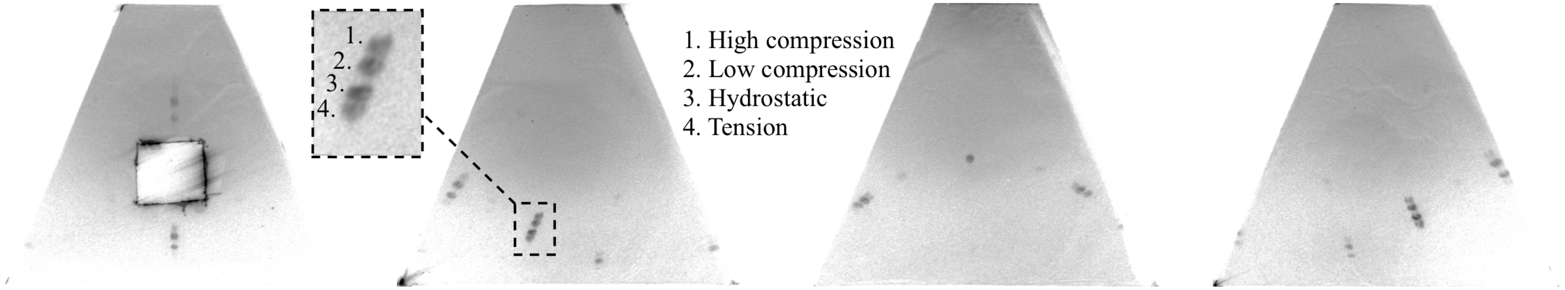

Figure 4.3: Image plate data for a representative driven shot. We can see each Laue spot splits into a four-spot pattern. Highlighted in the inset are the qualitative strains of each of the four spots. The central spot on the third IP is the (004) spot, therefore its position does not change with changes in a_3, *i.e* the magnitude of the lattice vector parallel to the drive direction.

As described in section 4.2, the multiple diffraction spots, indicating multiple strain states in the sample, are not unexpected. However, only two of the additional spots fit diffraction from silicon under *compression*, the final spot appears on the other side of the hydrostatic spot, *i.e.* in *tension*. Although there is evidence of transient tension in previous work [113, 60], this clear, unbroadened tension spot suggests a large region of the sample stays under uniaxial tension for an extended period of time.

The most obvious cause of tension in a sample is that produced when the release wave from the end of the drive pulse reaches the rear surface of the target [113]. There are three main reasons why this can *not* be the cause of the tensile spot seen in the data, which are here discussed in turn, and then illustrated. Firstly, the multiple spots due to positive elastic compression would only be visible if our backlighter was timed to capture the breakout of the leading wave. Our laser drive pulse is 5 ns in duration, while the pulse that creates our backlighter x-rays is only 1 ns in duration. Therefore, when timed to capture the leading edge of the pressure wave interacting with the rear surface, the backlighter will have ceased several nanoseconds prior to the release wave breaking out. Secondly, if the tension arose as described above, in a purely elastic system, the strain value of the tension spot should be the same absolute value as the highest compression spot, but the opposite sign. Even from initial analysis it is clear this is not the case, as the tension spot is much closer to the hydrostatic spot compared with the high compressive strain spot. The reason for the specific value seen (measured as $-4.8 \pm 0.4\,\%$) will be discussed shortly. Finally, the tension spot seen in each group of four is a clear and separate fourth spot, indicating diffraction from a substantial elastic region in tension. This is in contrast to the continuous blur from zero strain that would be created by release at the end of the drive pulse (fig. 4.4 and reference [113]).

To illustrate these points further we can use the Langrangian elastic code described in chapter 3 to simulate a two-wave pressure pulse travelling through the sample.

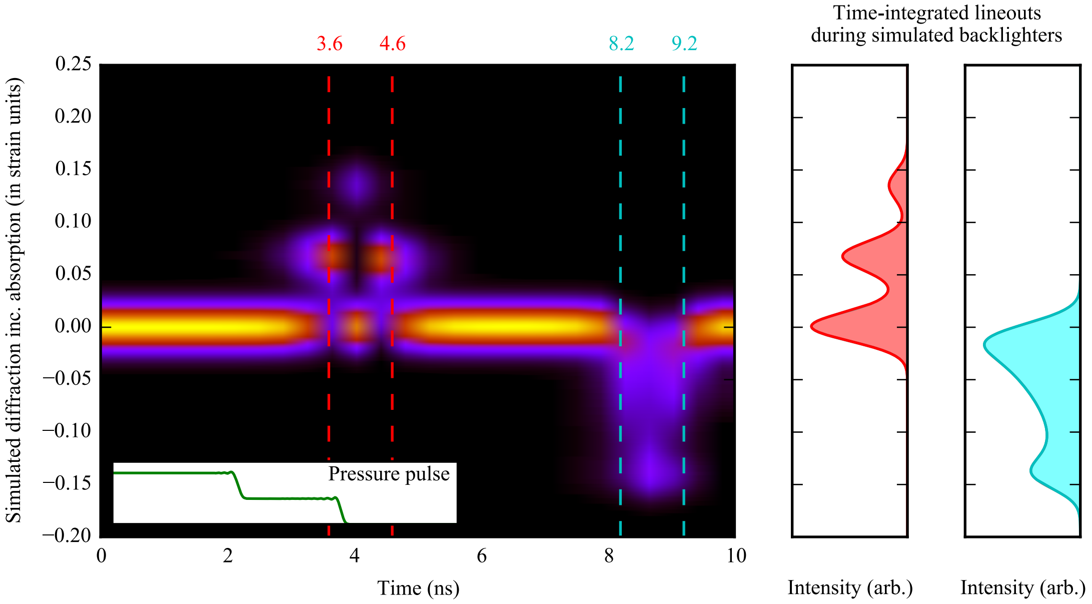

Figure 4.4: Simulated diffraction from a 30 um thick sample exposed to a 5 ns drive pulse. As there is no model in the LE code which would create this two-wave *elastic* profile, we artificially impose a two-wave pressure pulse, shown schematically in the inset (green) for the purposes of simulating the resulting diffraction. Two possible 1 ns backlighter pulses are shown, and the time-integrated diffraction is plotted (red and blue).

From this we can simulate a time-resolved diffraction pattern for one of the diffracting planes and see the appearance (and disappearance) of the additional spots in time. This is shown in figure 4.4. As we can see, the tensile spot appears much later in time than the compression spots, it is of a much larger value of negative strain than those seen in the data (fig. 4.3), and creates a diffuse spot with a less clear separation from the hydrostatic spot.

With these three factors in mind, we are confident that the tensile spot is not due to the release of the drive pressure, but instead due to some interaction between elastic waves in the leading section of the pressure profile and must find a cause that is consistent with the multiple compressive spots. At this stage we introduce a series of molecular dynamics simulations that shed considerable light on the behaviour of the sample during the passage of the pressure wave.

4.6 Molecular dynamics simulations and the appearance of a delay before the cd $\rightarrow$ β-Sn phase change

To complement the MD simulations described in chapter 3, further simulations using the same method were run at pressures closer to the phase change pressure.

These secondary MD simulations revealed a more complicated response to the pressure wave, which manifests at pressures close to the phase change pressure. For a timestep 23 ps after the onset of the pressure pulse, figure 4.5 shows the strain profile, as well as the longitudinal and transverse deformation gradients [114]. These deformation gradients provide a useful metric for quantifying an atom's local environment compared with its previous environment in the undisturbed material. By comparing the relative positions of each atom's neighbours at a given timestep with their initial positions before the onset of the pressure pulse, a local strain tensor for each atom can be calculated. Each element of this tensor provides insight into a certain type of relative movement of the atoms under the passage of the shock. For example, the longitudinal deformation gradient (fig. 4.5 upper colourbar), F_{33}, corresponds to uniaxial compression along the shock direction, and shows two clear regions of compression before the onset of the phase change. Meanwhile the transverse deformation gradient (fig. 4.5 lower colourbar), F_{11}, which corresponds to transverse compression, shows no change from the static material ahead of the mixed-phase region. This is strong evidence that *two distinct elastic* regions exist, ahead of the phase change wave. As shown in figure 4.5, we name the three regions (from right to left) the High Strain Elastic region (HSE), the Low Strain Elastic region (LSE) and the mixed-phase region. The banding seen close to the piston, in both deformation gradients, is again similar to that seen by Mogni *et al.* [93], and is symptomatic of the partial phase change from cd to β-Sn, seen in chapter 3.

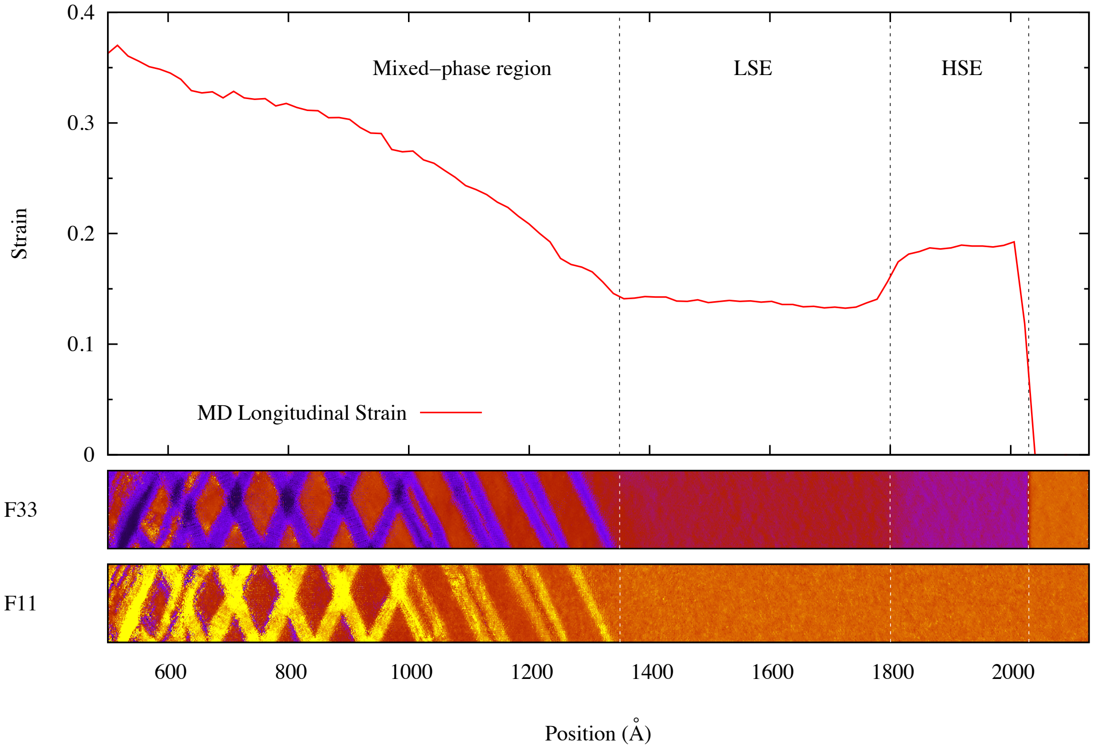

Figure 4.5: Representative strain profile from the secondary set of MD simulations, with the three distinct regions labelled. Also shown are the per-atom deformation gradient elements F33 (upper) and F11 (lower). F33 is related to the compression along the shock direction, whereas F11 is related to compression transverse to the shock direction.

The proposed explanation for the two-plateaux elastic behaviour is described here qualitatively. As the pressure wave travels into the undisturbed material, the phase change to β-Sn is kinetically inhibited. Unable to immediately overcome the enthalpy barrier, no new phase is created, and so only elastically compressed material is present behind the shock, at the value of the HSE. Given that the energy of the phonons in the material will follow a Maxwell-Boltzmann distribution at roughly room temperature (25 meV), only a very small number of phonons will have enough energy to overcome the enthalpy barrier (calculated as 498.65 meV in reference [96]). The phonons strike the enthalpy barrier at a rate proportional to the phonon frequency. After some finite time, a sufficient number of suitably energetic phonons will have overcome the enthalpy barrier to nucleate the phase change, after which the phase change proceeds more rapidly. Precisely how many such phonons are required to cause a cascade of new phase is an ongoing problem. The phase change from cd to β-Sn is accompanied by a large ($\sim$55 %) volume collapse along the shock direction. This collapse allows material directly preceding the phase change wave to relax backwards along the shock direction. This reduces the strain down to the value of the LSE, after which no more new phase can be created. The release wave from this collapse travels forward more rapidly than the phase change wave itself, and erodes the HSE plateau, creating the two plateaux seen in figure 4.5. If the length of the sample was great enough, the HSE plateau would eventually be completely eroded, leaving a two-wave profile; a LSE region followed by a mixed-phase region. In this experiment, our sample is short enough that by the time the leading elastic wave breaks out from the rear surface, the LSE region has not yet fully eroded the HSE region.

4.7 From a two-plateaux elastic profile to four diffraction spots

It is not immediately obvious that this two-plateaux profile can create the four diffraction spots seen in the data, so the process is laid out here. We are reminded that x-ray absorption in the sample means that reflection from material closer to the rear surface appears more strongly in the diffraction pattern.

As described above, the initial profile is a series of four regions, from right to left: the undisturbed material, at $\epsilon = 0$; the high strain elastic region, at a strain ϵ_{HSE}; the low strain elastic region, at a strain ϵ_{LSE}; and finally the mixed phase region.

As the pressure profile moves through the sample, the x-rays initially diffract strongly only from undisturbed material. As the leading elastic wave nears the rear surface, diffraction from the HSE region will begin, followed by diffraction from the LSE region. Once the leading elastic wave reaches the rear surface it will release to $\epsilon = 0$. The release wave travels back into the material, eroding the HSE plateau to zero strain. Once this backward-moving release wave reaches the forward-moving partial release wave (separating ϵ_{HSE} from ϵ_{LSE}), the material is taken into tension at a strain value of $\epsilon_{\text{tension}} = -(\epsilon_{\text{HSE}} - \epsilon_{\text{LSE}})$, from which the x-rays diffract to produce the tension spot. This process is shown in figure 4.6.

Depending on the delay the phase-change experiences, and the thickness of the sample, these four diffraction spots can be produced within a 1 ns backlighter pulse, as shown in figure 4.7. This is in contrast to the tension explored in figure 4.4, which appeared much later in time than the compression spots.

Finally, one can see from figure 4.7 that if the backlighter pulse is not timed precisely with the breakout of the leading elastic wave, not all four diffraction spots will be recorded: too late and the HSE spot will be absent; too early and the tension spot will be absent.

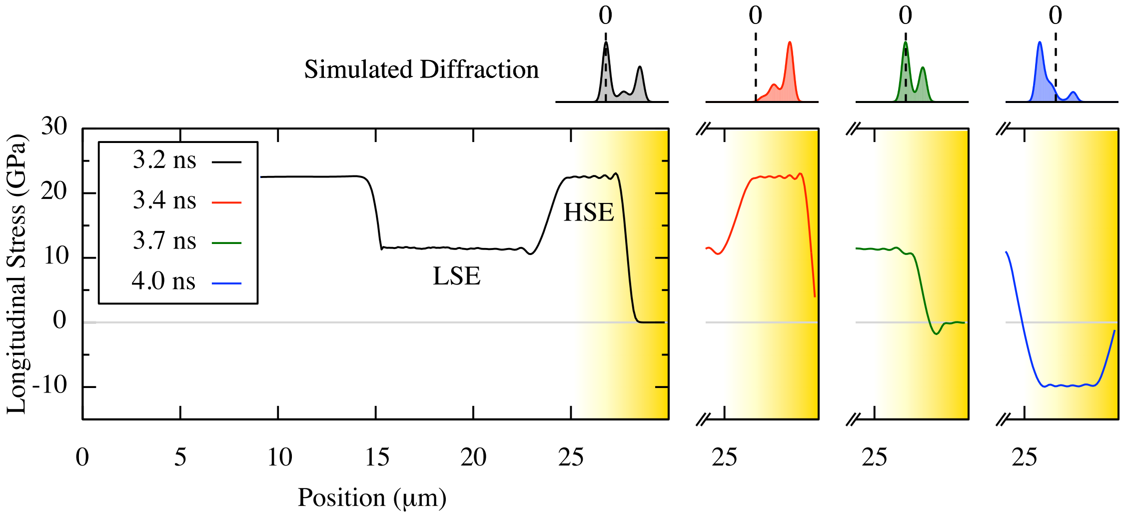

Figure 4.6: A two-wave elastic profile (HSE followed by LSE) causes a 4-spot diffraction pattern on interaction with the rear surface of the sample. Simulated diffraction from the rear surface is shown above. The exponential nature of the x-ray absorption is highlighted with the yellow gradient.

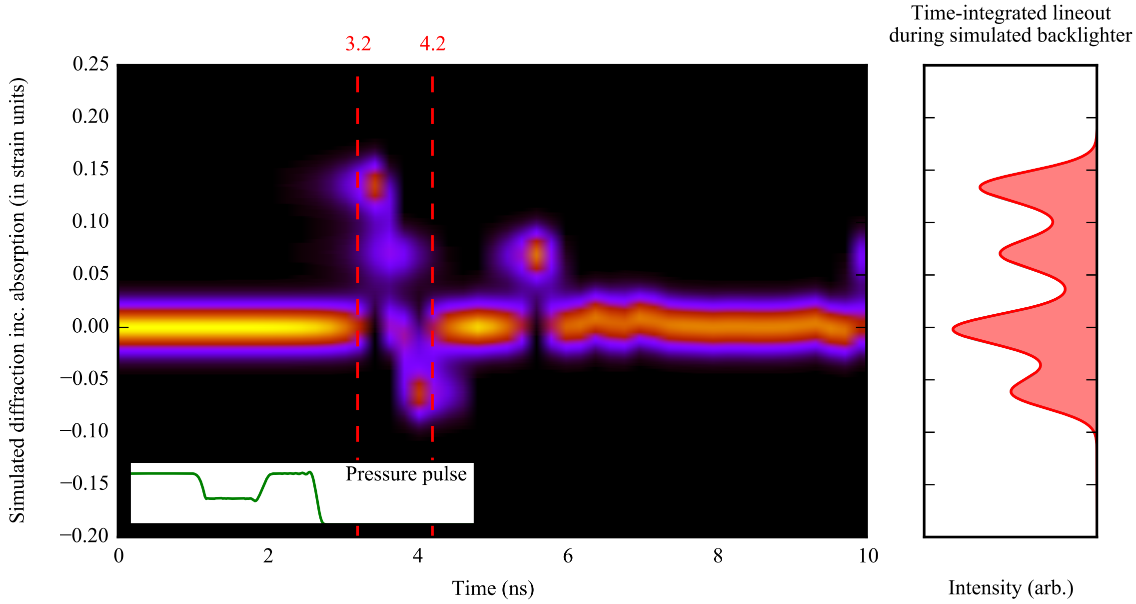

Figure 4.7: A well-timed 1 ns backlighter can record diffraction from all four strain states, resulting in a 4-spot diffraction pattern.

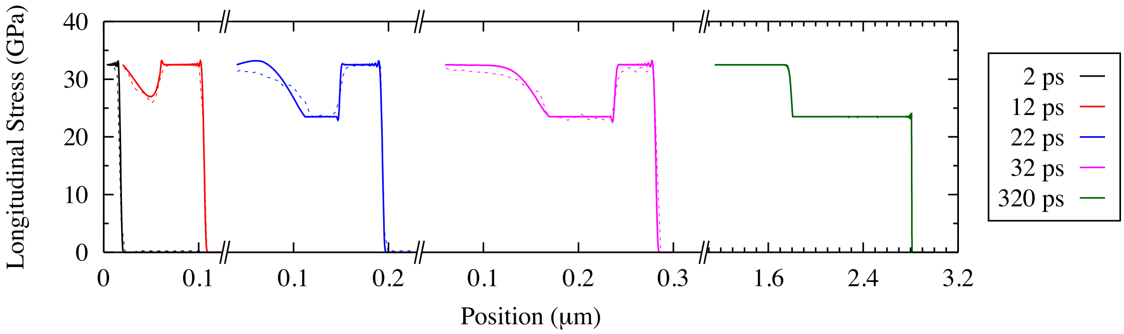

Figure 4.8: The LE code matches profiles from MD for all times of a single simulation. Also shown is a late-time profile (green) from the LE code to illustrate how the LSE region erodes the HSE region completely, leaving a two-wave profile, as seen in gas-gun experiments. MD simulations were not run at this length-scale.

4.8 Implementing the delayed phase-change in the LE code, and simulating the full diffraction pattern

Now that we are confident with the processes occurring in the material, we can adjust our Lagrangian elastic code slightly to accommodate the delayed phase change, and from there simulate the complete diffraction pattern.

Our assumption is that each cell in the simulation, once it has reached the phase-change stress, must wait a time τ_{delay} before increasing its phase fraction of β-Sn. The larger the value of τ_{delay} for a certain simulation, the longer the HSE plateau will be at any given timestep. However, no matter how large the value of τ_{delay}, given enough time, and a long enough sample, the LSE region will always fully erode the HSE region, leaving a simple two-wave structure, *i.e.* an elastic precursor, at strain ϵ_{LSE}, followed by a phase change wave. Comparison between the LE code and MD for multiple timesteps is shown in figure 4.8, including a late time profile showing the HSE region having completely decayed leaving a two-wave profile.

With the LE code accurately reproducing MD simulations, we increase the time-and length-scales of the LE simulations to match the scales of our experiment (using $\tau_{\text{delay}} = 0.6\,\text{ns}$ and $\kappa = 1 \times 10^{-3}\,\text{ps}^{-1}\,\text{GPa}^{-1}$). From these simulations we can calculate the x-ray diffraction pattern at any given timestep, and from there calculate the time-integrated diffraction patterns we expect to record on the image plate. These can then be compared with the data to see if our simulations are consistent with the experiment.

Using the concepts introduced in section 2.2, we simulate diffraction from our LE code. Given a certain crystal plane, defined by $\mathbf{G}_{hkl}$, and the incoming x-ray vector, $\mathbf{k}$, we can calculate the outgoing vector using the Laue condition, $\mathbf{k}' = \mathbf{k} + \mathbf{G}_{hkl}$. Given that we know the position of the image plates from fitting the unstrained spots, we can calculate where this x-ray will intersect the IP. We must also check that the diffraction process is elastic, $|\mathbf{k}'| = |\mathbf{k}|$, and that diffraction from the crystal plane in question is allowed by the selection rules of the crystal, given in section 2.2.3. The diffraction is simulated for the same geometry used in this experiment, and the resulting diffraction patterns are convolved with a gaussian profile to create finite-width diffraction spots from initially infinitely-sharp points. In reality, the spot size is affected by the divergence of the x-rays, dictated by the collimator, and a more complicated convolution could be calculated to model this. For analysis that follows, the gaussian filter used here was deemed sufficient. This simulated diffraction is compared with the IP data in figure 4.9.

As the expected positions of the diffraction spots are now known, this allows certain aspects of the analysis to be simplified. Principally, lineouts from the data can be taken automatically along known axes, namely those axes that pass through the simulated x-ray spots, and should therefore pass through the data spots. We take a rectangular selection of the IP data around a given four spots, and collapse the intensity along a direction perpendicular to increasing strain, to gain a 1D lineout along the strain axis. This is superior to taking a lineout through the spots centres

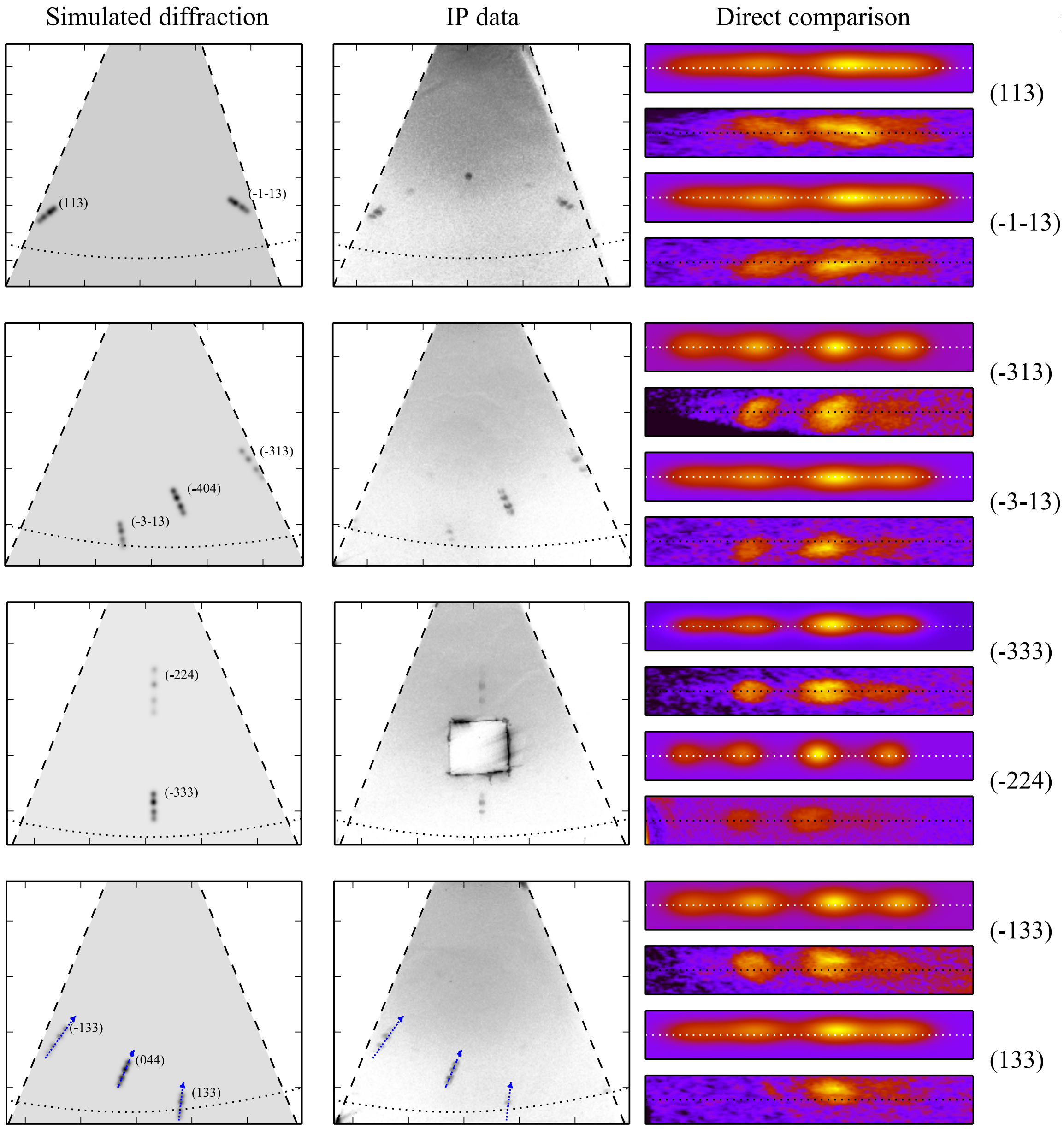

Figure 4.9: Simulated (left) and recorded (centre) diffraction for each of the four plates. We label the diffraction spots on the simulated diffraction (based on an fcc-with-a-basis conventional unit cell). Edges of the IP are shown (dashed lines), as well as a shadow caused by the target mounting plate (dotted lines) which both hinder direct measurement of several of the tension spots. For the bottom plate we show the predicted strain axis, along which the IP data can be automatically measured. Each set of spots is then rotated (right) to enable qualitative comparison (simulated above, data below, for each set of spots), before lineouts are taken for quantitative comparison (fig. 4.10). Note that only data spots that contained useful information were chosen to be simulated, most noticeably the central (004) spot on the upper plate is absent from the simulated pattern.

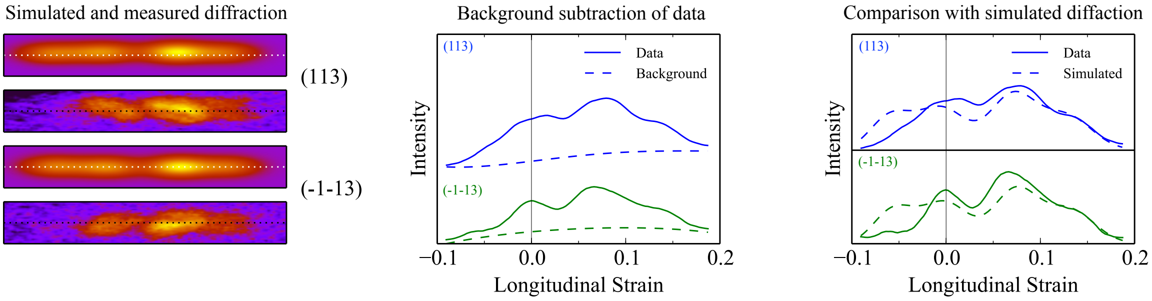

Figure 4.10: For each 4-spot diffraction pattern (fig. 4.9), we sum the total intensity perpendicular to each point on the strain axis. We can then perform background subtraction, before comparing the simulated diffraction.

with a width of only one pixel, as we are not rejecting any of the intensity contained in the 2D spot, but off the central axis. We can then perform a background subtraction routine by averaging intensity either side of the rectangular selection to provide a background intensity. This process is shown in figure 4.10.

At this stage we are in a position to measure the strain values for the three non-hydrostatic diffraction spots. Furthermore, by fitting the strain values of the spots predicted from the LE code to the data, the values for longitudinal and transverse stress can also be calculated. The values will be explored shortly, but first we must highlight an intrinsic limitation of the experiment as it was carried out, and how this affects our analysis of the data.

4.9 The varying intensity of the x-ray spectrum, and its effect on the data

As introduced in section 4.2, our x-rays were produced by irradiating a cocktail backlighter foil. The spectrum that is produced by this method has an intensity that varies considerably with energy. At the time of the experiment, the Orion system had not yet fielded a spectrometer, and so no shot-to-shot x-ray spectra exist. We note that the four spots diffracted from a given crystallographic plane are produced by different energies x-rays, and measure that in our data the energy range required to produce the whole four-spot pattern can be as large as 0.6 keV. This clearly suggests that a spectrum whose intensity varies with x-ray energy will alone greatly affect the relative intensity of the four spots, without considering any other effects. Without a shot-to-shot x-ray spectrum to normalise the intensity of each of the data lineouts, we are not easily able to gain useful information from either the relative or absolute intensity of the spots in a given lineout.

To illustrate the form of the spectrum that is obtained from these cocktail backlighter sources, we reproduce with permission a figure from Suggit *et al.* [107], which shows the spectrum from a similar cocktail foil (fig. 4.11a). We also include a partial spectrum, measured from within a single undriven spot, on a shot with a large-aperture collimator, which shows that there was also considerable intensity variation with x-ray energy present with the backlighter foils used in this experiment.

In essence, this means that we cannot expect a close agreement between the intensities of the lineouts in the right most subplot of figure 4.10.

4.10 Experimental Results: The strains of the elastic plateaux

We are now in a position to measure the strains of the individual spots. As there are diffraction spots from many crystallographic planes on each shot, we are able to take multiple measurements of each of the four strains. We show the measured strains in figure 4.12. For a given shot, we measure the local maxima of the lineouts, remembering that for some shots, the timing of the backlight might mean that fewer than four spots were recorded. The means of these values are plotted as points, along with their standard deviations as error bars. Each experimental shot is plotted with respect to the drive pressure on that shot.

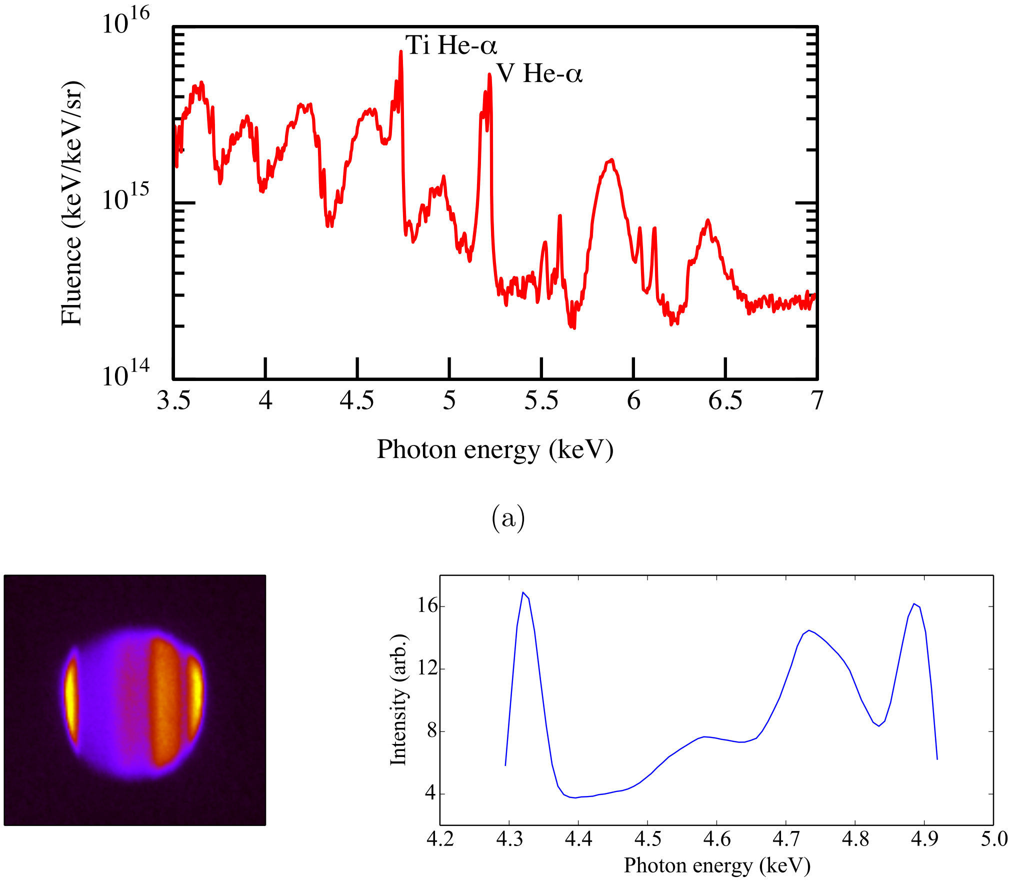

(a)

(b)

(c)

Figure 4.11: (a) Representative x-ray spectrum from mixed-metal backlighter foil, reprinted from [107] with the permission of AIP Publishing, note the vertical log-scale (b) Single undriven diffraction spot, taken from a shot carried out with a large collimator aperture. (c) Partial spectrum taken from (b), the x-ray intensity changes substantially over 0.6 keV, which corresponds to the energy range of a single 4-spot pattern.

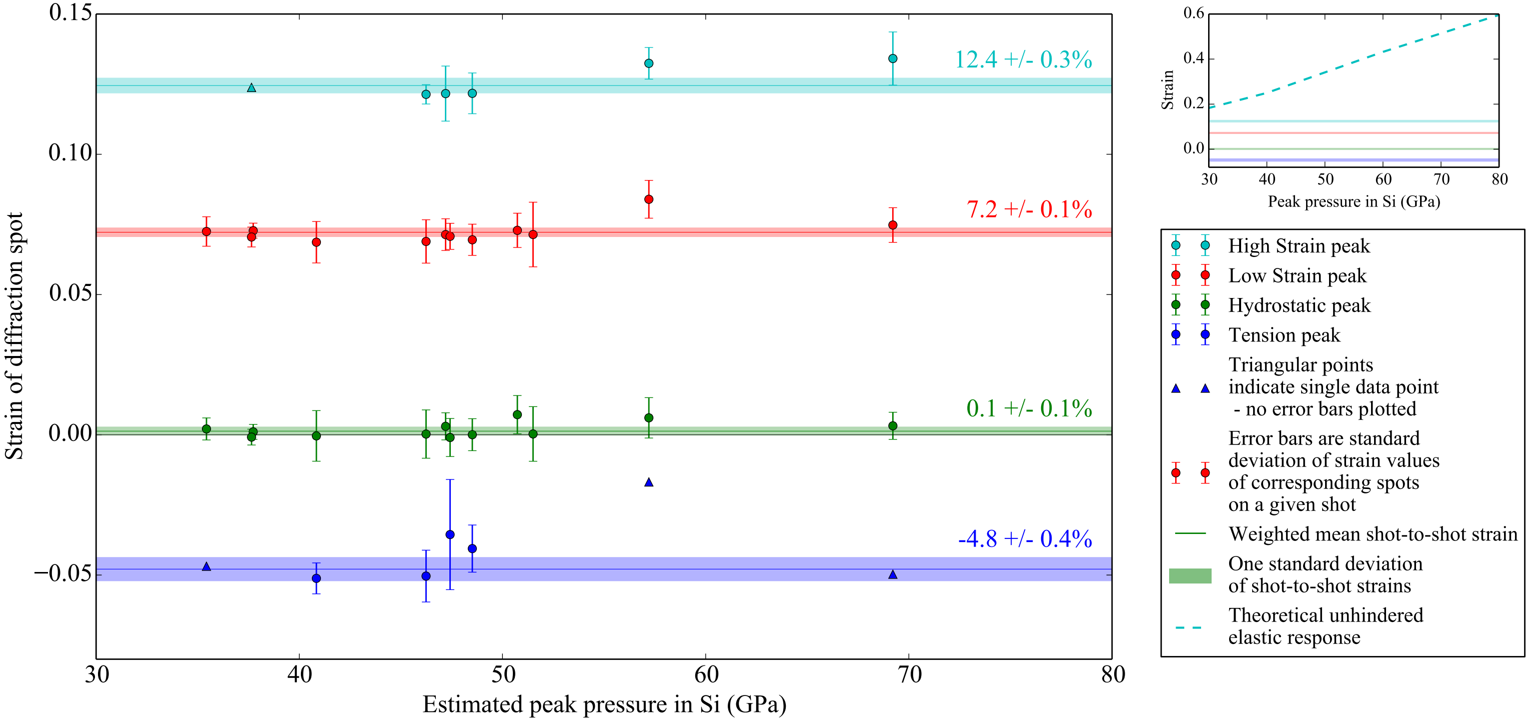

Figure 4.12: Strain values from all Laue spots for each shot. We also illustrate, in the inset, the strain expected calculated from the LE code for a purely elastic response, as posited by Loveridge-Smith *et al.* [25].

As we can see from the figure, the value of strain for each spot does not seem to vary considerably with drive pressure, appearing to be near constant for the full range of drive energies explored (250-750 J, 30-70 GPa).

If we assume that this highlights an underlying insensitivity of the strains to drive pressure then we can calculate the mean and standard deviation of these strains across the full pressure range. These are plotted as the horizontal lines and shading, respectively.

Unfortunately, to convert from drive energy to peak drive pressure is not trivial. As mentioned, apart from the total energy, the drive parameters were kept constant, therefore energy correlates linearly with drive intensity. A scaling law between intensity and pressure, for square pulses, was developed by Mora [115]:

$$P\,(\mathrm{Mbar}) = 11.6\left(\frac{I}{1\times10^{14}\,\mathrm{Wcm^{-2}}}\right)^{3/4}\left(\frac{\lambda}{1\,\mu\mathrm{m}}\right)^{-1/4}\left(\frac{A}{2Z}\right)^{7/16}\left(\frac{Z^*}{3.5}\right)^{-1/8}\left(\frac{\tau}{1\,\mathrm{ns}}\right)^{-1/8}, \tag{4.1}$$

where:

$P =$ Peak drive pressure
$I =$ Drive intensity
$\lambda =$ Laser wavelength
$A =$ Mass number of the ablation material
$Z =$ Atomic number of the ablation material
$Z^* =$ Ionization number of the ablation material
$\tau =$ Pulse length

This scaling, introduced to the author by J. M. Foster of AWE, is shown in figure 4.13. It gives the peak pressure in the ablation material, in our case parylene (CH). From here, the stress in the silicon layer can be calculated by impedance matching, using the equations of state for parylene and silicon as described in section 2.3.4.

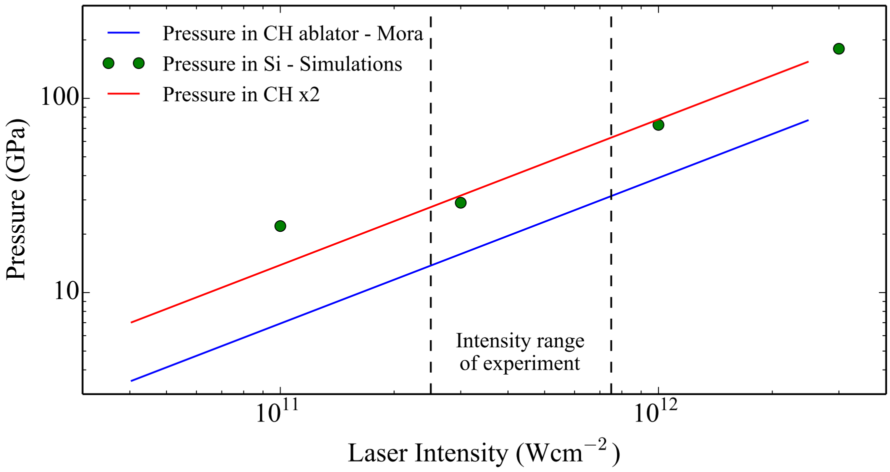

Figure 4.13: Predicted drive pressure in the CH ablator, based on the work by Mora [115] (blue). Simulations carried out by L. Peacock of AWE (green), reproduced with permission. Approximate pressure scaling in Si used by colleagues at AWE is found by applying a factor of 2 to the pressure in the ablator (red), which agrees well with simulations over the intensity range of the experiment.

This analysis suggests the stress in the silicon is roughly a factor of 2 higher than in the parylene. Colleagues from AWE have completed simulations, also shown on figure 4.13, that agree with this analysis for the full range of drive intensities in this experiment. From here we can calculate that the range of intensities in this experiment ($2.5 - 7.5\times10^{11}$ Wcm^{-2}) corresponds to peak drive stresses of 28 - 65 GPa. With this in mind we return to figure 4.12.

The LSE is pegged at a certain value (7.2 ± 0.1 %) irrespective of drive pressure because this is the lowest strain for which it is energetically favourable to change to the new phase. On the other hand, the HSE being pegged at a certain value (12.4 ± 0.3 %) does not have so simple an explanation in the current description: if the HSE plateau is reached before the phase change to β-Sn has chance to take effect, being kinetically inhibited by some energy barrier, then the strain, ϵ_{HSE}, should increase with drive pressure. However, it seems that it is broadly independent of drive pressure. One explanation for this is that a second, rapidly nucleated, but slow moving, phase change begins immediately near the drive surface, and that the HSE plateau is the elastic precursor for this second phase change, and therefore pegged at a certain value. Unfortunately, white-light Laue diffraction in this setup is insensitive to any phase changed material (as described below), and moreover it is insensitive to material far from the rear surface, and so this hypothesis is not immediately testable from the diffraction data.

In this case, we can gain insight from previous work, which shows just such an additional phase change after the cd/β-Sn mixed-phase wave [106, 18], referred to there as the inelastic wave. The final phase is consistent with the simple hexagonal (SH) crystal structure seen in static compression of silicon. Therefore, our proposal is as such: as the material is shock compressed above the SH stress threshold, it undergoes an immediate phase change to SH phase, but with a slow moving phase-change wave that is quickly outrun by an elastic precursor at ϵ_{HSE}. Even at ϵ_{HSE}, a partial phase change to β-Sn is energetically favourable, but a substantial energy barrier inhibits such a change. Eventually, after some nucleation time, the β-Sn phase is nucleated, with the associated volume collapse in the longitudinal direction, sending forward a release wave into the HSE plateau. This release wave erodes the HSE plateau down to ϵ_{LSE}, creating the two-plateaux profile seen in figure 4.5. As the release wave continues forward, eventually it fully erodes the HSE plateau leaving the monotonically increasing profile seen in long length-scale experiments.

This explanation suggests that for each repeated shot at a given drive pressure, two factors could determine the position of the β-Sn phase-transition wave at a given time: the wave velocity and the nucleation time. This is in contrast to both the elastic precursor and the SH phase-transition wave, which are governed purely by their respective wave velocities. However, our data suggest that the nucleation time for the β-Sn phase is on the nanosecond scale, meaning that on long time- and length-scale experiments, the position of the partial phase-change (inelastic) wave at a given time is dominated by the wave velocity, and not the nucleation time. This is consistent with the data from mm-scale targets in reference [106], which shows the β-Sn wave position at a given snapshot to be extremely consistent shot-to-shot.

Extrapolating the trend in SH wave speed (ref. [106]) from 21.7 GPa to slightly higher pressure, the SH phase-change wave would overtake the β-Sn phase-change wave, and a two wave structure would manifest: elastic precursor followed by a phase-change to a SH structure. Indeed, in reference [17], the second phase-change wave is seen to overtake the first below 36.3 GPa.

With this qualitative description being complementary to previous work, we now look at whether it is quantitatively consistent. As described, the value of our low strain elastic plateau should be the traditional HEL. A strain value of $7.2 \pm 0.1\,\%$ from the data coordinates with a longitudinal stress of 11.7 GPa in our LE code. This is considerably higher than the recorded 8.7 GPa elastic precursor stress, however, we remind the reader of the results of Smith *et al.* which display a substantial rise in elastic precursor stress with decreasing target thickness. With targets of thickness 15 - 55 μm, they find elastic precursor stresses of 12.6 - 19.1 GPa, considerably higher than the long length-scale HEL stress. This is because for the thinnest targets, the timescale of the experiment approaches the timescale of the material response to compression, and so only partial relaxation is possible during the passage of the pressure wave, exhibiting an artificially high elastic precursor. As the disturbance traverses more material (by using a thicker target) complete relaxation is possible, reducing the elastic precursor to the long length-scale HEL stress.

Likewise, we can compare our HSE values with previous work. Firstly, the maximum 11.7 % longitudinal strain[1] seen by Loveridge-Smith [25] may indeed be from the same process as our HSE strain, which for us is constant at $12.4 \pm 0.3\,\%$. They maintain that this strain value is limited by their maximum drive pressure of 60 GPa,

---

[1] We have converted the engineering strain stated, $e = 11\,\%$, into true strain, $\epsilon = -\ln(1 - e)$, for direct comparison with our results.

as they see no evidence of either plasticity, or of diffraction from other phases. Given that all other works that explore pressure up to 60 GPa see at least one additional phase being created, and that a 60 GPa drive pulse would create an purely elastic wave with much greater than 11 % strain, we strongly believe that Loveridge-Smith *et al.* were seeing the precursor from a phase change wave. Their statement that no evidence of phase change is visible is explored by Turneaure and Gupta [26], who posit that the new phase is created with some heterogeneity in its microstructure. The combination of the non-focussing x-ray diffraction geometry used by Loveridge-Smith (and indeed in this experiment) and the heterogeneity in the phase-changed material would result in any diffraction signal being diffuse, and so spread over a large area of the detector. This would result in the diffraction from the phase changed material not being visible, compared with the bright signal from the elastically compressed cubic diamond phase. We agree with this explanation, and provide stronger evidence for one or more phase changes following the elastic wave, despite not seeing diffraction signals directly from the new phases.

Separately, Smith *et al.* report a peak in the elastic precursor before a pullback to a lower stress. Although they attribute this to plastic work releasing the precursor to a lower stress, we can compare the values to see whether our two data are consistent, despite our explanations differing. The peak precursor stress they measure as 20.2 ± 1.9 GPa for targets of thickness 15 - 55 μm, in good agreement with our value of 22 GPa.

4.11 Further considerations

Due to the lack of shot-to-shot spectra, we have not analysed the intensity of each of the four peaks in any group. However, it should be mentioned for completeness that the intensity of diffraction from static, undisturbed material and elastically compressed material do not compare completely intuitively. As described in reference [116], under compression, an *increase* in diffraction intensity can be seen. This is attributed to the change from a scheme of dynamical diffraction in the unshocked material to kinematic diffraction in the shocked material, whereby even small strain gradients decrease the regularity of the lattice, and thus can actually increase the diffraction signal. As we lack sufficient information to analyse the intensity of the diffraction signal no more will be said on this at this stage, but we note that such effects have been observed previously by Woolsey [117].

A useful diagnostic to have had on this experiment would have been a Velocity Interferometer System for Any Reflector (VISAR) [20]. A rear surface velocity measurement might have unambiguously revealed the two-plateaux profile, without having to infer it from the existence of the tension spot, as we have here. Unfortunately, the VISAR system was not fully operational on Orion at the time of the experiment (this was the first academic access experiment on the facility), and on the very few shots for which we have rear surface velocity data, only one arm of the VISAR fired, meaning we have no fringe disambiguation, and so no unambiguous measure of the rear surface velocity. As such, these VISAR traces are inconclusive with respect to our description of the two elastic plateaux, nor could they provide a measure of the total drive pressure reached on each shot. This would be an extremely helpful diagnostic to run on any future experiments of this nature.

In addition to this, a direct, time-resolved measurement of one of the diffraction spots would be useful. One could imagine engineering an additional aperture in the BBXRD, such that one of the four-spot diffraction patterns could be recorded by a streak camera. In this way, time-resolved diffraction data, as well as the time-integrated full diffraction pattern on the IP, could be recorded.

Alternatively, as seen in figure 4.3, the (004) diffraction spot remains in the same position on the image plate throughout the drive pulse. This is due to the insensitivity of the (00n) spots to changes in the magnitude of the a_3 lattice parameter, that parallel to the drive direction. The x-rays that created this diffraction spot will have been of multiple different energies, related to the lattice spacing, and therefore the strain state, of the sample region from which each individual photon diffraction. This information is lost by recording the spot using IP. If instead, an aperture in the BBXRD allowed the spot to be recorded using a CCD, judicious choice of filtering would allow the *energies* of the individual x-rays to be recorded, regaining this lost information [118].

4.12 Summary

We have described an experiment carried out on the Orion Laser at AWE, Aldermaston. Single crystal [001] oriented silicon samples were laser-driven while a co-timed x-ray backlighter investigated a uniaxially compressed region of the sample. The diffraction patterns were recorded on image plates, allowing the strain induced movement of Laue spots to be investigated. The diffraction data suggest that the two separate elastic regions precede a phase-change wave, perhaps to the mixed-phase region seen in molecular dynamics. Quantitative analysis of the data suggests these elastic regions exist at strains of 12.4±0.3 % and 7.2±0.1 %, independent of peak drive pressure. This pressure independence also suggests that a second, rapidly nucleated, but slow moving, phase-change wave follows the mixed phase region.

Chapter 5

Single Crystal Monochromatic X-ray Experiment on the LCLS

5.1 Introduction

In this chapter we discuss an experiment carried out using the Linac Coherent Light Source (LCLS) at the Stanford Linear Accelerator Center, in California, USA. The experiment was designed to investigate the response of single crystal silicon to uniaxial compression on nanosecond timescales. As we will see, the extremely bright x-rays produced by the LCLS, compared with those produced by the mixed-metal backlighter foils of chapter 4, made this experiment sensitive to different forms of material response. In this way, the data presented in this chapter complement those of the previous chapter well. The structure of the chapter is as follows: we first give details of the LCLS system, and the experimental setup. We go on to introduce the data, and discuss the presence and benefit of the third harmonic diffraction spots therein. We describe in detail the concept of mosaicity, before measuring the orientation and mosaic spread of the newly-formed crystallites in the sample. We discuss what can be said about the phases that are created, both in compression and release, before summarising the main findings and putting forward possibilities for further work.

5.2 The Linac Coherent Light Source

The LCLS is an x-ray free electron laser (XFEL) [119] that began fielding experiments in 2009 [120, 121]. Before the development of XFELs, so-called 4th-generation light sources, the brightest x-ray sources were synchrotrons [122], known as 3rd-generation light sources. The evolution of XFELs heralded an increase in peak x-ray brightness available to experiments of more than 8 orders of magnitude [121].

At the LCLS, x-ray energies of 0.25 - 9.5 keV (in the fundamental harmonic) are possible, delivered to the experimental chambers at a rate of up to 120 Hz. The experiment in this chapter was carried out at the Matter in Extreme Conditions (MEC) instrument [123], which comprises a cylindrical 2 m diameter vacuum chamber into which are focussed two optical lasers to drive the target before the arrival of the x-rays. The x-rays can be delivered to target with spot sizes between 2 - 150 μm and pulse lengths between 5 - 200 fs. In addition to the fundamental harmonic, the LCLS delivers a small intensity of the third harmonic, which can be rejected by placing harmonic rejection mirrors in the beam.

The optical lasers at the MEC end-station are a two-armed long-pulse Nd:glass system and a short-pulse Ti:sapphire system. The laser used in the experiment described here was the long-pulse laser, which can deliver two co-timed 25 J pulses, with pulse lengths of 2 - 100 ns, at a frequency-doubled wavelength of 527 nm.

5.3 Experimental setup

The experiment described in this chapter, like that of the previous chapter, investigates the response of [001] oriented single crystal silicon to a laser-driven pressure

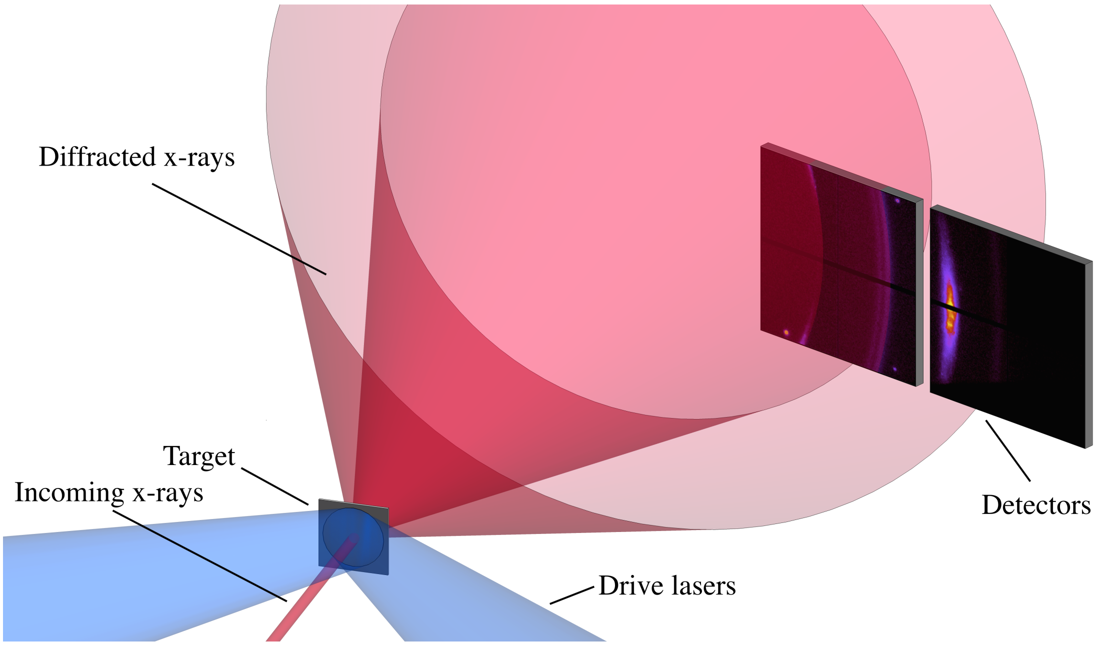

Figure 5.1: Schematic of the setup for this experiment.

pulse. However, the nature of the x-rays used to probe the material, namely the extreme brightness and high monochromaticity, means that the experiment is sensitive to different processes in the sample. A schematic of the setup for the experiment is shown in figure 5.1. For this experiment, the two arms of the long-pulse laser provided a 10 ns pulse, focussed to 200 μm diameter flat-top spot, resulting in an intensity on target of $\sim 10^{12}$ Wcm^{-2}.

The x-rays incident on the target were delivered by the LCLS as quasi-monochromatic ($\Delta E/E = 0.2$-$0.5\,\%$), transversely coherent, 7.952 keV pulses of 60 fs duration. Each pulse contained an average of $\sim 10^{12}$ photons.

The x-ray diffraction signal was recorded in transmission by two Cornell-SLAC Pixel Array Detectors (CSpads) [124], which covered a solid angle between approximately $20^\circ < 2\theta_B < 70^\circ$ and $-25^\circ < \phi < 25^\circ$.

The targets were made up of either 43 μm or 100 μm single crystal, [001] oriented, silicon. Unlike the previous experiment discussed, these targets had no parylene-N layer, with the drive laser directly ablating the silicon.

5.4 Experimental Results: An introduction to the data

To illustrate several important features of the data, we show background subtracted data from three representative shots in figure 5.2. We display it in the same orientation as in figure 5.1: Bragg angle is increasing from left to right; and azimuthal angle, ϕ, is approximately zero at the horizontal centre of the CSpads.

Several features which are present in the entire data set can be introduced. On the left detector two bright spots (labelled 200 and $10\bar{1}$ in red) close to $\phi = 0$ are seen at early time (fig. 5.2a), which appear to increase their ϕ extent after breakout (fig. 5.2b), before having full azimuthal symmetry by the late time shots (fig. 5.2c). The Bragg angle of these two arcs is consistent with several of the high pressure silicon phases, namely β-Sn, Imma and simple hexagonal. In addition to these, at late time, two further arcs extend inwards from the detector edges at low Bragg angle (labelled $10\bar{1}$ in blue). These arcs are consistent with a highly mosaic cubic diamond structure. From the several samples which were mounted with a substantial rotation around their target normal, we can determine the position of the centre of these two arcs, despite the centres lying off the detector for the majority of the shots.

On the right detector, a spot (labelled $1\bar{1}\bar{2}$ in blue) near $\phi = 0$ at early time increases in brightness and appears to increase its ϕ extent once again as backlighter delay is increased. This is consistent with the mosaic cubic diamond structure previously mentioned. In addition to this, an arc is seen near the centre of the detector (labelled 211 in red), at a Bragg angle consistent with both cd and the higher pressure phases. In this case, the nature of the arc could be examined, and compared with the other diffraction arcs, to try to determine which phase is the cause.

The increase in azimuthal spread from early to late time is indicative of an initially single crystal sample increasing its mosaicity, effectively becoming more like a poly-

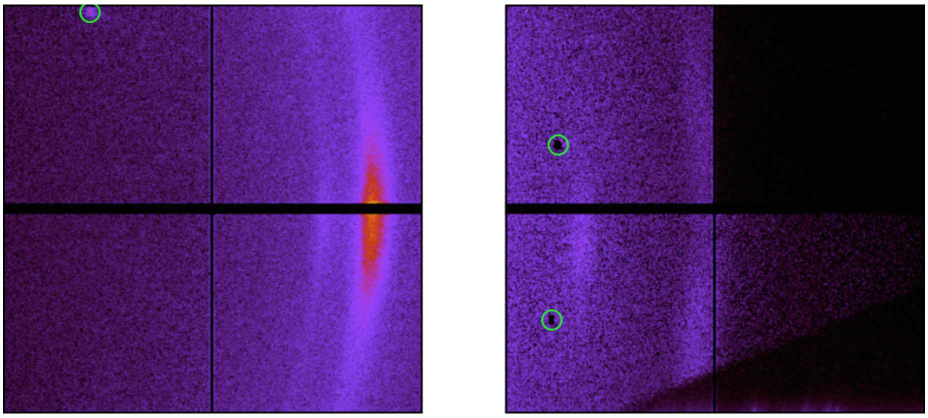

(a) During shock-wave passage.

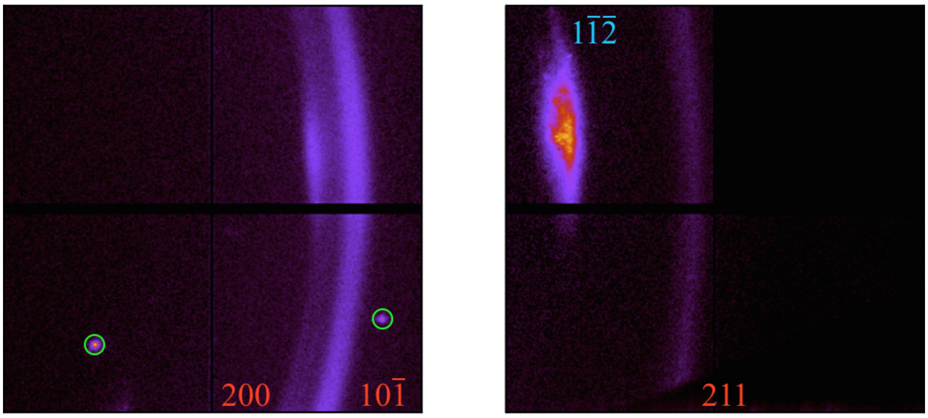

(b) Shortly after rear-surface breakout

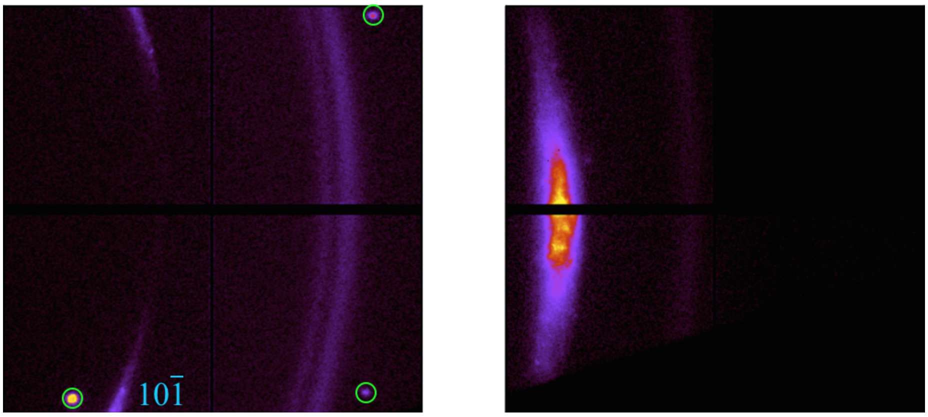

(c) Later time

Figure 5.2: Three representative shots. The cubic diamond (blue) and high-pressure phase (red) arcs are each labelled once. Green circles highlight the 3rd harmonic spots discussed in section 5.5.

crystal, as its grains become more randomly oriented. This is exhibited as a change in the nature of the diffraction pattern from well-contained diffraction spots, at early time, to partially/fully formed Debye-Scherrer rings, at late time. In what follows, we refer to partially formed Debye-Scherrer rings as ‘arcs’, where the arc-length describes the ϕ extent, and, where necessary, the arc-width describes the θ extent. It should be noted that although our data covers only a modest range in azimuthal angle, we can simulate diffraction for the full azimuthal extent, and in certain cases, the *lack* of a diffraction signal where one is expected is information in itself.

5.5 The third harmonic spots

As the silicon targets were oriented with [001] as the drive direction, when mounting the targets there was some freedom in the rotation of the sample about the [001] axis. This manifests in the data as a rotation, of the entire diffraction pattern, around ϕ. We can see this in figure 5.2b, where the brightest parts of each arc do not lie along the horizontal centre of the detectors, at $\phi = 0$. With no further information, we would not be able to constrain this rotation about the sample normal, and so would not be able to say whether any movement around ϕ was due to normal rotation of the target, or physical behaviour upon driving the sample. However, for this experiment, the previously-mentioned harmonic rejection mirrors were not used, resulting in 3rd harmonic (∼24 keV) x-rays being delivered to the target. It is these x-rays that cause the several small, bright spots that can be seen on the detectors (highlighted with green circles in figure 5.2), most noticeably near the four corners of the left detector. These 3rd harmonic x-rays are considerably less tightly focussed than the fundamental, and so bathe a large portion of the target in 3rd harmonic light. Crucially, as the focal size of the 24 keV x-rays was much larger than the drive spot, these 3rd harmonic spots are broadly independent of the drive pulse, and backlighter timing, and so provide the perfect calibration for the normal rotation of the target.

In addition to this, the 3rd harmonic spots can be used to automatically fit the position of the detectors in space without the need for the usual calibration process. So long as there are at least 3 spots whose displacements from each other cover a large extent in both dimensions of the detector, the position of the detector can be determined accurately. The only choice necessary is to decide one sample orientation that defines zero normal rotation, after which the position of the detectors, and all other sample rotations are fixed. This is, in some sense, superior to the power-diffraction calibration routine often used [125], which does constrain the position of the detectors, but leaves the azimuthal positions unknown. In practice, a combination of these two methods was used to fit the detector positions and sample normal rotations.

As described in section 2.2.4, Laue diffraction usually assumes for simplicity a lattice of point-like intensities in reciprocal space, necessitating a range of energies of x-rays to allow the Laue condition to be met exactly. However, the extremely narrow energy spread of the LCLS means that for the Laue condition to be met for the 3rd harmonic spots, the points in k-space can no longer be assumed to be delta functions. As shown in figure 5.3, an increase in the extent of the reciprocal lattice point would allow the Laue condition to be met even for a monochromatic x-ray beam, so long as the energy was close enough to the ideal energy for the reflection. It is the extreme peak brightness of the LCLS instrument that results in finite diffraction signals from the low intensity extremes of the k-space points.

In figure 5.3a, we show ideal diffraction from a given delta-function (hkl)-point in reciprocal space, with an ideal x-ray energy of, for example, 24.1 keV (*i.e.* close to the 3rd harmonic energy). This is the energy at which the Laue condition is perfectly met. In figure 5.3b, we show the same reciprocal space representation of the sample, but acknowledge that the k-points are now distributions of intensity, centred on the original positions. An x-ray of a slightly different energy, here that of the 3rd

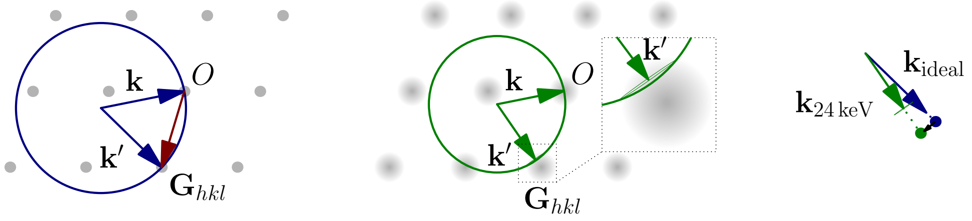

(a) (b) (c)

Figure 5.3: (a) Laue condition exactly met. (b) Laue condition approximately met, allowed by non-delta-function k-spots. (c) Resulting movement of the diffraction spot.

harmonic, 24 keV, still incident on the target along the same direction $\hat{\mathbf{k}}$, can diffract to any position on the Ewald sphere that intersects with the intensity distribution of the k-point. Note however, that the change in incoming x-ray energy means that the centre of the Ewald sphere has moved, and so the average direction of the outgoing x-ray, $\hat{\mathbf{k}}'$, has changed, as seen in figure 5.3c. This results in the 3rd harmonic spots being displaced relative to the perfect Laue spots. This displacement was taken into account when simulating the 3rd harmonic spots, and the simulated pattern fits the data excellently, as shown in figure 5.4.

Finally, this displacement of the 3rd harmonic spots reduces the sensitivity of these spot positions to strain in the crystal, as can be seen from figure 5.5. Coupled with the large spot size of the incident 3rd harmonic x-rays (∼2 mm) relative to the size of the drive spot, this explains why we only see diffracted 3rd harmonic spots from the undriven material. This means that we are insensitive to the elastic regions that caused the 4-spot splitting in chapter 4.

5.6 Time dependence of the material response

In order to gain a better insight into the behaviour of the sample as the pressure wave travels through it, we project the detectors into a frame defined by phi and 2-theta. In this coordinate system, diffraction rings which are circular in real space

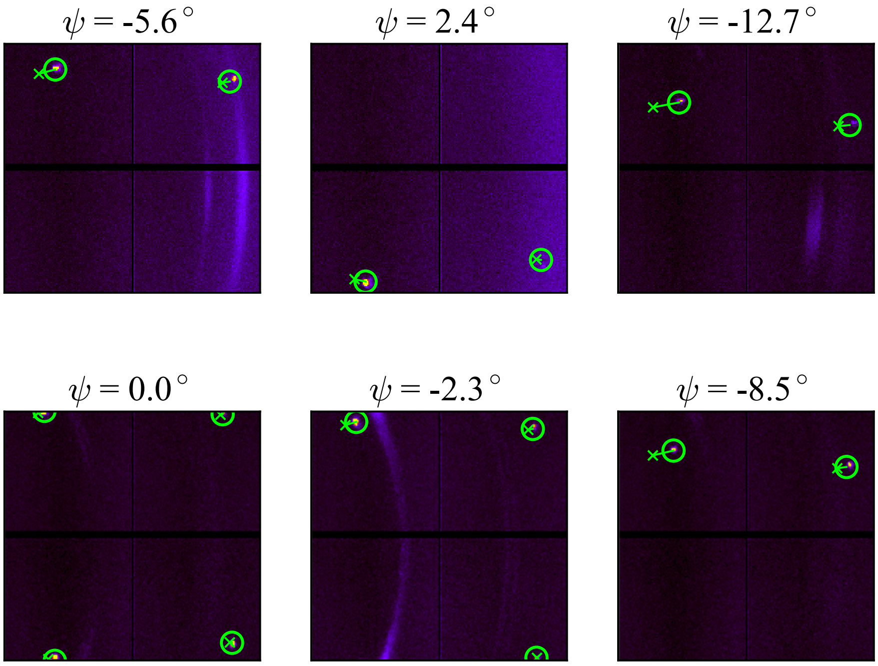

Figure 5.4: Data from six different shots for the left-hand CSpad, each from a sample with a unique normal rotation, ψ. The calculated ideal Laue diffraction spots are shown (crosses), along with the calculated spots allowed at the fixed energy of the third harmonic x-rays (circles). The normal rotations of each sample are given above. This process fits both the detector position and the individual sample rotations, based only on the positions of the automatically detected third harmonic spots.

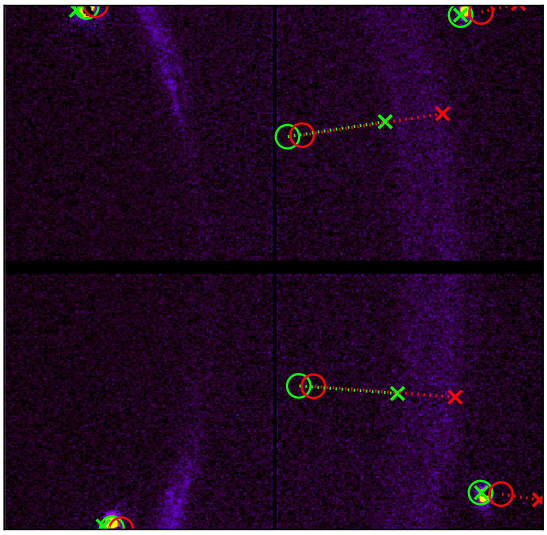

Figure 5.5: Diffraction spot positions are less sensitive to strain when fixed at the energy of the third harmonic x-rays. Calculated positions of ideal energy spots (crosses) and 3rd harmonic spots (circles) are shown for zero strain (green) and 5% strain (red).

(*i.e.* have a fixed Bragg angle) should appear as straight, vertical lines. This is shown in figure 5.6. This projection enables lineouts to be taken, by summing the total intensity for each value of 2-theta, and allows for more direct comparison between different shots.

Given the work in chapters 3 and 4, upon passage of the pressure wave, we expect the material to compress elastically, remaining single crystal, before a mixed phase region is created, formed of crystallites of cubic diamond and β-Sn (or the similar high pressure phases, Imma and simple hexagonal).

We return to figure 5.6, focussing on diffraction from cubic diamond for the time being. For context, we plot on the figure the zero-pressure positions for the cd peaks in this geometry (red dashed lines). Initially, the cubic diamond crystallites have a strain measured between $11.5 \pm 1.5\,\%$ uniaxial and $4 \pm 0.5\,\%$ hydrostatic. With such a limited azimuthal extent of the detectors we initially only have one diffraction peak from cd, and so we are unable to differentiate these two limiting cases. We can see, as the delay of the backlighter increases, the cubic diamond returns towards a zero-strain state. For backlighter delays between 8 ns - 12 ns, two cd peaks are observed, which have positions and large widths consistent with material between $7 \pm 2\,\%$ uniaxial and $1 \pm 0.5\,\%$ hydrostatic strain. The peaks are not consistent with either of these limiting cases alone, suggesting a mixture of strain states in the sample. Late time shots, such as the final lineout shown in figure 5.6, show the cd has returned to zero-strain conditions (red dashed lines).

It should be noted that the transit time of the pressure pulse was such that backlighter delays longer than 6 ns resulted in diffraction from the material after release of the pressure wave from the rear surface, and so the reduction in strain in the cubic diamond is likely from release of pressure, rather than from, say, rearrangement of the crystallites allowing further relaxation.

We now consider the diffraction peaks from the high-pressure phase. At short

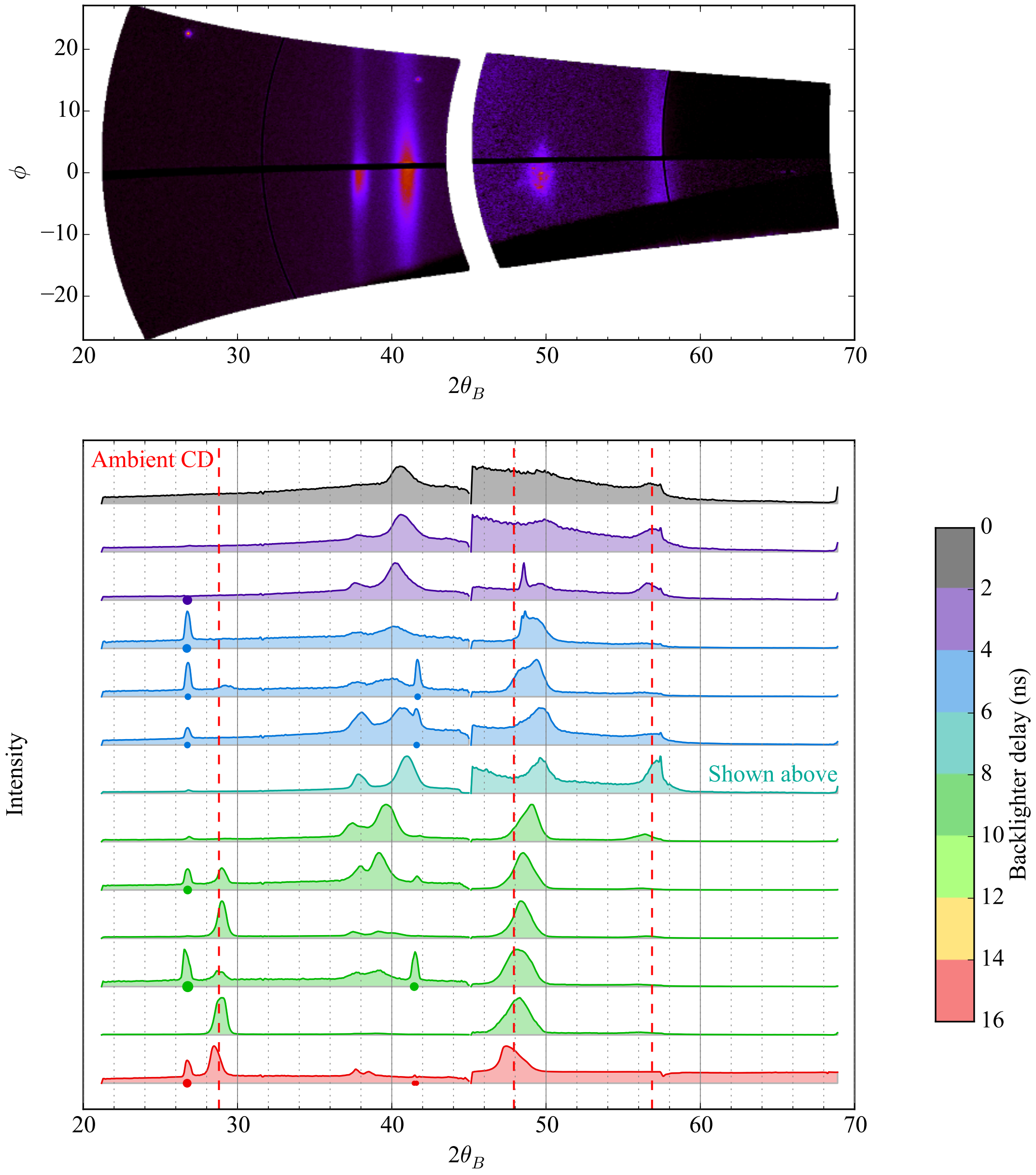

Figure 5.6: Time dependence of the diffraction pattern. We show data from a single shot projected into $2\theta_B$-ϕ coordinates (above). We also show lineouts for shots of different backlighter delays, and highlight the positions of ambient cubic diamond diffraction (dashed red). Third harmonic spots lie at $2\theta_B = 26.8°$, $41.5°$ and $48.6°$, those bright enough to be automatically detected by the analysis code are marked with circular points.

backlighter delays, the diffraction is consistent with a β-Sn structure with lattice parameters of $a = 4.78 \pm 0.02\,\text{Å}$ and $c = 2.53 \pm 0.04\,\text{Å}$. However, we acknowledge that due to the similarities between the β-Sn, Imma and simple hexagonal structures, and with such limited theta-phi detector coverage, we cannot say with confidence which of the three phases we observe. A large peak width in the high-pressure phase could be a combination of two factors: variable strain conditions in the material, and slight asymmetry in the a and b lattice parameters splitting the given peak into two separate, but unresolvable, peaks.

As with the cd, the high-pressure phase peaks move to lower 2-theta, *i.e.* increasing lattice parameters, at later backlighter times, suggesting relaxation. There is much greater movement in the $10\bar{1}$ peak than the 200 peak, suggesting a much greater relaxation along the [001] direction, parallel to the drive direction, than the transverse directions. This is not unexpected given the uniaxial drive pulse.

We note that the appearance of the mosaic cubic diamond material and high-pressure phase concurrently, before the breakout from the rear surface, is consistent with our model of the mixed phase region that has been seen in MD simulations. At time of writing, the author is not aware of any evidence in the literature of direct diffraction from the shock-compressed mixed-phase region of silicon. The appearance of the high-pressure phase in this data corroborates our discussion in chapter 4, which assumed the existence of the mixed phase region to explain the two-plateaux elastic wave profile. Here we see preliminary evidence for just such a region.

5.7 Mosaicity and the orientation of the shocked crystallites

We now attempt to determine the orientation and mosaic spread of those newly formed crystallites (both cd and high-pressure phase) with respect to the original single crystal.

Firstly, we must define what we mean by mosaicity in the crystal. Given an initial reciprocal lattice vector, $\mathbf{G}_{\mathrm{sc}}$, defined by the orientation of the undriven single crystal, we assume for now that the subsequently formed crystallites are oriented preferentially about $\mathbf{G}_{\mathrm{sc}}$. The distribution of angles between the G-vector of each crystallite and $\mathbf{G}_{\mathrm{sc}}$ is defined as the mosaicity. It is simplifying here to think of this as an angle, θ_{max}, above which there are no associated crystallites, and below which there is a uniform distribution of crystallites. In reality, it is more likely to be a smooth gaussian-like distribution centred on $\mathbf{G}_{\mathrm{sc}}$.

As seen in figure 5.7a, the minimum mosaicity, θ_{min}, required for the Laue condition to be met is found by rotating the G-vector from $\mathbf{G}_{\mathrm{sc}}$ towards $\hat{\mathbf{k}}_{\mathbf{0}}$ until it intersects the Ewald sphere. This defines the outgoing k-vector. Diffraction spots on the detectors can extend into diffraction arcs if a mosaicity larger than θ_{min} is present in the sample. This is seen in figure 5.7b, where the larger mosaicity angles allow an arc to form, centred on the original outgoing k-vector.

We now highlight the difference between the behaviour of a crystal with mosaic spread and one which has simply been rotated. In the latter case, each reciprocal lattice vector is rotated about the same axis, passing through the origin (h, k, l)=(0,0,0) as shown in figure 5.8a. In the figure, this single rotation has allowed diffraction from the planes defined by $\mathbf{G}_1$, but the planes defined by $\mathbf{G}_2$ still do not meet the Laue condition, and so do not diffract. Conversely, in figure 5.8b we sketch the case for crystallites with a given mosaic spread around their original orientation. As we can see, now diffraction from planes defined by $\mathbf{G}_1$ and $\mathbf{G}_2$ are both allowed.

For each phase, cubic diamond and the high-pressure phase, we can predict whether a single crystal orientation could be responsible for all the peaks seen in the diffraction pattern at early time, without the need for mosaic spread. We acknowledge that irrespective of the early time behaviour, at later time some mosaicity

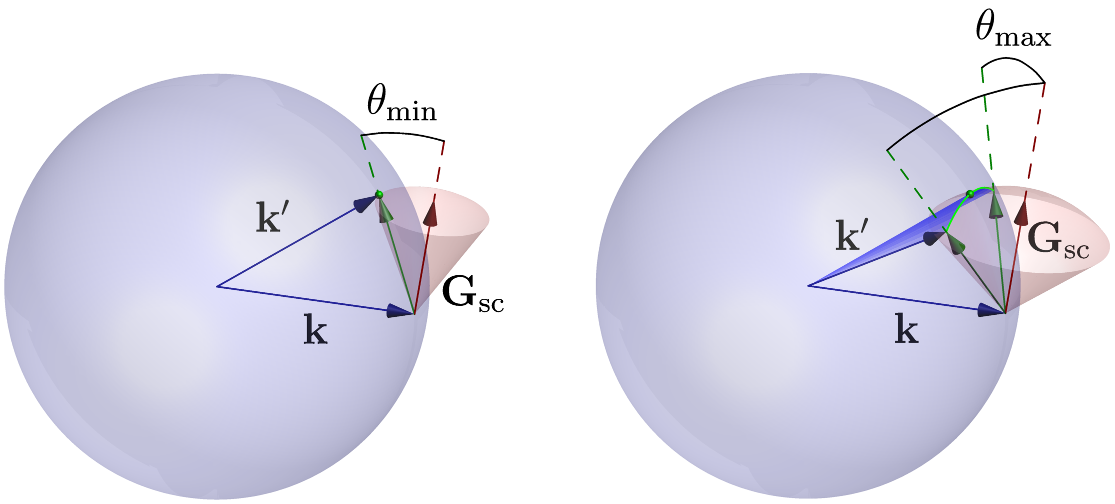

(a) Minimum mosaicity, θ_{min}, for a given single crystal G-vector, $\mathbf{G}_{\text{sc}}$, shown in red, initially not satisfying the Laue condition, to diffract. The locus of all possible G-vectors is shown as the red spherical section, and the G-vector which satisfies the Laue condition is shown in green.

(b) When the mosaicity is greater than θ_{min}, a diffraction arc is formed at the intersection of the Ewald sphere and the spherical section around $\mathbf{G}_{\text{sc}}$. This arc is shown in green.

Figure 5.7: As mosaicity increases, the diffraction from a given set of planes becomes possible. Initially a diffraction spot is formed, but as mosaicity increases this extends into an arc. The initial G-vector, $\mathbf{G}_{\text{sc}}$, is shown in red, and its resulting G-vectors shown in green. The incoming x-rays with wavevector $\mathbf{k}$ and outgoing wavevector $\mathbf{k}'$ are shown as blue arrows. The Ewald sphere is shown in blue.

will be necessary to allow the peaks to spread azimuthally into arcs.

As an example, we consider the $11\bar{2}$ peak from cubic diamond, seen on the right detector in figure 5.2. For any given single crystal orientation (of the [001] crystal axis), we will be able to find a minimum mosaicity at which the $11\bar{2}$ plane (or any of the $\{112\}$ family) will diffract to this position on the detector. If the orientation is optimal for this reflection, this mosaicity will be small. However, when several diffraction peaks are considered collectively, it is not certain that a distinct single crystal orientation exists that would cause diffraction at each position on the detector simultaneously. We can therefore calculate the optimum crystal orientation to allow diffraction at several points. We define this as the orientation of the [001] crystal axis that requires the smallest mosaicity to satisfy the Laue condition for all the points

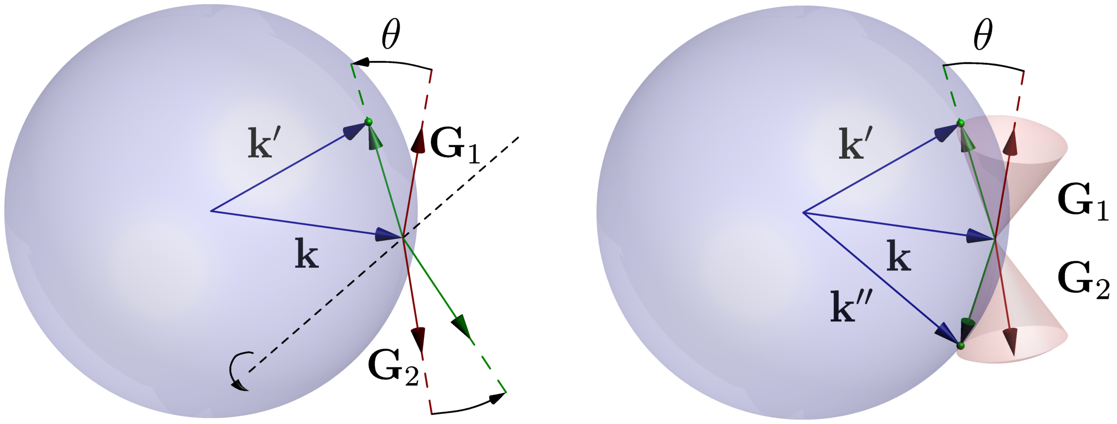

(a) Rotation of a single crystal by an angle θ. Only those planes defined by $\mathbf{G}_1$ satisfy the Laue condition after the rotation. Planes defined by $\mathbf{G}_2$ do not diffract.

(b) Mosaicity of θ. Now both planes defined by $\mathbf{G}_1$ and $\mathbf{G}_2$ can diffract. The loci of all possible G-vectors are shown as the red spherical sections, with those that satisfy the Laue condition shown as green arrows.

Figure 5.8: Highlighting the difference between single crystal rotations and increasing mosaicity. Two initial G-vectors, $\mathbf{G}_1$ and $\mathbf{G}_2$, are shown in red, and their resulting G-vectors shown in green. The incoming x-rays with wavevector $\mathbf{k}$ and outgoing wavevectors $\mathbf{k}'$ (and $\mathbf{k}''$) are shown as blue arrows. The Ewald sphere is shown in blue.

being considered.

When considering all cubic diamond diffraction spots for which we know the detector position accurately, that is the three already mentioned, this constrains the possible orientation of the crystallites well. This is shown in figure 5.9. Firstly, we show the mosaicity required for each of the reflections in the $\{112\}$ family to diffract to the detector position seen in the data (figure 5.9 top). In the centre row of the figure, we show the collective minimum of all of these reflections, as each reflection in the family is equivalent. We show an equivalent plot for the family that diffracts to the two other spots we are considering (which lie off the detector in figure 5.2). As described, we want to find the crystal orientation that requires the minimum mosaicity to satisfy the Laue condition for all of these detected spots simultaneously, and therefore take the minimum of the plots for each of the families. This yields the final plot in figure 5.9. We can see that an orientation of $(\phi, \theta) = (0, -12^\circ)$ would create all three diffraction spots in the data with a modest mosaicity of 4°. Alternatively, if we were to assume that the average orientation of the crystallites did not change from the undriven single crystal orientation (*i.e.* position (0,0) on the plot) a larger mosaicity of 12° would be necessary to allow diffraction at each of the 3 points simultaneously.

For the high-pressure phase (figure 5.10), the data only gives us the positions of two peaks with which to carry out this analysis, the two introduced in section 5.4. However, a different situation from the cubic diamond is seen. While the {200} spot has a minimum mosaicity at an average crystal orientation of $(\phi, \theta) = (\pm 45°, +31°)$, the $\{10\bar{1}\}$ spot requires an average crystal orientation of $(\phi, \theta) = (\pm 45°, -30°)$. The choice of $\phi = \pm 45°$ is arbitrary, as the tetragonal (or approximately tetragonal) nature of the high-pressure phase makes the two rotations equivalent for these reflections.

This suggests two limiting cases for the nature of the high-pressure phase after the passage of the shock, as shown schematically in figure 5.11. Both require a rotation of ±45° about the [001] crystallographic direction with respect to the unshocked crystal. The first of these cases (Case 1) is that the sample contains two (or more) variants of the high-pressure phase, each with low mosaicity about a specific single crystal orientation, two of which we have found here ($\theta = +31$ or -30). Alternatively, (Case 2) the sample could contain crystallites of the high-pressure phase that have an unchanged average crystal orientation ($\theta = 0$), but a high mosaicity, $\sim 31°$. The former option agrees more closely with the MD simulations of chapters 3 and 4, and previous MD work [93], which found the nucleation of 4 possible bands of Imma phase, each with a well defined orientation. However, we must stress that the 45° phi-rotation of the high-pressure phase is not observed in the MD simulations. Indeed, diffraction patterns produced from MD shock simulations, as illustrated in figure 5.12, show peaks corresponding to the cubic diamond peaks in the data, but no observable diffraction from the high-pressure phase is predicted. This implies that the MD does not fully capture the true behaviour of the high-pressure phase during the experiment.

(a) Each reflection that can contribute to the first detector peak:

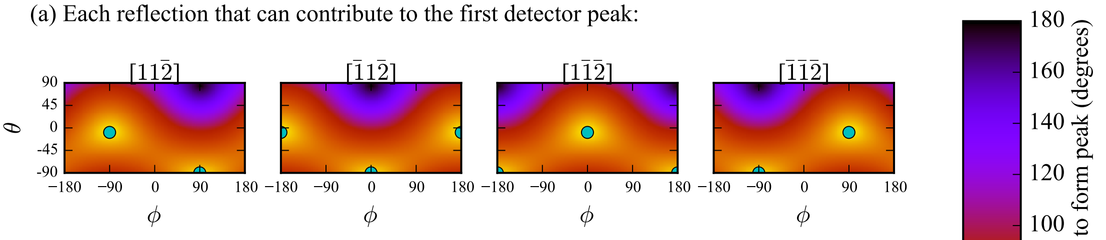

(b) Each detector peak:

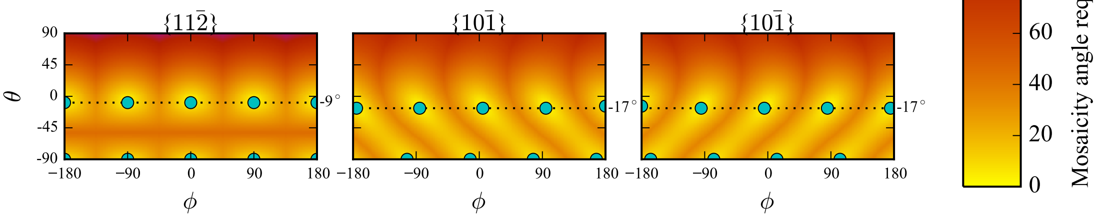

(c) Minimum mosaicity required to produce all peaks from one average orientation:

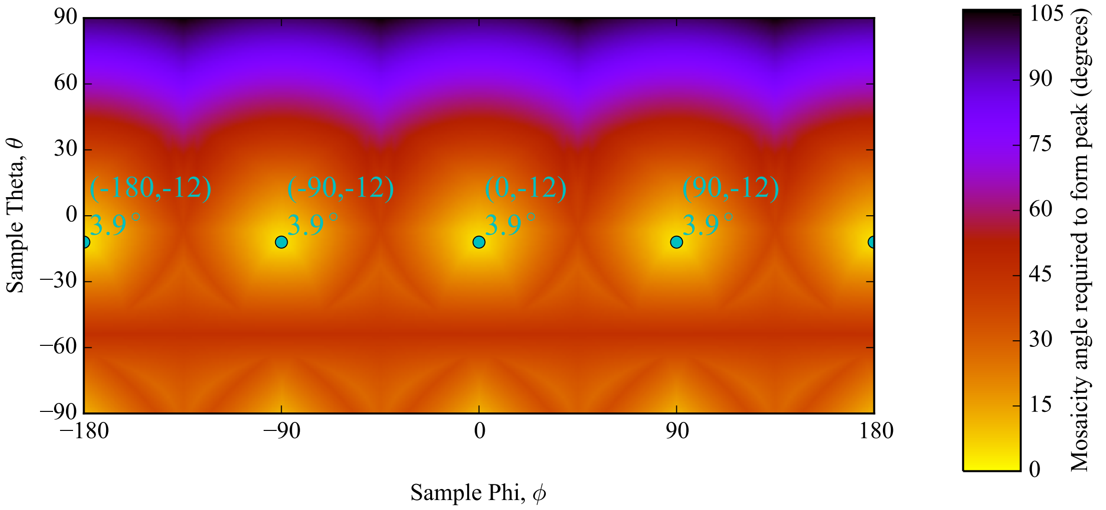

Figure 5.9: Possible orientations of cubic diamond that produce the diffraction peaks seen on detector. Local minima for each plot are shown as cyan points.

(a) Each reflection that can contribute to the first detector peak:

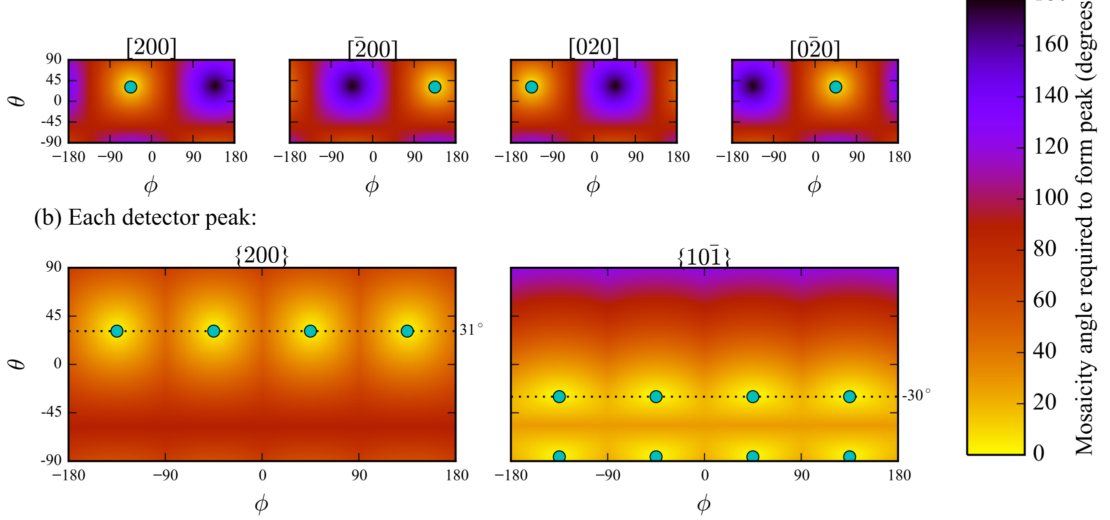

(b) Each detector peak:

(c) Minimum mosaicity required to produce all peaks from one average orientation:

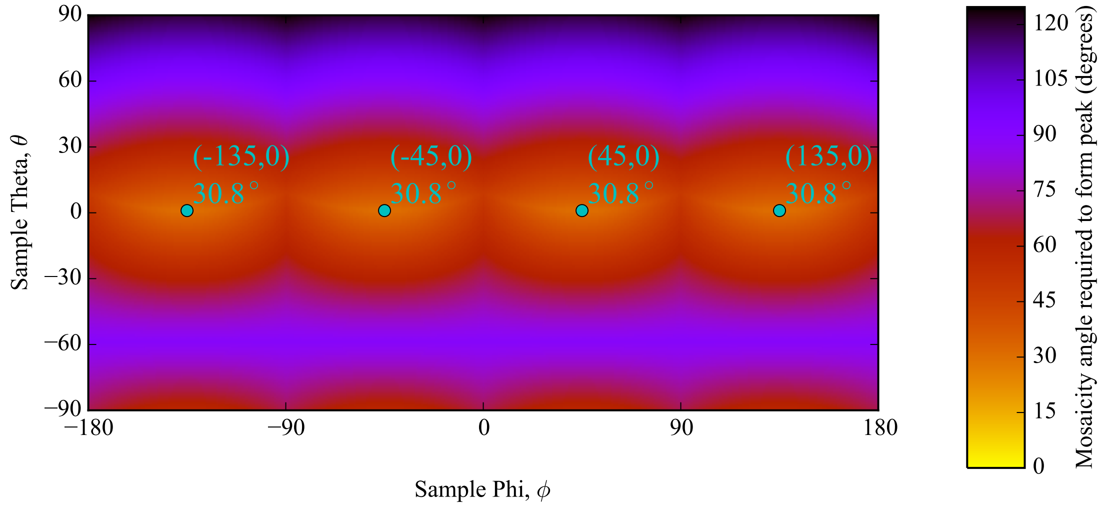

Figure 5.10: Possible orientations of β-Sn that produce the diffraction peaks seen on detector. Local minima for each plot are shown as cyan points. This suggests two limiting cases for the composition of the high-pressure phase, shown in figure 5.11.

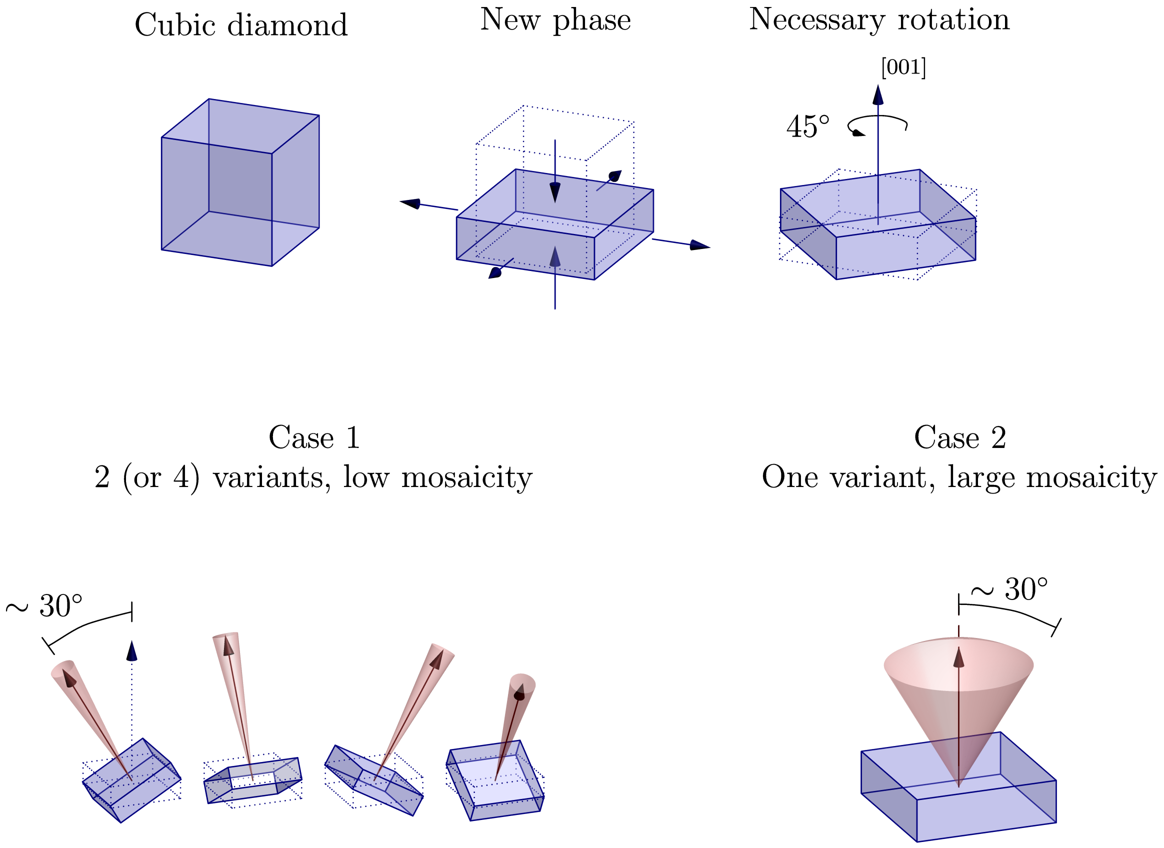

Cubic diamond

New phase

Necessary rotation

Case 1
2 (or 4) variants, low mosaicity

Case 2
One variant, large mosaicity

Figure 5.11: Two suggested limiting cases for the nature of the high-pressure phase. The 45° rotation (top right) may be a manifestation of a small basis change, rather than a macroscopic shift of all atoms by 45°.

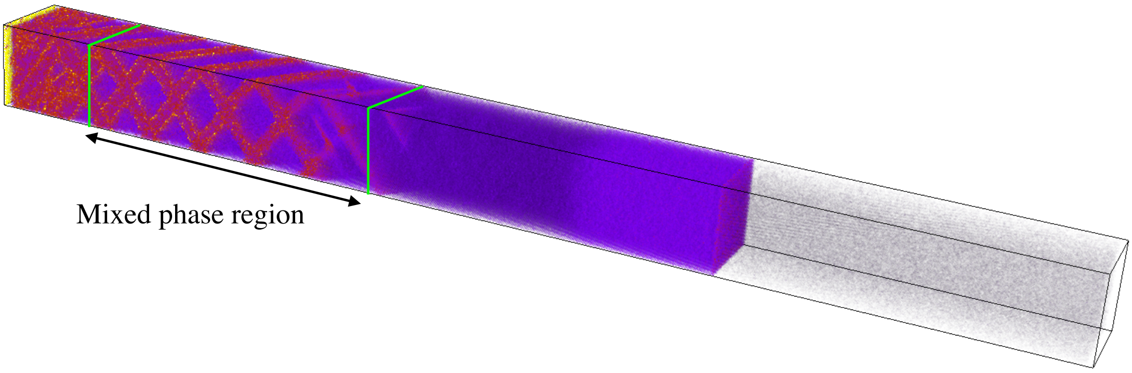

(a) MD shock simulation. Peak drive stress 32 GPa.

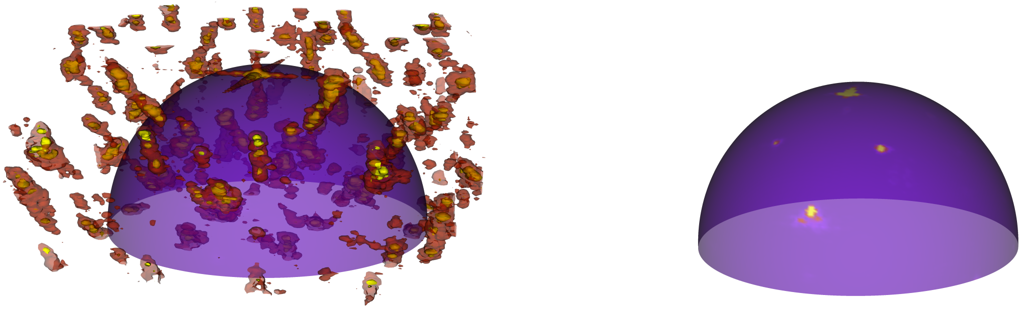

(b) Reciprocal space representation of mixed phase region with Ewald sphere shown.

(c) Reciprocal space intersections with Ewald sphere.

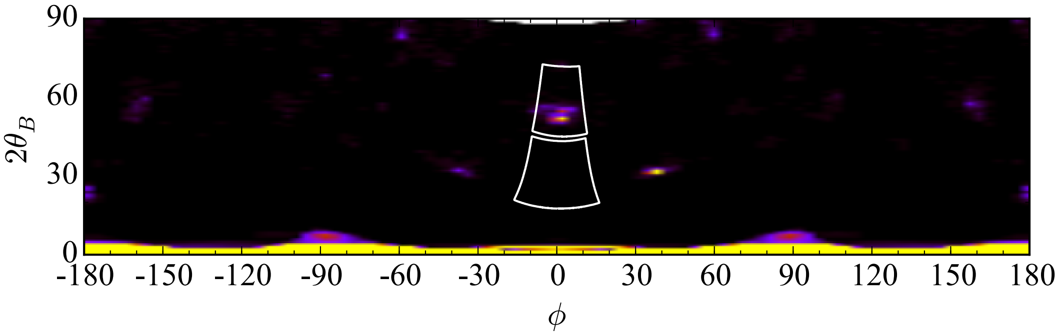

(d) Simulated diffraction.

Figure 5.12: Simulated diffraction from an MD shock simulation. Colour shows intensity (in arbitrary units). (a) Potential energy plot of an MD shock simulation, with peak drive stress of 32 GPa. (b) Fourier transform of the mixed phase region gives the reciprocal space representation. The Ewald sphere for all possible forward diffraction directions shown as the hemi-sphere. (c) Ewald sphere intersections, with the FT removed for clarity. (d) ϕ - $2\theta_B$ representation of the Ewald sphere intersections. The positions of the experimental detectors are shown as white outlines. The predicted diffraction agrees qualitatively with the observed diffraction from cubic diamond in the data, but there is no simulated diffraction matching the diffraction arcs from the high-pressure phase.

5.7.1 Approximating mosaic spread from arc-lengths

As shown in figure 5.7b, once the minimum mosaicity criterion for diffraction is reached, increasing the mosaicity further enables the diffraction spot to increase its azimuthal-extent, becoming a partially-formed Debye-Scherrer ring, or arc. In principle, it should be possible to measure the azimuthal extent of these arcs, here referred to as the arc length, to determine the mosaicity in the sample. We now perform that analysis.

Firstly, we simulate how the detected arc length would be related to the mosaic spread in a perfect material. This is achieved by taking the Fourier transform (FT) of a small, thermalised sample of cubic diamond or β-Sn from MD. The intersections of this reciprocal space intensity distribution with the Ewald sphere, defined by $\mathbf{k}_0$, gives the predicted diffraction. By rotating the FT around axes perpendicular to the [001] direction, and calculating the Ewald sphere intersections in each case, we can emulate mosaicity in the sample. This process produces diffraction patterns qualitatively similar to those seen in the data, though matching exact 2-theta positions would require a full sweep of unit cell parameters. For this analysis, which concerns the arc-lengths, a single, zero-pressure cd or β-Sn sample is used. By measuring the predicted arc-length for each value of allowed mosaicity, we calculate a one-to-one relationship between arc-lengths on the detector and mosaic spread in the material. This analysis is illustrated in figures 5.13 and 5.14. It should be noted that this analysis requires a choice of model for mosaic spread, *i.e.* one must choose between the two limiting cases described in the previous section, or an alternative intermediary case. The analysis shown here assumes a material with unchanged average crystallite orientation and large mosaic spread (Case 2). The same analysis was completed for Case 1, but the well ordered, small MD samples resulted in the simulated diffraction being extremely strong in the centre of each arc, meaning a relationship between mosaicity and arc-length predicted extremely short arcs (arc-length $< 2°$) for all mosaic spreads.

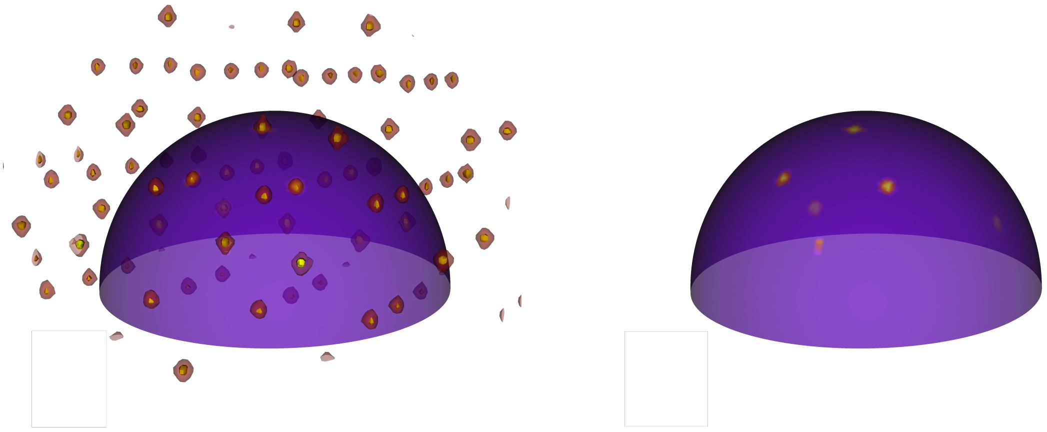

(a) Reciprocal space representation with Ewald sphere shown.

(b) Reciprocal space intersections with Ewald sphere.

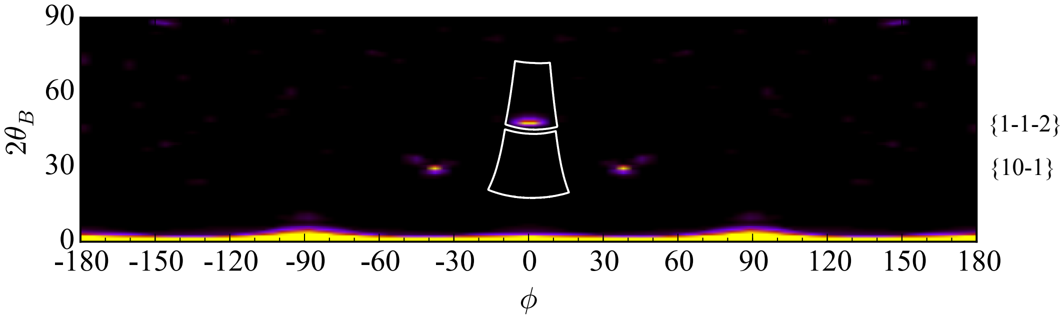

(c) Single orientation.

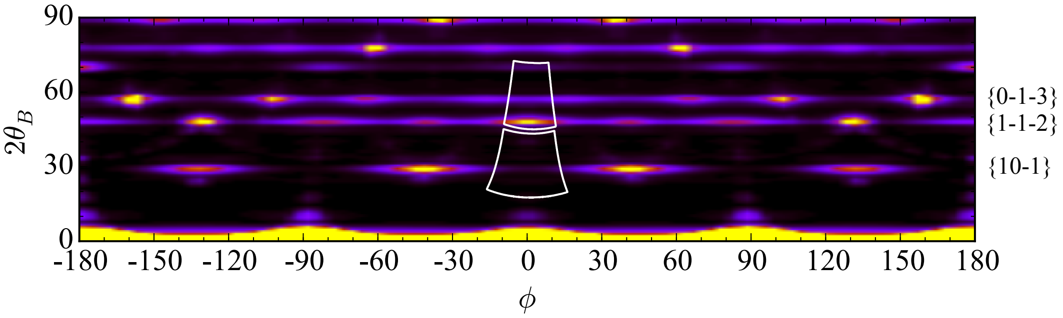

(d) Crystal with mosaic spread.

Figure 5.13: Predicted diffraction from cubic diamond. Colour shows intensity (in arbitrary units). (a) Reciprocal space representation of the cubic diamond phase, with an orientation of $(\phi, \theta) = (0, -12°)$, the Ewald sphere for all possible forward diffraction directions shown as the hemi-sphere. (b) Ewald sphere intersections, with the cubic diamond FT removed for clarity. (c) ϕ - $2\theta_B$ representation of the Ewald sphere intersections for this single orientation. The positions of the experimental detectors are shown as white outlines. (d) Calculated diffraction for a crystal with a mosaicity spread of 30°.

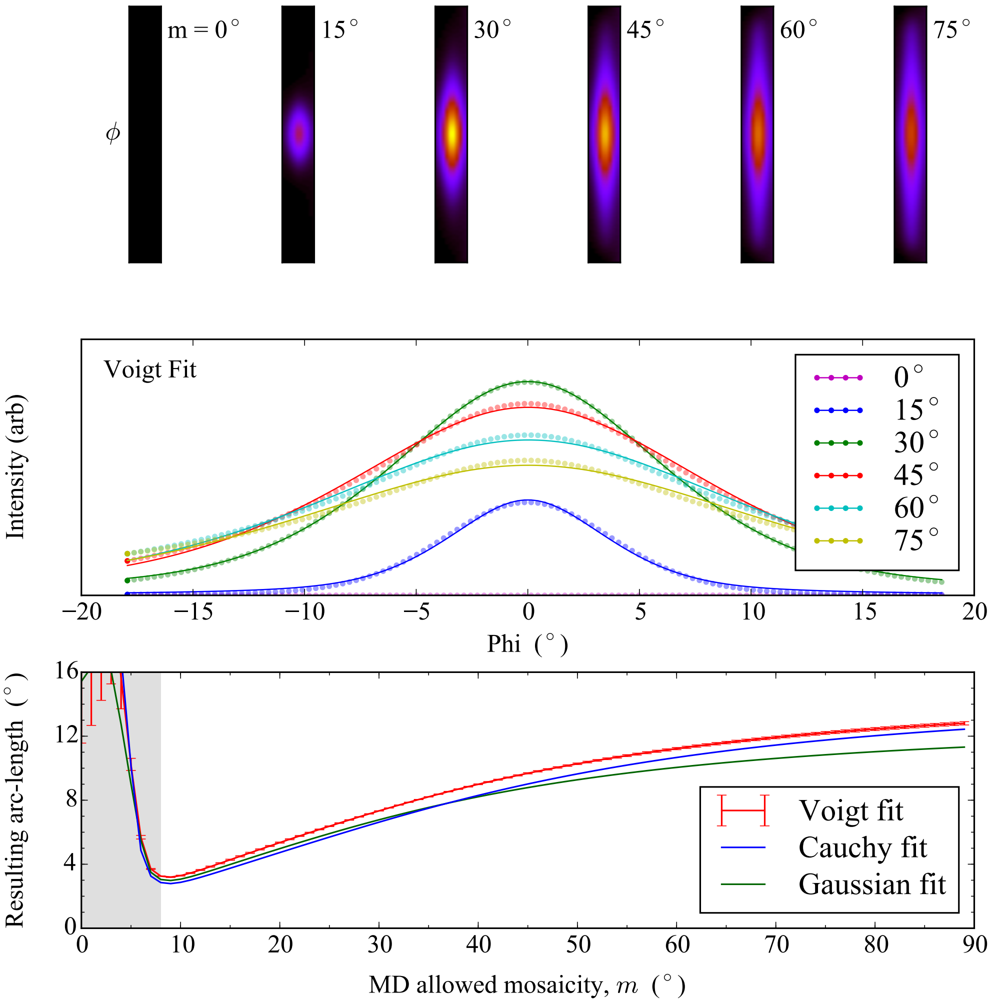

Figure 5.14: Using MD to calculate the relationship between mosaic spread and arc-length in perfect samples. We show the 200 arc from β-Sn for several mosaicities (top). We sum the intensity for each point in ϕ, and by fitting Voigt curves to these intensity profiles (centre) we can relate the mosaic spread in the crystal to the expected arc-length on the detector (bottom). We define the arc-length as the standard deviation on the width of the best fit profile. We note that due to very low simulated diffraction intensity at mosaicities $\lesssim 8°$, fitting a Voigt profile is problematic. This region is highlighted in the lower plot in grey, where the increase in calculated arc-length is a shortcoming of the fitting process, and not a true response of the diffraction arc.

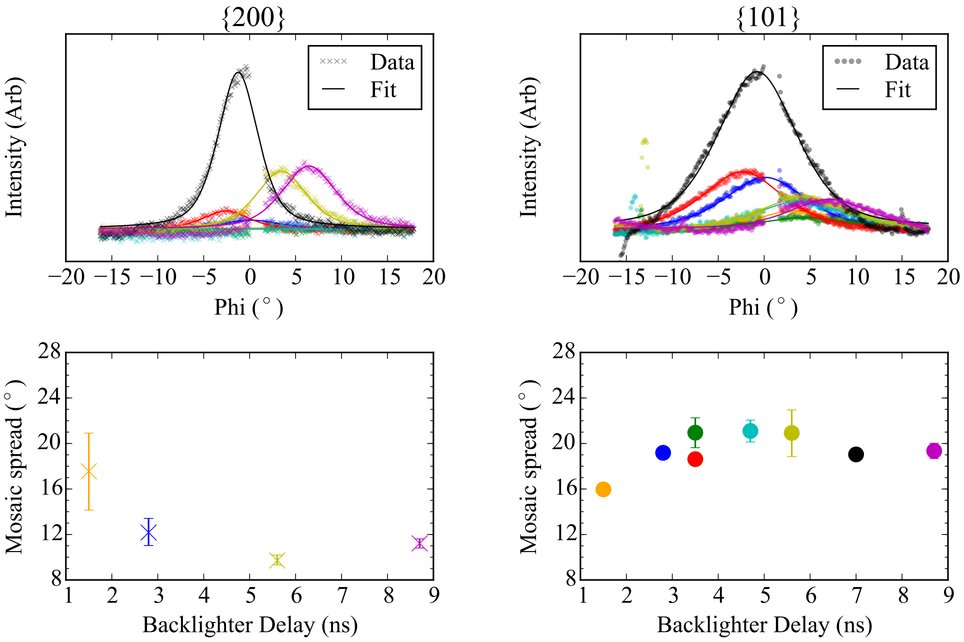

Figure 5.15: Measuring the mosaic spreads in the samples from the arc lengths on the detectors. This analysis suggests that the mosaic spread does not increase with time, as initial inspection of the data had suggested. We acknowledge that the calculated mosaicity should be consistent for the two arcs, but that the data above suggest otherwise. There are fewer points in the lower plot of the {200} arc than that of the {101} arc, as those points lay outside the range of the map from arc-length to mosaicity (figure 5.14 lower plot).

In figure 5.15, we calculate the mosaicity in the sample from the arc-lengths on the detectors for several shots over a range of backlighter delays. This suggests that the mosaicity doesn't evolve considerably in time, contrary to preliminary consideration of the data. With this is mind, any apparent increase in the arc-length must be a manifestation of the diffraction arc increasing in brightness, making the extremes of the arc visible above the noise. We also note that, given it is a property of the sample, the mosaicity for a given phase should be consistent when measured from different diffraction arcs. From the two arcs considered in figure 5.15, we see this is not the case. This may be further evidence that the assumption of a single average orientation and large mosaicity, on which figure 5.15 is based, is not a good description of the nature of the high-pressure phase.

Unfortunately, with just two arcs for the high-pressure phase, and only one for the cubic diamond, such measurements of the sample mosaicity are far from conclusive. We discuss possibilities for an experiment which is more sensitive to this property in section 6.2.

5.8 Phase in release

At late times, the sample will be in the process of releasing back to zero-pressure. Several metastable phases have been described in the literature which remain stable on release from high pressure to ambient conditions. These are: BC8 (Si-III), a body-centred cubic structure with 8 atoms in the unit cell [103, 126, 127]; the closely related structure R8 (Si-XII), a rhombohedral lattice which undergoes a reversible phase change from BC8 [128]; and two as-yet unknown tetragonal structures, named Si-VIII an Si-IX in the original paper [129]. Adapting diffraction patterns from the literature [130, 129] to match our geometry, we plot the ambient diffraction patterns from these phases in figure 5.16, along with a lineout of our data from a late time shot. We also mark the ambient diffraction from cubic diamond (green dashed lines). It is clear that while the diffraction from cubic diamond agrees well with predicted ambient diffraction from cd, none of the described release phases show good agreement with the four high-pressure phase peaks in our data at $2\theta_B = \sim 37.7°, 38.7°, 55.0°$ and $55.6°$ (highlighted with magenta triangles in figure 5.16). One possible explanation for this is that the original experiments were carried out using diamond anvil cells, for which the timescale of the release was $\gtrsim 1\,\mathrm{s}$. It may be that the timescale for the formation of these metastable phases is much longer than our experimental timescale of 10s of ns. The best fit to these four diffraction peaks is found from a β-Sn structure (or Imma or sh with $a \approx b$) with unit cell parameters of $a = 4.8\,\text{Å}$ and $c = 2.68\,\text{Å}$, which gives a $c/a = 0.558$. Extrapolating measured unit cell dimensions for β-Sn

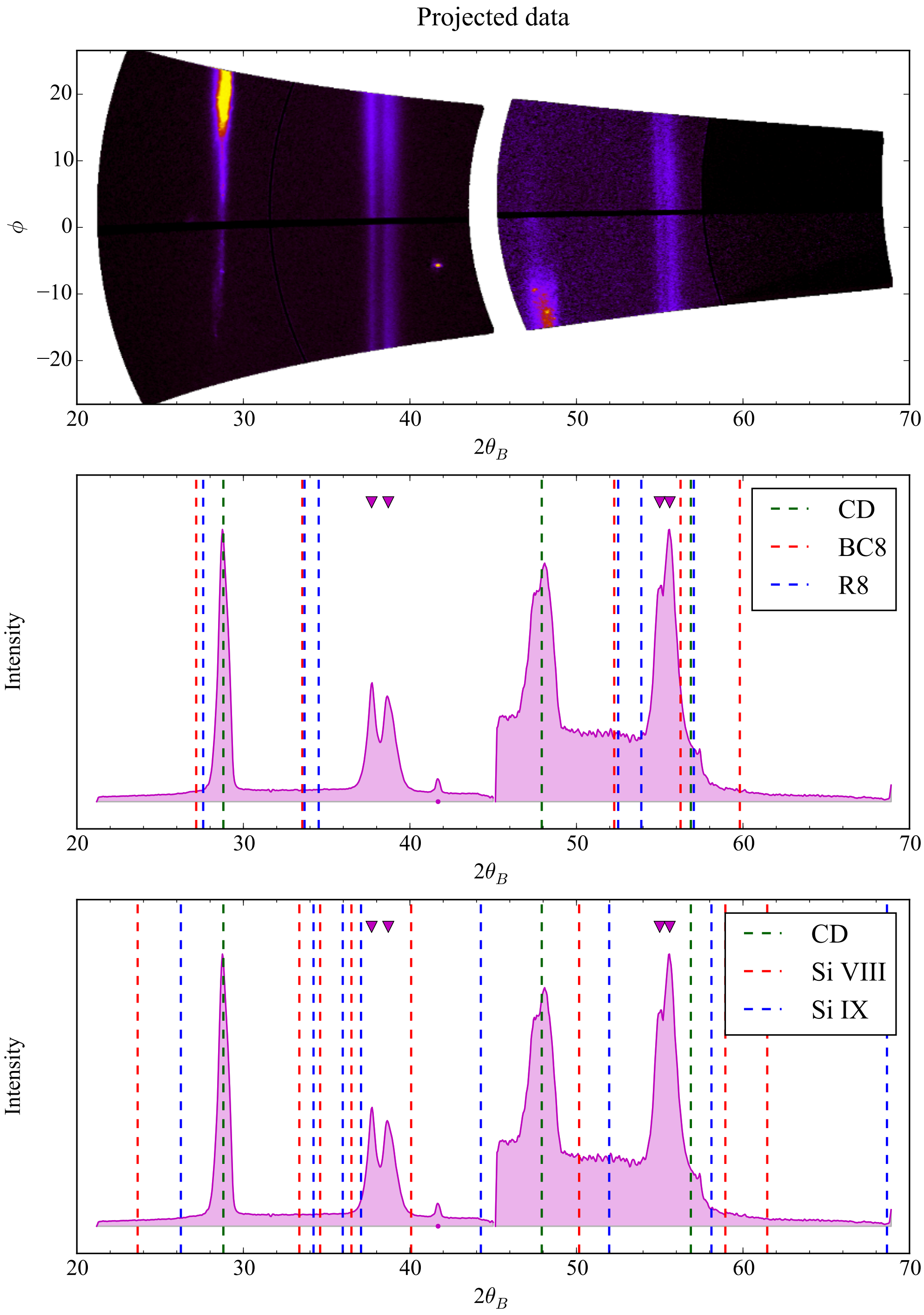

Figure 5.16: Late time shot, 16.9 ns after the onset of the drive pulse. The top plot shows the projected data, while the bottom two show the summed intensity for each value of $2\theta_B$. We note that none of the metastable, release phases seen in the literature at zero pressure (red/blue dashed lines), match the diffraction rings at $\sim 37.7°, 38.7°, 55.0°$ and $55.6°$ (highlighted with magenta triangles). The two strong cubic diamond lines are in good agreement with the predicted zero-strain positions (green dashed).

from McMahon *et al.* [92] gives this phase as in tension (1-2 % hydrostatic), though it should be noted that the lower limit of measurements for β-Sn in that reference is 12 GPa, and therefore the extrapolation is considerable.

5.9 Further work

The clear step for further work here is to analyse the VISAR traces that were recorded during the experiment. Unfortunately, as the main focus of the work to this point was to investigate the development of mosaicity from a single crystal, time constraints made analysis of the VISAR impractical. If analysed and of good quality, not only could this give insight into the peak drive pressures, but possibly the pressure of the elastic wave and any phase-change waves. Whilst determining the pressure of the phase-change wave may further constrain which high-pressure phase we observe in the diffraction, the similarity of those phases in terms of structure and symmetries renders any further constraint somewhat inconsequential in terms of answering the current questions: those of mosaic spread and orientation of the resulting crystallites.

One feature of the VISAR traces could be of great importance to the overall picture however, and that is whether they show evidence for the kind of two-plateaux elastic wave-profile that we inferred from the data in chapter 4. If this evidence was observed, it would corroborate our explanation for the so-called *anomalous* elastic response of silicon, which was given in chapter 4 based purely on diffraction data.

5.10 Summary

We have observed diffraction showing that on passage of pressure waves somewhat below 50 GPa, single-crystal [001]-oriented silicon undergoes a phase change to a high-pressure phase consistent with strained β-Sn. The appearance of diffraction from both cd and high-pressure phase crystallites concurrently suggests a mixed phase region, similar to that seen in MD simulations. The orientation and mosaic spread of the crystallites of each phase in the mixed-phase region is not perfectly constrained, however limiting cases for each phase have been suggested. A rotation of 45° around the [001] axis is seen in the crystallites of the high-pressure phase, relative to the initial orientation, which was not expected. A possible mechanism for this rotation is not yet known.

Chapter 6

Summary and Future work

6.1 Summary

The first complete description of the recently developed Lagrangian elastic (LE) code is given in chapter 3. We focus on the ability of the code to model a phase-change to a mixed-phase region, such as that seen in molecular dynamics (MD) simulations of shock-compressed silicon. We highlight the code's ability to calculate and store the stresses and strains in each of the phases contained therein. Knowledge of these strains is crucial when simulating diffraction from the sample. We show that with the inclusion of a physically motivated boundary softening term, close agreement between the LE and MD simulations is seen. The code requires three fitting parameters, each with a physical meaning, and a distinct effect on the resulting wave profiles: a boundary softening coefficient, a phase-change growth-rate coefficient, and the pressure which marks the onset of the phase-change. The much greater efficiency that is inherent in the LE code, compared with MD simulations, makes it possible for large numbers of simulations to be carried out using even modest computing resources. This may becoming increasingly important when simulating future experiments, as they are fielded on facilities with ever-increasing repetition rates, such as the LCLS and the European XFEL.

Data from a recent white-light Laue diffraction experiment at The Orion Laser Facility is introduced and analysed in chapter 4. The experiment investigates the response of [001]-oriented single-crystal silicon to shock compression, with peak stresses between 28 - 65 GPa. Two clear spots are seen in compression, and an unexpected spot is repeatably seen in tension. Supplementary MD simulations suggest that a kinetically inhibited phase-change would create a transient two-plateaux elastic wave profile. A small addition to the LE code to temporally inhibit phase-changes enables diffraction from these two distinct elastic regions to be simulated. By comparing the simulated diffraction to the data we are able to calculate the stresses and normal strain of the two elastic regions, and show that the strain of each region is independent of drive pressure for the full range of drive pressures explored. This is strong evidence that both strain values are related to phase changes, and mark the boundaries of the conditions in the sample for which each phase is energetically favourable under dynamic compression. The description of the two distinct elastic regions given in this work may provide an explanation for the previously observed *anomalous* elastic response of silicon to short time- and length-scale shock-compression experiments.

The LCLS experiment on [001]-oriented single crystal-silicon described in chapter 5 offers further detail to the description. By using extremely bright, monochromatic x-rays, this experiment was sensitive to different material behaviour from the previous experiment. The diffraction data recorded during the experiment show clear evidence of a high-pressure phase created upon shock compression. There are currently no observations of diffraction from a high-pressure phase of silicon, during dynamic compression experiments, in the literature. The diffraction from this phase is consistent with a tetragonal structure, specifically a non-hydrostatically strained β-Sn structure. However, similarities in the structure of the β-Sn, Imma and simple hexagonal phases of silicon, and the limited angular coverage of the detectors, make it extremely difficult to determine the phase precisely. The presence of diffraction from both cubic diamond and high-pressure phase crystallites concurrently, and before the breakout of the pressure wave from the rear surface, is consistent with a mixed phase region existing in the sample. The positions and azimuthal extents of the diffraction arcs suggest limiting cases for the orientation and mosaic spread of the crystallites of each phase, though again, limited detector coverage makes constraining further the mosaic spread of the crystallites of either phase impractical. We observe a 45° degree rotation, about the drive axis, of the high-pressure phase crystallites with respect to the initial crystal orientation, which is not seen in MD studies, and for which a mechanism of rotation is not currently known.

6.2 Future work

In order to more closely investigate the mosaic spread of the crystallites that are created under shock compression, a future experiment could use the tuneable nature of the x-ray energy at the LCLS (0.25-9.5 keV) to 'scan' through reciprocal space. To demonstrate, we return briefly to the bottom portion of figure 5.11, which illustrates the two suggested limiting cases for the nature of the crystallites. As we have discussed, the diffraction from a material is related to the intersections of the Ewald sphere with the reciprocal space intensity, which is shown as the red spherical sections in the figure. The two cases shown in the figure have very different reciprocal space intensity distributions, and by increasing the x-ray energy, and therefore the Ewald sphere radius, it would be possible, in principle, to map out this reciprocal space intensity distribution. This may provide strong evidence for one case or the other, or indeed suggest that an intermediary case is more realistic. This method is particularly attractive, in contrast to requiring larger detector coverage, for two reasons: increasing the number of detectors is expensive; and it is not always possible due to spatial constraints in a crowded target chamber. Conversely, sweeping the energy of the x-rays as described here does not increase the experimental requirements, as it is already a working property of the LCLS. It should be noted that two further CSpads were present on this experiment but their positions yielded minimal data. Judicious choice of positioning for the additional CSpads based on the findings described in this work, and on simulated diffraction patterns, could allow firmer conclusions to be drawn.

6.3 Final thoughts

With the Lagrangian elastic code, we have developed a new tool to investigate the response of materials to shock compression. With the advent of the unexpected tension spot from the white-light Laue diffraction experiment, it was almost immediately adapted to accommodate kinetically inhibited phase-changes, such is the pace of the current understanding. We have also seen that successfully investigating the evolution of crystalline materials, formed from the shock-compressed of single crystals, will require thoughtful consideration and exquisite experimental planning before any firm conclusions can be drawn.

The response of silicon to high pressure has always been a complex and intriguing puzzle. Our aim with this work was to correctly place one more piece of the jigsaw, and we hope that has been achieved. However, the puzzle is by no means complete, and what's more, it's not even clear how many pieces are still left in the box.

Bibliography

[1] John W. Taylor. Thunder in the mountains. In *Shock Waves in Condensed Matter-1983*, pages 3–15. Elsevier Science Publishers BV, 1984. (Cited on page 1.)

[2] L. V. Al'Tshuler. Experiment in the soviet atomic project. In I.M. Dremin and A.M. Semikhatov, editors, *Proceedings of the Second International A. D. Sakharov Conference on Physics: Moscow, Russia 20-24 May 1996.* World Scientific, 1997. (Cited on page 1.)

[3] Peter O.K. Krehl. *History of shock waves, explosions and impact.* Springer-Verlag Berlin Heidelberg, 2009. (Cited on page 1.)

[4] Denis Keefe. Inertial confinement fusion. *Annual Review of Nuclear and Particle Science*, 1982. (Cited on page 1.)

[5] Thomas Hamacher, Matthias Huber, Johannes Dorfner, Katrin Schaber, and Alex M. Bradshaw. Nuclear fusion and renewable energy forms: Are they compatible? *Fusion Engineering and Design*, 88(6-8):657–660, 2013. (Cited on page 1.)

[6] T Guillot. Interiors of giant planets inside and outside the solar system. *Science (New York, N.Y.)*, 286(5437):72–7, oct 1999. (Cited on page 2.)

[7] Frank D. Stacey. High pressure equations of state and planetary interiors. *Reports on Progress in Physics*, 68(2):341–383, 2005. (Cited on page 2.)

[8] D. C. Swift, J. H. Eggert, D. G. Hicks, S. Hamel, K. Caspersen, E. Schwegler, G. W. Collins, N. Nettelmann, and G. J. Ackland. Mass-Radius Relationships for Exoplanets. *The Astrophysical Journal*, 744(1):59, jan 2012. (Cited on page 2.)

[9] Francis Birch. Elasticity and constitution of the Earth's interior. *Journal of Geophysical Research*, 57(2):227–286, 1952. (Cited on page 2.)

[10] Frank Sohl and Tilman Spohn. The interior structure of Mars: Implications from SNC meteorites. 102:1613–1635, 1997. (Cited on page 2.)

[11] Thomas G. Sharp and P. S. de Carli. Shock effects in meteorites. *Meteorites and the Early Solar System II*, pages 653–677, 1988. (Cited on page 2.)

[12] K. Holsapple and E. Ryan. Asteroid Impacts : Laboratory Experiments and Scaling Laws. *Asteroids III*, pages 443–462, 2002. (Cited on page 2.)

[13] A. G. W. Cameron and W. R. Ward. The Origin of the Moon. In *Lunar and Planetary Science Conference*, volume 7 of *Lunar and Planetary Science Conference*, March 1976. (Cited on page 2.)

[14] Stephen Walley. Bibliography of 2013 Shock Physics Papers (Updated 19 Jun 2015), 2013. (Cited on page 2.)

[15] Stephen Walley. Bibliography of 2014 Shock Physics Papers (Updated 01 Jan 2016), 2014. (Cited on page 2.)

[16] Stephen Walley. Bibliography of 2015 Shock Physics Papers (Updated 01 Jan 2016), 2015. (Cited on page 2.)

[17] W. H. Gust and E. B. Royce. Axial Yield Strengths and Two Successive Phase Transition Stresses for Crystalline Silicon. *Journal of Applied Physics*, 42(5):1897, 1971. (Cited on pages 2, 37, 76 and 101.)

[18] R. F. Smith, R. W. Minich, R. E. Rudd, J. H. Eggert, C. A. Bolme, S. L. Brygoo, A. M. Jones, and G. W. Collins. Orientation and rate dependence in high strain-rate compression of single-crystal silicon. *Physical Review B*, 86(24):245204, December 2012. (Cited on pages 2, 37, 77 and 100.)

[19] Quintin Johnson and A C. Mitchell. First x-ray diffraction evidence for a phase transition during shock-wave compression. *Phys. Rev. Lett.*, 29:1369–1371, Nov 1972. (Cited on page 2.)

[20] L. M. Barker. Laser interferometer for measuring high velocities of any reflecting surface. *Journal of Applied Physics*, 43(11):4669, 1972. (Cited on pages 2, 78 and 103.)

[21] Peter P. Gillis, Kenneth G. Hoge, and Richard J. Wasley. Elastic precursor decay in tantalum. *Journal of Applied Physics*, 42(5):2145–2146, 1971. (Cited on page 2.)

[22] R. F. Smith, J. H. Eggert, M. D. Saculla, A. F. Jankowski, M. Bastea, D. G. Hicks, and G. W. Collins. Ultrafast dynamic compression technique to study the kinetics of phase transformations in bismuth. *Phys. Rev. Lett.*, 101:065701, Aug 2008. (Cited on page 2.)

[23] A. Higginbotham, P. G. Stubley, A. J. Comley, J. H. Eggert, J. M. Foster, D. H. Kalantar, D. McGonegle, S. Patel, L. J. Peacock, S. D. Rothman, R. F. Smith, M. J. Suggit, and J. S. Wark. Inelastic response of silicon to shock compression. *Scientific Reports*, 6(April):24211, 2016. (Cited on pages 2, 5 and 80.)

[24] William C. Dash. Growth of Silicon Crystals Free from Dislocations. *Journal of Applied Physics*, 30(4):459–474, 1959. (Cited on page 2.)

[25] A. Loveridge-Smith, A. Allen, J. Belak, T. Boehly, A. Hauer, B. Holian, D. Kalantar, G. Kyrala, R. Lee, P. Lomdahl, M. Meyers, D. Paisley, S. Pollaine, B. Remington, D. Swift, S. Weber, and J. S. Wark. Anomalous Elastic Response of Silicon to Uniaxial Shock Compression on Nanosecond Time Scales. *Physical Review Letters*, 86(11):2349–2352, March 2001. (Cited on pages 3, 76, 82, 97 and 101.)

[26] Stefan J. Turneaure and Y. M. Gupta. Real-time x-ray diffraction at the impact surface of shocked crystals. *Journal of Applied Physics*, 111(2):026101, 2012. (Cited on pages 3, 77 and 102.)

[27] J.R. Asay and M. Shahinpoor. *High-Pressure Shock Compression of Solids*. Shock Wave and High Pressure Phenomena. Springer New York, 2012. (Cited on page 3.)

[28] John M. Walsh and Russell H. Christian. Equation of state of metals from shock wave measurements. *Phys. Rev.*, 93, 1955. (Cited on page 3.)

[29] John M. Walsh, Melvin H. Rice, Robert G. McQueen, and Frederick L. Yarger. Shock-wave compressions of twenty-seven metals. Equations of state of metals. *Physical Review*, 108(2):196–216, 1957. (Cited on page 3.)

[30] R. G. McQueen and S. P. Marsh. Equation of state for nineteen metallic elements from shock-wave measurements to two megabars. *Journal of Applied Physics*, 31(7):1253–1269, 1960. (Cited on page 3.)

[31] R. G. Shreffler and W. E. Deal. Free surface properties of explosive-driven metal plates. *Journal of Applied Physics*, 24(1):44–48, 1953. (Cited on page 3.)

[32] A. C. Charters. Development of the high-velocity gas-dynamics gun. *International Journal of Impact Engineering*, 5(1-4):181–203, 1987. (Cited on page 3.)

[33] A. V. Pavlenko, S. I. Balabin, O. E. Kozelkov, and D. N. Kazakov. A one-stage light-gas gun for studying dynamic properties of structural materials in a range up to 40 GPa. *Instruments and Experimental Techniques*, 56(4):482–484, 2013. (Cited on page 3.)

[34] W. D. Crozier and William Hume. High-velocity, Light-gas gun. *Journal of Applied Physics*, 28(8):892–894, 1957. (Cited on page 3.)

[35] J. Michael Brown and G. Mcqueen. Phase Transitions, Grüneisen Parameter, and Elasticity. *Journal of Geophysical Research*, 91:7485–7494, 1986. (Cited on page 3.)

[36] N. C. Holmes, J. A. Moriarty, G. R. Gathers, and W. J. Nellis. The equation of state of platinum to 660 GPa (6.6 Mbar). *Journal of Applied Physics*, 66(7):2962–2967, 1989. (Cited on page 3.)

[37] A. Jayaraman. Diamond anvil cell and high-pressure physical investigations. *Rev. Mod. Phys.*, 55:65–108, Jan 1983. (Cited on page 3.)

[38] Arthur L. Ruoff, Hui Xia, Huan Luo, and Yogesh K. Vohra. Miniaturization techniques for obtaining static pressures comparable to the pressure at the center of the earth: Xray diffraction at 416 GPa. *Review of Scientific Instruments*, 61(12):3830–3833, 1990. (Cited on page 4.)

[39] Leonid Dubrovinsky, Natalia Dubrovinskaia, Vitali B. Prakapenka, and Artem M. Abakumov. Implementation of micro-ball nanodiamond anvils for high-pressure studies above 6 Mbar. *Nature communications*, 3:1163, Jan 2012. (Cited on page 4.)

[40] L. Dubrovinsky, N. Dubrovinskaia, E. Bykova, M. Bykov, V. Prakapenka, C. Prescher, K. Glazyrin, H.-P. Liermann, M. Hanfland, M. Ekholm, Q. Feng, L. V. Pourovskii, M. I. Katsnelson, J. M. Wills, and I. A. Abrikosov. The most incompressible metal osmium at static pressures above 750 gigapascals. *Nature*, 525(7568):226–229, 2015. (Cited on page 4.)

[41] C. Phipps. *Laser Ablation and Its Applications*. Springer Series in Optical Sciences. Springer, 2007. (Cited on page 4.)

[42] A. Lazicki, J. R. Rygg, F. Coppari, R. Smith, D. Fratanduono, R. G. Kraus, G. W. Collins, R. Briggs, D. G. Braun, D. C. Swift, and J. H. Eggert. X-Ray Diffraction of Solid Tin to 1.2 TPa. *Phys. Rev. Lett.*, 115:075502, Aug 2015. (Cited on page 4.)

[43] A. L. Kritcher, T. Döppner, D. Swift, J. Hawreliak, G. Collins, J. Nilsen, B. Bachmann, E. Dewald, D. Strozzi, S. Felker, O. L. Landen, O. Jones, C. Thomas, J. Hammer, C. Keane, H. J. Lee, S. H. Glenzer, S. Rothman, D. Chapman, D. Kraus, P. Neumayer, and R. W. Falcone. Probing matter at Gbar pressures at the NIF. *High Energy Density Physics*, 10(1):27–34, 2014. (Cited on page 4.)

[44] Justin S. Wark, Andrew Higginbotham, Despina Milathianaki, and Arianna Gleason. Combined hydrodynamic and diffraction simulations of femtosecond x-ray scattering from laser-shocked crystals. *Journal of Physics: Conference Series*, 500(15):152016, 2014. (Cited on pages 5 and 54.)

[45] A. E. Gleason, C. A. Bolme, H. J. Lee, B. Nagler, E. Galtier, D. Milathianaki, J. Hawreliak, R. G. Kraus, J. H. Eggert, D. E. Fratanduono, G. W. Collins, R. Sandberg, W. Yang, and W. L. Mao. Ultrafast visualization of crystallization and grain growth in shock-compressed SiO2. *Nature Communications*, 6:8191, 2015. (Cited on page 6.)

[46] B.E. Warren. *X-ray Diffraction*. Addison-Wesley series in metallurgy and materials engineering. Dover Publications, 1969. (Cited on page 8.)

[47] J. F. Nye. *Physical Properties of Crystals: Their Representation by Tensors and Matrices*. Oxford science publications. Clarendon Press, 1985. (Cited on pages 8 and 20.)

[48] S. H. Simon. *The Oxford Solid State Basics*. OUP Oxford, 2013. (Cited on pages 8, 24, 25 and 26.)

[49] M. A. Meyers. *Dynamic Behavior of Materials*. Wiley-Interscience publication. Wiley, 1994. (Cited on pages 8, 32 and 39.)

[50] Auguste Bravais. *English translation from original by A. J. Shaler: On the systems formed by points regularly distributed on a plane or in space*. Crystallographic Society of America, 1949. (Cited on page 10.)

[51] Robert Hooke. *Given as a latin anagram in Lectiones Cutlerianæ, or, A collection of lectures, physical, mechanical, geographical, & astronomical made before the Royal Society on several occasions at Gresham Colledge, Number 3: A description of helioscopes and some other instruments, Page 31*. London : Printed for John Martyn, printer to the Royal Society, at the Bell in S. Pauls Church-yard, 1679. (Cited on page 20.)

[52] So Bo Batdorf and Bernard Budiansky. A mathematical theory of plasticity based on the concept of slip. 1949. (Cited on page 22.)

[53] T. E. Mitchell and W. A. Spitzig. Three-Stage Hardening in Tantalum Single Crystals. *Acta Metallurgica*, 13(11):1169–1179, 1965. (Cited on page 23.)

[54] L. E. Murr, M. A. Meyers, S. Niou, Y. J. Chen, S. Pappu, and C Kennedy. Shock-induced deformation twinning in tantalum. *Acta materialia*, 45(1):157–175, 1997. (Cited on page 23.)

[55] Percy Williams Bridgman. *Collected experimental papers*. Cambridge, Harvard University Press., 1964. (Cited on page 23.)

[56] Dennison Bancroft, Eric L. Peterson, and Stanley Minshall. Polymorphism of iron at high pressure. *Journal of Applied Physics*, 27(3):291–298, 1956. (Cited on page 23.)

[57] John C. Jamieson and A. W. Lawson. X-ray diffraction studies in the 100 kilobar pressure range. *Journal of Applied Physics*, 33(3):776–780, 1962. (Cited on page 23.)

[58] W. H. Bragg and W. L. Bragg. The Reflection of X-rays by Crystals. *Proceedings of the Royal Society of London*, 88(605):428–438, 1913. (Cited on pages 23 and 29.)

[59] Justin S. Wark, Robert R. Whitlock, Allan A. Hauer, James E. Swain, and Paul J. Solone. Subnanosecond X-ray diffraction from laser-shocked crystals. *Physical Review B*, 40(8):5705–5714, 1989. (Cited on page 29.)

[60] D. H. Kalantar, E. A. Chandler, J. D. Colvin, R. Lee, B. A. Remington, S. V. Weber, L. G. Wiley, A. Hauer, J. S. Wark, A. Loveridge, B. H. Failor, M. A. Meyers, and G. Ravichandran. Transient x-ray diffraction used to diagnose shock compressed Si crystals on the Nova laser. *Review of Scientific Instruments*, 70(1):629, 1999. (Cited on pages 29 and 84.)

[61] W. L. Bragg. The Structure of Some Crystals as Indicated by their Diffraction of X-rays. *Proceedings of the Royal Society of London A: Mathematical, Physical and Engineering Sciences*, 89:248–277, 1913. (Cited on page 29.)

[62] W. Friedrich, P. Knipping, and M. Laue. Interferenzerscheinungen bei Röntgenstrahlen. *Annalen der Physik*, 346(10):971–988, 1913. (Cited on page 29.)

[63] Peter Debye and Paul Scherrer. Interferenzen an regellos orientierten teilchen im röntgenlicht. i. *Nachrichten von der Gesellschaft der Wissenschaften zu Göttingen, Mathematisch-Physikalische Klasse*, 1916:1–15, 1916. (Cited on page 29.)

[64] A. Hull. A New Method of X-Ray Crystal Analysis. *Physical Review*, 10(6):661–696, 1917. (Cited on page 29.)

[65] J. Ian Langford and Daniel Louer. Powder diffraction. *Reports on Progress in Physics*, 59(2):131, 1996. (Cited on page 29.)

[66] P. P. Ewald. Introduction to the dynamical theory of X-ray diffraction. *Acta Crystallographica Section A: Crystal Physics, Diffraction, Theoretical and General Crystallography*, 25(1):103–108, 1969. (Cited on page 30.)

[67] W . J . Macquorn Rankine. On the Thermodynamic Theory of Waves of Finite Longitudinal Disturbance. *Philosophical Transactions of the Royal Society of London*, 160(May):277–288, 1870. (Cited on page 32.)

[68] Henri Hugoniot. Sur la propagation du movement dans les corps et spécialement dans les gaz parfaits. *J. Ecole Polytechnique*, 58:1–125, 1889. (Cited on page 32.)

[69] Brad Lee Holian. Modeling shock-wave deformation via molecular dynamics. *Physical Review A*, 37(7):2562–2568, 1988. (Cited on page 37.)

[70] B. L. Holian. Atomistic computer simulations of shock waves. *Shock Waves*, 5(3):149–157, 1995. (Cited on page 37.)

[71] Y. M. Gupta, G. E. Duvall, and G. R. Fowles. Dislocation mechanisms for stress relaxation in shocked LiF. *Journal of Applied Physics*, 46(2):532, 1975. (Cited on pages 37 and 73.)

[72] E. Orowan. Problems of plastic gliding. *Proceedings of the Physical Society*, 52(1):8, 1940. (Cited on page 37.)

[73] David J. Benson. Computational methods in Lagrangian and Eulerian hydrocodes. *Computer Methods in Applied Mechanics and Engineering*, 99(2-3):235–394, 1992. (Cited on pages 40, 41 and 54.)

[74] C. L. M. H. Navier. Sur les lois des mouvement des fluides, en ayant egard a l'adhesion des molecules. *Ann. Chim. Paris*, 19:244–260, 1821. (Cited on page 40.)

[75] M. J. Berger and P. Colella. Local adaptive mesh refinement for shock hydrodynamics. *Journal of Computational Physics*, 82(1):64–84, 1989. (Cited on page 42.)

[76] R. Courant, K. Friedrichs, and H. Lewy. Uber die partiellen Differenzengleichungen der mathematischen Physik. *Mathematische Annalen*, 100(1):32–74, 1928. (Cited on page 43.)

[77] R. Courant, K. Friedrichs, and H. Lewy. On the partial difference equations of mathematical physics. *IBM Journal*, 100(March):32–74, 1928. (Cited on page 43.)

[78] J. VonNeumann and R. D. Richtmyer. A Method for the Numerical Calculation of Hydrodynamic Shocks. *Journal of Applied Physics*, 21(3):232, 1950. (Cited on page 43.)

[79] Gordon R. Johnson and William H. Cook. A constitutive model and data for metals subjected to large strains, high strain rates and high temperatures. In *Proceedings of the 7th International Symposium on Ballistics*, volume 21, pages 541–547. The Hague, The Netherlands, 1983. (Cited on page 44.)

[80] D. J. Steinberg, S. G. Cochran, and M. W. Guinan. A constitutive model for metals applicable at high-strain rate. *Journal of Applied Physics*, 51(3):1498–1504, 1980. (Cited on page 44.)

[81] Frank J. Zerilli and Ronald W. Armstrong. Dislocation-mechanics-based constitutive relations for material dynamics calculations. *Journal of Applied Physics*, 61(5):1816–1825, 1987. (Cited on page 44.)

[82] Y. Horie. Numerical Integration of Plane Elastic-Relaxing Plastic Shock Waves by a Two-Step Method. *Journal of Applied Physics*, 40(13):5368, 1969. (It's an older code, sir, but it checks out). (Cited on pages 44 and 52.)

[83] J T Larson. *HYADES - Book II - The Physics in HYADES - Material Constitutive Models*. (Cited on page 44.)

[84] R. Ravelo, T. C. Germann, O. Guerrero, Q. An, and B. L. Holian. Shock-induced plasticity in tantalum single crystals: Interatomic potentials and large-scale molecular-dynamics simulations. *Physical Review B - Condensed Matter and Materials Physics*, 88(13):1–17, 2013. (Cited on page 45.)

[85] L. Pizzagalli, J. Godet, J. Guénolé, S. Brochard, E. Holmstrom, K. Nordlund, and T. Albaret. A new parametrization of the Stillinger-Weber potential for an improved description of defects and plasticity of silicon. *Journal of Physics: Condensed Matter*, 25(5):55801, 2013. (Cited on page 45.)

[86] Steve Plimpton. Fast Parallel Algorithms for Short – Range Molecular Dynamics. *Journal of Computational Physics*, 117(June 1994):1–19, 1995. (Cited on pages 45 and 64.)

[87] Benjamin FrantzDale, Steven J. Plimpton, and Mark S. Shephard. Software components for parallel multiscale simulation: An example with LAMMPS. *Engineering with Computers*, 26(2):205–211, 2010. (Cited on page 45.)

[88] Loup Verlet. Computer “Experiments” on Classical Fluids. I. Thermodynamical Properties of Lennard-Jones Molecules. *Phys. Rev.*, 159(1):98, 1967. (Cited on page 46.)

[89] William C. Swope, Hans C. Andersen, Peter H. Berens, and Kent R. Wilson. A computer simulation method for the calculation of equilibrium constants for the formation of physical clusters of molecules: Application to small water clusters. *J. Chem. Phys.*, 76(1):637–649, 1982. (Cited on page 46.)

[90] Giles Kimminau, Paul Erhart, Eduardo M. Bringa, Bruce Remington, and Justin S. Wark. Phonon instabilities in uniaxially compressed fcc metals as seen in molecular dynamics simulations. *Physical Review B - Condensed Matter and Materials Physics*, 81(9):1–4, 2010. (Cited on page 46.)

[91] Giles Kimminau, Bob Nagler, Andrew Higginbotham, William J Murphy, Nigel Park, James Hawreliak, Kai Kadau, Timothy C Germann, Eduardo M Bringa, Daniel H Kalantar, Hector E Lorenzana, Bruce a Remington, and Justin S Wark. Simulating picosecond x-ray diffraction from shocked crystals using post-processing molecular dynamics calculations. *Journal of Physics: Condensed Matter*, 20(50):505203, 2008. (Cited on page 47.)

[92] M. I. McMahon, R. J. Nelmes, N. G. Wright, and D. R. Allan. Pressure dependence of the Imma phase of silicon. *Physical Review B*, 50(2):739743, 1994. (Cited on pages 49 and 131.)

[93] Gabriele Mogni, Andrew Higginbotham, Katalin Gaál-Nagy, Nigel Park, and Justin S. Wark. Molecular dynamics simulations of shock-compressed single-crystal silicon. *Physical Review B*, 89(6):064104, February 2014. (Cited on pages 49, 64, 65, 70, 72, 86 and 120.)

[94] D. Milathianaki, S. Boutet, G. J. Williams, A. Higginbotham, D. Ratner, A. E. Gleason, M. Messerschmidt, M. M. Seibert, D. C. Swift, P. Hering, J. Robinson, W. E. White, and J. S. Wark. Femtosecond visualization of lattice dynamics in shock-compressed matter. *Science (New York, N.Y.)*, 342(6155):220–3, October 2013. (Cited on page 54.)

[95] A. Reuss. Berechnung der Fliehgrenze von Mischkristallen auf Grund der Plastizittitsbedingung fiir Einkristalle. *Zeitschrift für angewandte Mathematik und Mechanik*, 9:49–58, 1929. (Cited on page 57.)

[96] K. Gaál-Nagy, A. Bauer, P. Pavone, and D. Strauch. Ab initio study of the enthalpy barriers of the high-pressure phase transition from the cubic-diamond to the beta-tin structure of silicon and germanium. *Computational Materials Science*, 30(1-2 SPEC ISS.):1–7, 2004. (Cited on pages 60 and 88.)

[97] J. Tersoff. New empirical approach for the structure and energy of covalent systems. *Physical Review B*, 37(12):6991–7000, 1988. (Cited on page 64.)

[98] P. Erhart and K. Albe. Analytical potential for atomistic simulations of silicon, carbon, and silicon carbide. *Physical Review B*, 71(3):35211, 2005. (Cited on page 64.)

[99] T. Nicholas, A. M. Rajendran, and D. J. Grove. An offset yield criterion from precursor decay analysis. *Acta Mechanica*, 69(1-4):205–218, Dec 1987. (Cited on page 73.)

[100] Jon T. Larsen and Stephen M. Lane. HYADES-A plasma hydrodynamics code for dense plasma studies. *Journal of Quantitative Spectroscopy and Radiative Transfer*, 51(1-2):179–186, 1994. (Cited on page 74.)

[101] L. V. Al'tshuler. Use of shock waves in high-pressure physics. *Soviet Physics Uspekhi*, 8(1):52, 1965. (Cited on page 76.)

[102] M. N. Pavlovskii. Formation of metallic modification of Germanium and Silicon under shock loading, 1967. (Cited on page 76.)

[103] S. Minomura and H. G. Drickamer. Pressure induced phase transitions in silicon, germanium and some III–V compounds. *Journal of Physics and Chemistry of Solids*, 23(5):451–456, 1962. (Cited on pages 76 and 129.)

[104] J. C. Jamieson. Crystal Structures at High Pressure of Metallic Modifications of Silicon and Germanium. *Science*, 139(22):762, 1963. (Cited on page 76.)

[105] Tsuneaki Goto, Toshiyuki Sato, and Yasuhiko Syono. Reduction of shear strength and phase-transition in shock-loaded silicon. *Japanese Journal of Applied Physics*, 21(Part 2, No. 6):L369–L371, 1982. (Cited on page 76.)

[106] Stefan J. Turneaure and Y. M. Gupta. Inelastic deformation and phase transformation of shock compressed silicon single crystals. *Applied Physics Letters*, 91(20):201913, 2007. (Cited on pages 77, 100 and 101.)

[107] Matthew Suggit, Giles Kimminau, James Hawreliak, Bruce Remington, Nigel Park, and Justin S. Wark. Nanosecond x-ray Laue diffraction apparatus suitable for laser shock compression experiments. *The Review of scientific instruments*, 81(8):083902, August 2010. (Cited on pages 78, 80, 95 and 96.)

[108] A. J. Comley, B. R. Maddox, R. E. Rudd, S. T. Prisbrey, J. A. Hawreliak, D. A. Orlikowski, S. C. Peterson, J. H. Satcher, A. J. Elsholz, H.-S. Park, B. A. Remington, N. Bazin, J. M. Foster, P. Graham, N. Park, P. A. Rosen, S. R. Rothman, A. Higginbotham, M. Suggit, and J. S. Wark. Strength of Shock-Loaded Single-Crystal Tantalum [100] Determined using In Situ Broadband X-Ray Laue Diffraction. *Physical Review Letters*, 110(11):115501, March 2013. (Cited on pages 78, 80 and 81.)

[109] Nicholas Hopps, Kevin Oades, Jim Andrew, Colin Brown, Graham Cooper, Colin Danson, Simon Daykin, Stuart Duffield, Ray Edwards, David Egan, Stephen Elsmere, Steve Gales, Mark Girling, Edward Gumbrell, Ewan Harvey, David Hillier, David Hoarty, Colin Horsfield, Steven James, Alex Leatherland, Stephen Masoero, Anthony Meadowcroft, Michael Norman, Stefan Parker, Stephen Rothman, Michael Rubery, Paul Treadwell, David Winter, and Thomas Bett. Comprehensive description of the Orion laser facility. *Plasma Physics and Controlled Fusion*, 57(6):064002, 2015. (Cited on page 79.)

[110] http://creativecommons.org/licenses/by/4.0/legalcode. (Cited on page 80.)

[111] Matthew J. Suggit, Andrew Higginbotham, James A. Hawreliak, Gabriele Mogni, Giles Kimminau, Patrick Dunne, Andrew J. Comley, Nigel Park, Bruce A. Remington, and Justin S. Wark. Nanosecond white-light Laue diffraction measurements of dislocation microstructure in shock-compressed single-crystal copper. *Nature communications*, 3:1224, 2012. (Cited on page 80.)

[112] B. R. Maddox, H. S. Park, B. A. Remington, C. Chen, S. Chen, S. T. Prisbrey, A. Comley, C. A. Back, C. Szabo, J. F. Seely, U. Feldman, L. T. Hudson, S. Seltzer, M. J. Haugh, and Z. Ali. Absolute measurements of x-ray backlighter sources at energies above 10 keV. *Physics of Plasmas*, 18(5):0–6, 2011. (Cited on page 81.)

[113] J. S. Wark, D. Riley, N. C. Woolsey, G. Keihn, and R. R. Whitlock. Direct measurements of compressive and tensile strain during shock breakout by use of subnanosecond x-ray diffraction. *Journal of Applied Physics*, 68(9):4531–4534, 1990. (Cited on page 84.)

[114] Futoshi Shimizu, Shigenobu Ogata, and Ju Li. Theory of Shear Banding in Metallic Glasses and Molecular Dynamics Calculations. *Materials Transactions*, 48(11):2923–2927, 2007. (Cited on page 86.)

[115] Patrick Mora. Theoretical model of absorption of laser light by a plasma. *Physics of Fluids*, 25(6):1051, 1982. (Cited on pages 98 and 99.)

[116] Stefan J. Turneaure and Y. M. Gupta. X-ray diffraction and continuum measurements in silicon crystals shocked below the elastic limit. *Applied Physics Letters*, 90(5):051905, 2007. (Cited on page 103.)

[117] Nigel Charles Woolsey. *Time resolved, in situ, x-ray diffraction from laser shocked solids.* PhD thesis, University of Oxford, March 1994. (Cited on page 103.)

[118] Shamim Patel, Matthew J Suggit, Paul G Stubley, James a Hawreliak, Orlando Ciricosta, Andrew J Comley, Gilbert W Collins, Jon H Eggert, John M Foster, Justin S Wark, and Andrew Higginbotham. Single Hit Energy-resolved Laue Diffraction. *The Review of scientific instruments*, 86(5):053908, 2015. (Cited on page 104.)

[119] John M. J. Madey. Stimulated emission of bremsstrahlung in a periodic magnetic field. *Journal of Applied Physics*, 42(5):1906–1913, 1971. (Cited on page 106.)

[120] J. Arthur, G. Materlik, R. Tatchyn, and H. Winick. The LCLS: A fourth generation light source using the SLAC linac. *Review of Scientific Instruments*, 66(2):1987–1989, 1995. (Cited on page 106.)

[121] P. Emma, R. Akre, J. Arthur, R. Bionta, C. Bostedt, J. Bozek, A. Brachmann, P. Bucksbaum, R. Coffee, F.-J. Decker, Y. Ding, D. Dowell, S. Edstrom, A. Fisher, J. Frisch, S. Gilevich, J. Hastings, G. Hays, Ph. Hering, Z. Huang, R. Iverson, H. Loos, M. Messerschmidt, A. Miahnahri, S. Moeller, H.-D. Nuhn, G. Pile, D. Ratner, J. Rzepiela, D. Schultz, T. Smith, P. Stefan, H. Tompkins, J. Turner, J. Welch, W. White, J. Wu, G. Yocky, and J. Galayda. First lasing and operation of an ångstrom-wavelength free-electron laser. *Nature Photonics*, 4(9):641–647, 2010. (Cited on page 106.)

[122] Donald H Bilderback, Pascal Elleaume, and Edgar Weckert. Review of third and next generation synchrotron light sources. *Journal of Physics B: Atomic, Molecular and Optical Physics*, 38(9):S773, 2005. (Cited on page 106.)

[123] Bob Nagler, Brice Arnold, Gary Bouchard, Richard F. Boyce, Richard M. Boyce, Alice Callen, Marc Campell, Ruben Curiel, Eric Galtier, Justin Garofoli, Eduardo Granados, Jerry Hastings, Greg Hays, Philip Heimann, Richard W. Lee, Despina Milathianaki, Lori Plummer, Andreas Schropp, Alex Wallace, Marc Welch, William White, Zhou Xing, Jing Yin, James Young, Ulf Zastrau, and Hae Ja Lee. The Matter in Extreme Conditions instrument at the Linac Coherent Light Source. *Journal of Synchrotron Radiation*, 22(November 2014):520–525, 2015. (Cited on page 106.)

[124] P. Hart, S. Boutet, G. Carini, A. Dragone, B. Duda, D. Freytag, G. Haller, R. Herbst, S. Herrmann, C. Kenney, J. Morse, M. Nordby, J. Pines, N. Van Bakel, M. Weaver, and G. Williams. The Cornell-SLAC pixel array detector at LCLS. *IEEE Nuclear Science Symposium Conference Record*, pages 538–541, 2012. (Cited on page 107.)

[125] Z. Xing, E. Galtier, H. J. Lee, E. Granados, B. Arnold, S. Mullane, C. Bolme, A. Fry, P. Hart, and B. Nagler. X-ray diffraction at Matter in Extreme Conditions endstation. In *57th Annual Meeting of the APS Division of Plasma Physics, Savannah, US, November 16-20, 2015*, pages 1–7, 2015. (Cited on page 111.)

[126] R. H. Wentorf and J. S. Kasper. Two New Forms of Silicon. *Science (New York, N.Y.)*, 139:338, 1963. (Cited on page 129.)

[127] J. S. Kasper and S. M. Richards. The crystal structures of new forms of silicon and germanium. *Acta Crystallographica*, 17:752–755, 1964. (Cited on page 129.)

[128] J. Crain, G. J. Ackland, J. R. Maclean, R. O. Piltz, P. D. Hatton, and S. Pawley. Reversible pressure-induced structural transitions between metastable phases of silicon. *Physical Review B*, 50(17), 1994. (Cited on page 129.)

[129] You Xiang Zhao, Fred Buehler, James R. Sites, and Ian L. Spain. New metastable phases of silicon. *Solid State Communications*, 59(10):679–682, 1986. (Cited on page 129.)

[130] R. O. Piltz, J. R. Maclean, S. J. Clark, G. J. Ackland, P. D. Hatton, and J. Crain. Structure and properties of silicon XII: A complew tetrahedrally bonded phase. *Physical Review B*, 52(6):4072, 1995. (Cited on page 129.)